SOURCE CHARACTERISTICS OF LARGE STRIKE-SLIP EARTHQUAKES

A DISSERTATION
SUBMITTED TO THE DEPARTMENT OF GEOPHYSICS
AND THE COMMITTEE ON GRADUATE STUDIES
OF STANFORD UNIVERSITY
IN PARTIAL FULLFILLMENT OF THE REQUIREMENTS
FOR THE DEGREE OF
DOCTOR OF PHILOSOPHY

Seok-Goo Song

June 2007

Reproduced with permission of the copyright owner. Further reproduction prohibited without permission.

UMI Number: 3267636

INFORMATION TO USERS

The quality of this reproduction is dependent upon the quality of the copy submitted. Broken or indistinct print, colored or poor quality illustrations and photographs, print bleed-through, substandard margins, and improper alignment can adversely affect reproduction.

In the unlikely event that the author did not send a complete manuscript and there are missing pages, these will be noted. Also, if unauthorized copyright material had to be removed, a note will indicate the deletion.

UMI®

UMI Microform 3267636

Copyright 2007 by ProQuest Information and Learning Company.

All rights reserved. This microform edition is protected against unauthorized copying under Title 17, United States Code.

ProQuest Information and Learning Company
300 North Zeeb Road
P.O. Box 1346
Ann Arbor, MI 48106-1346

Reproduced with permission of the copyright owner. Further reproduction prohibited without permission.

© Copyright by Seok-Goo Song 2007
All Rights Reserved

Reproduced with permission of the copyright owner. Further reproduction prohibited without permission.

I certify that I have read this dissertation and that, in my opinion, it is fully adequate in scope and quality as a dissertation for the degree of Doctor of Philosophy.

Gregory C. Beroza (Principal Advisor)

I certify that I have read this dissertation and that, in my opinion, it is fully adequate in scope and quality as a dissertation for the degree of Doctor of Philosophy.

Paul Segall

I certify that I have read this dissertation and that, in my opinion, it is fully adequate in scope and quality as a dissertation for the degree of Doctor of Philosophy.

Paul Spudich

Approved for the University Committee on Graduate Studies:

Reproduced with permission of the copyright owner. Further reproduction prohibited without permission.

Abstract

We investigate complex earthquake source processes using both spontaneous dynamic rupture modeling and kinematic finite-source inversion. Dynamic rupture modeling is an efficient tool with which we can examine how stress conditions and frictional behavior on a fault plane play a role in determining kinematic motions on the fault and the resulting ground motions at the Earth's surface. It enables us to develop a physical understanding of the earthquake rupture process in terms of Newtonian mechanics. Many interesting features of the earthquake source process can also be inferred from the kinematic source inversion of observed seismic or geodetic data. It is important to utilize our knowledge of the earthquake source to improve our understanding of near-field ground motion characteristics because source complexities are quite uncertain and can be the dominant factor in determining the characteristics of near-field ground motion.

We construct a set of spontaneous dynamic rupture models for several recent earthquakes in Japan and California, including the 1995 Kobe, Japan, earthquake and the 1989 Loma Prieta and 1992 Landers, California, earthquakes. Although the dynamic models are derived from the final slip alone, the slip and overall rupture duration, consistent with kinematic inversions, are successfully reproduced and in that sense they can be considered plausible models to represent the dynamic rupture properties of the selected events. Our dynamic models, together with several other models, for other earthquakes, obtained by different research groups, are used to investigate the scaling properties of fracture energy and stress drop.

We carry out a comprehensive source study of the 1906 San Francisco earthquake by re-analyzing both geodetic and seismic data in order to reconcile two existing, and mutually inconsistent, source models and obtain a unified one. We find that the 1906 earthquake experienced significant rupture along the entire northern segment of the San Andreas Fault - from Cape Mendocino to San Juan Bautista, resulting in about 500 km rupture length and M_w 7.9. We are able to reconcile the seismic data with the geodetically derived slip model by allowing the rupture velocity to exceed the shear wave velocity in the brittle crust (super-shear

Reproduced with permission of the copyright owner. Further reproduction prohibited without permission.

rupture). The unified source model for the earthquake has important implications for seismic hazard in California, and perhaps more generally for large strike-slip earthquakes. A slip model that reconciles the available data reduces the uncertainty in recurrence models for future earthquakes in northern California and suggests that the possibility of super-shear rupture should be taken into account when predicting the level and the variability of strong ground motion in future large strike-slip earthquakes.

Accurate prediction of the intensity and variability of near-field strong ground motion for future large earthquakes strongly depends on our ability to simulate realistic earthquake source models for those future events. We develop a pseudo-dynamic source modeling method with which we can generate physically self-consistent finite source models of large strike-slip earthquakes without high-cost, fully dynamic rupture simulation for near-field ground motion predictions. We construct 15 spontaneous dynamic rupture models with different slip realizations and hypocenter locations for large, M_w 7.5, strike-slip earthquakes, which have a very long and narrow rupture dimension, by taking advantage of high performance computing. Based on empirical relations derived from these dynamic modeling outputs, we develop efficient, physics-based finite-source characterization tools for ground motion predictions for large strike-slip earthquakes.

Reproduced with permission of the copyright owner. Further reproduction prohibited without permission.

Acknowledgements

I am deeply grateful to my advisor Greg Beroza for his continuous and solid support throughout my graduate school career. He is a kind of advisor who renders me understand what the word, "advisor," means. He inspired and motivated me with brilliant scientific ideas and guided me through the whole process of research with great support. I remember that he always cheered me up and tried to help me with plausible solutions when I got stuck in the middle of something and knocked his door for help in a gloomy mood. Recently I had a chance to go through hundreds of emails being back and forth between him and me. I could realize what level of communication has been carried out between us and also how much he was trying to help me and support me not only for my academic achievement but also in various aspects of my graduate school life. It is quite impressive that his reply came to my mail box within minutes most of the time whenever I sent him an email to ask for something.

I would like to thank my committee members David Pollard (chair), Paul Segall, Norm Sleep, and Paul Spudich for their enormous interests in my work and also for their numerous constructive criticisms, advices, and comments. I benefited greatly from Paul Segall and his in-depth knowledge in various areas from crustal deformation to inverse theory. In particular it would be impossible to make an achievement in the triangulation data analysis for the 1906 San Francisco earthquake source study without his distinctive insights into the field and continuous support. Norm Sleep, his broad range of knowledge in Science and all the funny stories he talked about in the quake seminar always impressed me and entertained me. His somewhat unexpected comments on many scientific issues enabled me to realize that we could take many different approaches in dealing with scientific problems although they do not look like conventional solutions. Paul Spudich, his endless enthusiasm and passion about Science always inspired me and stimulated me.

I owe a special debt of appreciation to Joe Andrews, who kindly provided me with his 3-D dynamic rupture code. I have no doubt that his code was a great backbone for my dynamic rupture modeling study. I am also indebted to David Wald and Wayne Thatcher for their kind

Reproduced with permission of the copyright owner. Further reproduction prohibited without permission.

support for the 1906 study by providing me with their data sets and also helping me with a lot of constructive critiques and comments. I cannot help mentioning the kindness of the National Geodetic Survey (NGS) when I was trying to gather century old triangulation data from their archives. It is definitely a laborious job, but they helped me with great support and willingness in this painful procedure. I would like to thank Brad Aagaard and all other ground motion modelers involved in the 3-D ground motion simulation project of the 1906 San Francisco earthquake. Their endless feedback and comments on my source model helped me to think about my study in more user-oriented way. I also want to thank Arben Pitarka for his support for the pseudo-dynamic source modeling study. This is an on-going project and I am sure that we will be closely collaborating on this issue even after this thesis.

Many thanks to the seismo gangs: Patti, Martin, Xyoli, Eva, David, Justin, Anu, Shuo. Special thanks to Patti and Martin, I started my work in the Earthquake Seismology group by reading their theses. I greatly benefited from their works and achievements. Also thanks to new comers: Justin Brown and Annemarie Baltay, I feel sorry that we do not have enough time to share many things, but I would like to welcome you all and wish you all the best while you stay here. It is a lot of fun and great benefits to study and discuss many different issues about Earthquake Science with people in different research fields. I want to thank all the people in the quake seminar: Mark Zoback, George Thompson, Jessica, Kaj, Andy, Doerte, Zhen, Emily, Kyle, Dan, Shinichi, Ryu, Ellen, Hannah, Amie, and all others. And also all the Korea gangs in the School of Earth Science: Youngseuk, Sung Keun, Chandong, Sang-Ho, Evan. They were great resources and comforts when I missed my home in Korea and we could share many things in the similar situation.

Lastly I want to thank my wife, Young Sun and my son, Tony. They introduced me a wonderful new world I had never imagined before and taught me why life is joyful. Without their endless love, unconditional support, and encouragement, I wouldn't have been able to finish my challenging task here at Stanford. I also would like to thank my mom and dad. Although they left me in an early stage of my life, I truly believe that they are still watching over me from above with great love and care.

Reproduced with permission of the copyright owner. Further reproduction prohibited without permission.

Table of Contents

Abstract iv

Acknowledgements vi

Table of Contents viii

List of Tables x

List of Illustrations xi

Chapter 1. Introduction 1

Chapte r 2. A Simple Dynamic Model for the 1995 Kobe, Japan Earthquake 9

Abstract 9

2.1. Introduction 9

2.2. Dynamic Modeling 10

2.3. Results 12

2.4. Discussion 14

Chapter 3. Dynamic Rupture Models of Recent Large Earthquakes: Toward Scaling of Fracture Energy and Stress Drop in Dynamic Rupture 20

Abstract 20

3.1. Introduction 21

3.2. Spontaneous Dynamic Rupture Modeling 22

3.2.1. Stress Drop and Fracture Energy 23

3.2.2. Fault Constitutive Law 25

3.2.3. Modeling Procedure 26

3.3. Dynamic Models 28

3.3.1. 1989 Loma Prieta Earthquake (M_w 6.9) 28

3.3.2. 1992 Landers Earthquake (M_w 7.2) 30

3.3.3. 1987 Whittier Narrows Earthquake (M_w 6.0) 32

3.4. Scaling of Fracture Energy and Stress Drop 33

3.5. Discussion 34

Reproduced with permission of the copyright owner. Further reproduction prohibited without permission.

Chapter 4. A Unified Source Model for the 1906 San Francisco Earthquake **47**

Abstract 47
4.1. Introduction 48
4.2. Geodetic Analysis 49
4.3. Seismic Analysis 51
4.4. Super-shear Rupture and Combined Slip Model 53
4.5. Discussion and Implications 55

Chapter 5. Pseudo-Dynamic Modeling of Large Strike-Slip Earthquakes **76**

Abstract 76
5.1. Introduction 77
5.2. Constructing Dynamic Rupture Models 79
5.2.1. Slip Realizations 79
5.2.2. Stress drop and Fracture Energy 81
5.2.3. Slip Weakening Friction Law 82
5.2.4. High Performance Computing 83
5.2.5. Dynamic Models 84
5.3. Pseudo-dynamic Source Characterization 86
5.3.1. Toward the Next Generation of Pseudo-dynamic Modeling 86
5.3.1.1. Relaxing the Sub-shear Rupture Velocity Constraint 87
5.3.1.2. Rise Time Scaling 88
5.3.2. Rupture Velocity 89
5.3.3. Slip Velocity Function (SVF) 91
5.3.3.1. Peak Slip Velocity 92
5.3.3.2. Pulse Width 93
5.3.3.3. Rise Time 93
5.3.4. Pseudo-dynamic Modeling Results 94
5.4. Discussion 96
5.5. Conclusions 98

Appendix A **115**
Appendix B (Bibliography) **118**

Reproduced with permission of the copyright owner. Further reproduction prohibited without permission.

List of Tables

Table 3.1. 1989 Loma Prieta earthquake 36
Table 3.2. 1-D Velocity structure used in the Loma Prieta earthquake modeling 36
Table 3.3. 1992 Landers earthquake 37
Table 3.4. 1-D Velocity structure used in the Landers earthquake modeling 37
Table 3.5. 1987 Whittier Narrows earthquake 38
Table 3.6. 1-D Velocity structure used in the Whittier Narrows earthquake 38

Table 4.1. Estimated (model coordinate) displacement fields in meter from triangulation data with predicted ones from the geodetic slip model 58
Table 4.2. Slip models from inversion of geodetic data only and combined inversion of the geodetic and seismic data 60

Table 5.1. 1-D velocity structure used in the modeling 101
Table 5.2. Modeling parameters used in the study 101

Reproduced with permission of the copyright owner. Further reproduction prohibited without permission.

List of Illustrations

Figure 2.1. Map showing the focal mechanism and surface projection of the fault plane 16
Figure 2.2. Final slip distribution of the Kobe earthquake and its static stress drop 17
Figure 2.3. Snapshot images of the rupture propagation for the Kobe earthquake 18
Figure 2.4. The comparison of the slip evolution 19

Figure 3.1. Slip-weakening friction law (Ida, 1972; Andrews, 1976a). 39
Figure 3.2. Flowchart of the dynamic modeling procedure 40
Figure 3.3. Two simple dynamic rupture models. (a) Constant yield stress, (b) Constant strength excess 41
Figure 3.4. Dynamic modeling results of the 1989 Loma Prieta earthquake 42
Figure 3.5. Fracture energy scaling with stress intensity factor 43
Figure 3.6. Dynamic modeling results for the 1992 Landers earthquake 44
Figure 3.7. Dynamic modeling results of the 1987 Whittier Narrows earthquake 45
Figure 3.8. Scaling of fracture energy with stress intensity factor 46

Figure 4.1. 1906 San Francisco earthquake 61
Figure 4.2. Comparison of two previous slip models for the 1906 event 62
Figure 4.3. Triangulation network in the northern region of the San Andreas fault 63
Figure 4.4. Estimated model coordinate displacement fields 64
Figure 4.5. Estimated model coordinate displacement fields in four local networks 65
Figure 4.6. Singular values used in the inversion 66
Figure 4.7. Slip model obtained from inversion of geodetic data 67
Figure 4.8. Cross validation curve used in the geodetic slip inversion 68
Figure 4.9. Five seismic stations used in the study 69
Figure 4.10. Waveforms recorded by the Wiechert Inverted Pendulum seismograph in Gottingen, Germany in the 1906 earthquake 70
Figure 4.11. Rupture time distribution along the fault with two segment (a) and five segment model (b) 71
Figure 4.12. Final slip models obtained from both geodetic and seismic data 72
Figure 4.13. Comparison of observed (solid) and calculated (dashed) waveforms and their envelopes 73

Reproduced with permission of the copyright owner. Further reproduction prohibited without permission.

Figure 4.14. Intensity map for the 1906 San Francisco earthquake by Boatwright and Bundock (2005) 74

Figure 4.15. Total rupture duration of the earthquake inferred from the deconvolution of observed waveforms 75

Figure 5.1. One example of slip realizations and stress drop and fracture energy distribution 102

Figure 5.2. Slip weakening friction law (Ida, 1972; Andrews, 1976) 103

Figure 5.3. One example of dynamic modeling outputs 104

Figure 5.4. Depth-averaged slip rate as a function of along-strike distance and time 105

Figure 5.5. Rupture time distribution and instantaneous rupture velocity 106

Figure 5.6. Scaling of (local) rupture velocity with slip 107

Figure 5.7. Slip velocity function parameterization in the PD approach 108

Figure 5.8. Peak slip velocity 109

Figure 5.9. Pulse width 110

Figure 5.10. Rise time as a function of total fault rupture duration and rupture time 111

Figure 5.11. Comparison of the pseudo-dynamic modeling results with the full dynamic approach (Model: dyna31) 112

Figure 5.12. Comparison of the pseudo-dynamic modeling with the full dynamic approach (Model: dyna13) 113

Figure 5.13. Scatter plots of the pseudo-dynamic modeling outputs with the full dynamic approach 114

Reproduced with permission of the copyright owner. Further reproduction prohibited without permission.

Chapter 1. Introduction

Earthquakes can be considered dynamic fracture inside the Earth and many features of the earthquake rupture process are well described by shear crack propagation (Kostrov and Das, 1988; Scholz, 1990). How the crack is formed, propagates and terminates, are fundamental questions in earthquake source physics and is also critical to understanding near-field ground motion characteristics generated by released stress from the crack propagation. My thesis aims to contribute to a better understanding of the complex earthquake rupture process, by implementing forward dynamic rupture modeling, kinematic finite-source inversion, and by utilizing the knowledge of the earthquake source derived from that modeling to improve our understanding of near-field ground motion characteristics.

The brittle crust of the Earth responds elastically to stress loaded by tectonic movement and deforms, depending its material properties and the level of the applied stress. Once the applied stress exceeds the critical level that the brittle crust endures, a crack is formed in a relatively weak zone and propagates in the surrounding region in a form of a running shear crack, creating a discontinuous boundary inside the Earth, i.e., fault. Seismic (or elastic) waves are generated as a result of the shear cracking because stress is released as the crack passes by and we expect to see ground shaking when the seismic waves propagate through the elastic Earth and arrive at the surface. In order to have a better understanding of the complex earthquake rupture process, we need to be able to answer many fundamental questions regarding various aspects of the faulting systems. For example, what are the initial stress conditions applied on a fault before earthquake rupture? How strong is our fault system in response to the applied stress? How do frictional properties change on the fault during rupture and what are the decay patterns of the stress field depending on the frictional behavior on a slipping fault?

Reproduced with permission of the copyright owner. Further reproduction prohibited without permission.

Byerlee's law (Byerlee, 1978) tells us that normal stress acting on a fault increases with depth so that the shear strength of the fault is proportional to the normal stress, and consequently increases with depth. The lack of a significant increase in the shear strength of the fault, often observed in active fault zones (Aki, 1972), generates debate on the actual strength level of the fault system; is it strong or weak? This is a particularly important question in seismically active fault zones. Constraining the absolute level of applied stress is also a challenging issue related to the fault strength problem. Seismologists tend to focus more on stress changes or stress drop before and after earthquake rupture because radiated seismic energy is mostly affected by the stress change, not its absolute level, and thus it can be better constrained by observed data.

In my thesis, stress drop is a main concern rather than the absolute level of both initial and final stress. Following the same approach, the strength of a fault can be represented by the difference between initial stress and the fault strength, e.q., strength excess. Once we know how much stress is applied on a fault system, and how strong the fault is or how much it can resist the applied stress, we are left with one more key element in order to fully describe the faulting system, that is, a fault constitutive law governing frictional behavior during rupture. Our knowledge of how stress drops as well as how much it drops after the fault starts slipping is critical for predicting the subsequent rupture behavior as well as the characteristics of radiated seismic energies. How traction changes on a slipping fault and what controls its behavior: slip, slip rate, or some other state parameters, has long been one of the main concerns of scientists studying earthquake rupture.

Reproduced with permission of the copyright owner. Further reproduction prohibited without permission.

The slip weakening law (Ida, 1972; Andrews, 1976a) was first introduced to remove the non-physical stress singularity near crack tip that occurred when abrupt stress drop is assumed. In this friction law, traction on a slipping fault is controlled by the amount of slip. As slip grows, the traction decays linearly from the yield stress and arrives at final stress when slip reaches a certain critical distance. More complicated laws like the rate- and state-dependent friction law (Okubo, 1989; Dieterich, 1994) have been introduced to explain and model various aspects of earthquake rupture (e.q., slow slip and self-healing, etc.), but the simple slip weakening law has been proved to be a good approximation at least for dynamically propagating stick-slip events. The fact that stress drops gradually rather than abruptly, introduces a new feature in earthquake rupture propagation, the cohesive zone. The cohesive zone is defined as the area where rupture front passes by but the slip does not reach the critical distance yet (Madariaga, 1983). In this region energy is absorbed for further propagation of the crack. The amount of energy that needs to be absorbed in this area is called fracture energy (or surface energy) which is defined as energy required to create a unit area of crack surface.

Once we specify the applied stress, shear strength, and constitutive law on a fault, we are ready to simulate the earthquake rupture process in a fully spontaneous way based on Newtonian mechanics. Once earthquake rupture is initiated, the rupture front is self-sustaining and the rupture criterion together with stress changes caused by previous rupture propagation determines "spontaneously" the evolution of rupture. The pattern of stress release at each point on a fault after the rupture front passes by is controlled by the fault constitutive law and the time varying applied stress field. The resulting kinematic motions (e.q., the temporal evolution of slip) are fully determined from the released stress based on Newtonian mechanics. Stress perturbations or kinematic motions in the form of displacement across a fault within an elastic continuum will generate elastic waves, which will propagate through the medium and

Reproduced with permission of the copyright owner. Further reproduction prohibited without permission.

arrive on the Earth's surface as ground shaking. The seismic wave propagation problem can be easily modeled by solving elastic-dynamic equations, using numerical methods, in a continuum body that has two boundaries, i.e., a traction free boundary at the Earth's surface and the fault inside the elastic medium. Spontaneous dynamic rupture modeling provides an opportunity to explore how the stress conditions and frictional behavior on a fault plane play a role in determining kinematic motions on the fault and resulting ground motions on the surface.

Given boundary conditions on a fault and material properties inside the Earth, we can now simulate how the seismic waves are generated from the fault and propagate through the Earth and arrive on the surface as ground motion. Our goal is to infer realistic boundary conditions on the fault from observed ground motion data or from kinematic models that are derived from those same ground motions. Once we account for propagation effects, often represented using Green's functions, synthetic ground motions can be easily computed by combining the evolution of the earthquake source with the Green's function. The spatial and temporal evolution of slip at the earthquake source can be obtained by solving a kinematic inverse problem with the observed ground motion data. Using this kinematic finite source inversion, many features of earthquake source process can be inferred from the observed data on the ground. For example, how much slip occurs at each point on a fault or how fast the rupture propagates on the fault.

While it is relatively straightforward to constrain kinematic motions on a fault from observed data, more challenging issues are involved in constraining dynamic parameters, such as initial stress and fracture energy from the observed data. No closed-form analytic expressions are available relating the dynamic source parameters and ground motions. Ground motions are

Reproduced with permission of the copyright owner. Further reproduction prohibited without permission.

less directly sensitive to many features of the dynamic source parameters, such as the absolute stress level. This problem is exacerbated by the band-limited nature of most ground motion data. Several studies have attempted to estimate dynamic parameters, either directly from observed data, or indirectly through constrained kinematic models (Fukuyama and Mikumo, 1993; Mikumo and Miyatake, 1995; Ide and Takeo, 1996; Peyrat et al., 2001; Peyrat et al., 2004), The results of these studies show that many different combinations of dynamic parameters can fit well, not only the kinematic models on the fault, but also the observed ground motions. This illustrates the difficulty of obtaining a unique dynamic model for a given earthquake rupture.

The factors that influence ground motion characteristics are traditionally divided into three categories: source, path, and site effects. The largest source of uncertainty in the near-field of large earthquakes, stems from our incomplete understanding of earthquake source effects. Recent finite-source inversion studies show that the earthquake source exhibits complex behavior, not just in terms of final slip distribution, but in all resolvable aspects of the source process, i.e., rupture velocity, rise time, and the temporal evolution of slip (Mai and Beroza, 2002; Guatteri et al., 2003). It is important to understand these source complexities and their effects on near-field ground motion characteristics not only for past earthquakes, but for strong ground motion prediction in future earthquakes.

My thesis touches several aspects of the earthquake source study: both forward rupture modeling and kinematic source inversion and investigates how we can utilize knowledge of the earthquake source to infer dynamic source parameters, and predict future ground motion.

Reproduced with permission of the copyright owner. Further reproduction prohibited without permission.

In Chapter 2 I start with dynamic rupture modeling of the 1995 Kobe, Japan, earthquake. It shows how a simple dynamic rupture model, which successfully reproduces kinematic models constrained by finite source inversion, can be constructed from a final slip model. All fundamental elements of the spontaneous dynamic rupture modeling are provided in this chapter. The implication of this study is that reasonable estimates of the temporal evolution of slip during earthquake rupture can be inferred from the slip distribution alone (Guatteri et al., 2003).

In Chapter 3 spontaneous dynamic rupture modeling is applied to several recent earthquakes in California, including the 1989 Loma Prieta and 1992 Landers earthquakes. Here we develop a set of plausible dynamic rupture models to produce kinematic motions consistent with finite source inversion. Even though it is impossible to obtain a unique dynamic model for a given event, developing plausible models is useful because they provide plausible interpretations of earthquake rupture dynamics. Our dynamic models, together with several other models obtained by different research groups, are used to investigate the scaling properties of fracture energy and stress drop by Mai et al. (2006).

In Chapter 4 we revisit the 1906 San Francisco earthquake that occurred about one century ago in the northern section of the San Andreas fault in California. Even though it is arguably the most important earthquake in the history of earthquake science, the two existing source models (geodetic and seismic) for the earthquake were clearly inconsistent with each other. This study was strongly motivated by the discrepancy and I re-visit the earthquake and re-analyze century-old data to resolve the puzzle and obtain a unique source model for the earthquake. A comprehensive source study was performed for the earthquake including both geodetic and seismic data analysis in this Chapter and we found that the 1906 earthquake

Reproduced with permission of the copyright owner. Further reproduction prohibited without permission.

experienced significant rupture along the entire northern segment of the San Andreas Fault – from Cape Mendocino to San Juan Bautista. In addition we showed that the seismic data can be reconciled with the geodetically derived slip model by allowing rupture velocity to exceed the shear wave velocity in the brittle crust (super-shear rupture).

The unified source model for the earthquake has important implications for seismic hazard in California. It reduces uncertainty in recurrence models for future earthquakes in northern California and also suggests that we ought to take into account the possibility of super-shear rupture when predicting the level and the variability of strong ground motion in future large strike-slip earthquakes. Our rupture was used as the basis for simulations of strong ground motion for the 1906 earthquake by different research groups.

Finally, in Chapter 5 we return to the dynamic rupture modeling, but pay more attention to developing a set of rules that provide an effective finite-source characterization that can be used for near-field ground motion predictions. This builds on the pioneering work of Guatteri et al. (2004) to develop an efficient way of providing physics-based kinematic source parameters for near-field strong motion prediction without a high computational cost. This approach has been termed "pseudo-dynamic" modeling because it is a kinematic approach that seeks to emulate the dynamic faulting, without extreme level of effort required for full dynamic rupture modeling.

The original pseudo-dynamic approach was designed for strike-slip earthquakes in the magnitude range of $6.4 < M < 7.2$. We extend this magnitude range further to cover larger events, which are of intense interest because they may control seismic hazard and because there is very little data to constrain ground motion for very large strike-slip earthquakes. By

Reproduced with permission of the copyright owner. Further reproduction prohibited without permission.

taking advantage of high performance computing, we developed a set of dynamic rupture models for large strike-slip (scenario) earthquakes (M ~ 7.5). Based on the results from this dynamic modeling, we have developed a next generation pseudo-dynamic rupture modeling scheme that captures important features of the rupture process for large strike-slip events.

Reproduced with permission of the copyright owner. Further reproduction prohibited without permission.

Chapter 2. A Simple Dynamic Model for the 1995 Kobe, Japan Earthquake

Song, S. G., and G. C. Beroza (2004), A simple dynamic model for the 1995 Kobe, Japan earthquake, *Geophys. Res. Lett.*, *31*, L18613, doi:10.1029/2004GL020557

Abstract

We investigate the dynamic rupture process of the 16 January 1995 Kobe earthquake (Mw 6.9) by spontaneous rupture modeling of a 3-D dynamic shear crack that reproduces the slip distribution found from kinematic waveform inversion of strong motion data. We find that using the heterogeneous initial stress field obtained from the kinematic slip model and relatively uniform fracture energy distribution, successfully generates a dynamic model with slip and rupture time distributions that are consistent with the kinematic source inversion. Our results suggest that we may be able to produce realistic dynamic rupture models with simpler assumptions for dynamic source parameters, such as the fracture energy, than have been used in most dynamic rupture models to date.

2.1. Introduction

The 16 January 1995 Kobe earthquake (Mw 6.9) occurred near the city of Kobe in western Japan, causing a tremendous amount of damage and the loss of many lives. The focal mechanism indicates right-lateral strike slip on a nearly vertical fault with the rupture area

Reproduced with permission of the copyright owner. Further reproduction prohibited without permission.

extending bilaterally from the hypocenter towards Awaji island to the southwest and towards the city of Kobe to the northeast as shown in Figure 2.1. Slip models, e.q., Ide and Takeo (1997), have been obtained by analyzing seismic and geodetic data.

In this study we construct a dynamic model that generates kinematic motions on the fault plane that are consistent with a kinematic source inversion. We are able to fit the kinematic rupture model with a fairly simple model of dynamic rupture. In our model, the initial stress is strongly variable, but the yield stress and slip weakening distance are almost uniform, which means our model has a relatively uniform fracture energy distribution.

2.2. Dynamic modeling

The final slip distribution of the Kobe earthquake as obtained from kinematic source modeling of Ide and Takeo (1997) and the associated static stress drop distribution are shown in Figure 2.2. As shown in the slip model, most of the slip occurred beneath Awaji island below the region of greatest surface rupture, while relatively little slip was observed below Kobe. The static stress drop distribution was calculated from the kinematic slip model using the Okada's method (Okada, 1992), which calculates static stress drop from a distribution of rectangular dislocations in a homogeneous half space. The stress drop distribution reveals two high stress patches separated by a narrow low stress band near Awaji island. Negative stress drop is observed in the relatively low slip area under Kobe.

Reproduced with permission of the copyright owner. Further reproduction prohibited without permission.

Based on the calculated stress drop distribution, we construct a possible dynamic model for the Kobe earthquake. First, we assume a homogeneous shear strength (τ_s) and final stress level (τ_f) over the fault plane computed following Byerlee's law (Byerlee, 1978) given below.

$$\tau_s = \tau_s \times \sigma_n = 0.6 \times 25 = 15 \text{ MPa} \quad (2.1)$$

$$\tau_f = \tau_f \times \sigma_n = 0.4 \times 25 = 10 \text{ MPa} \quad (2.2)$$

τ_s and τ_f are the static and dynamic frictional coefficient, respectively, and σ_n is the effective fault normal stress. While depth dependence of the normal stress is likely to occur, we assume a relatively low, and constant, normal stress (~25 MPa). The lack of a significant increase of earthquake stress parameters with depth are general characteristics of active fault zones in the Earth's crust (e.g., Aki, 1972). Spudich *et al.* (1998) also suggest a relatively low normal stress level (25 MPa) for the Kobe earthquake based on observations of temporal rake change. Thus, a uniform low normal stress (25 MPa) is used in our modeling. A heterogeneous initial stress field is obtained by adding the calculated stress drop to the uniform final stress following Olsen *et al.* (1997). Finally the slip weakening model (Ida, 1972) is used for fault constitutive relation in the dynamic modeling. An appropriate slip weakening distance is chosen by trial and error modeling in order to match the kinematic source inversion results. A larger slip weakening distance (0.5 m) is applied at the shallower depth (h<5km) than that (0.1 m) at greater depth (h > 5km) in order to approximate probable velocity hardening near the Earth's surface. Ide and Takeo (1997) also suggest a larger slip weakening distance near the surface. Our assumed value for τ_s places an upper bound on the size of the slip weakening distance, which otherwise might be smaller still since the fracture energy is the primary factor controlling the evolution of rupture (Guatteri and Spudich, 2000).

Reproduced with permission of the copyright owner. Further reproduction prohibited without permission.

Several questions arise regarding the uniqueness of our dynamic model. First, the homogeneous shear strength and final stress distribution calculated by the simple Byerlee's law might be unrealistically simple. The heterogeneous stress drop distribution tells us only that some combination of both the initial and final stress is responsible for the stress drop heterogeneity. Here we assume a uniform distribution of all dynamic source parameters except the initial stress, and incorporate the heterogeneous stress drop into the heterogeneous initial stress alone. Dynamic stress drop can also differ from static stress drop. Mikumo *et al.* (2003) also suggest heterogeneity in the distribution of the slip weakening distance. However, it is difficult to constrain different heterogeneities in dynamic source parameters independently from the given observed ground motions. Our approach is to start with a simple model that includes known heterogeneity and add complexity to the dynamic model as necessary in order to fit the kinematic model.

We used the 3-D finite difference code developed for the dynamic rupture simulation (Andrews, 1999). We also used the same layered velocity and density structure as used in the kinematic inversion (Ide and Takeo, 1997). The grid size and time step used are 0.5 by 0.5 km and 37 msec, respectively.

2.3. Results

Figure 3.3 compares the dynamic modeling results to the results obtained from waveform inversion (Ide and Takeo, 1997). Column (a), (b), (c) are snapshot images of the rupture propagation for the Kobe earthquake obtained from our dynamic modeling in terms of traction (MPa), slip (m), and slip velocity (m/s), respectively. The rupture is initiated by artificially

Reproduced with permission of the copyright owner. Further reproduction prohibited without permission.

forcing the initial stress drop to the final stress level (τ_f) in a circular nucleation zone (radius = 3 km). The forced stress drop starts at the hypocenter of the earthquake and continues to propagate inside the nucleation zone with the fixed rupture velocity (3 km/sec). The artificially initiated rupture near the high stress patch located at the center of the fault plane, thereafter, propagates as a self-sustaining (spontaneous) rupture throughout the first high stress patch as shown in the figure. It then traverses a narrow low stress band between the two high stress patches and propagates to the surface of Awaji island producing a large amount of slip beneath the island. Rupture on the farthest northeast reaches of the fault, near Kobe, occur after most of the southwest part of the rupture has completed. The relatively low initial stress beneath the city of Kobe and large slip weakening distance at shallow depth prevents surface rupture in this area. Column (b') and (c') are snapshot images of the rupture propagation obtained from waveform inversion (Ide and Takeo, 1997).

Since we took only the final slip distribution from the kinematic model to build the dynamic model, it is interesting to compare the spatio-temporal evolution of source parameters obtained from the dynamic modeling and kinematic inversion. The general trend of the rupture propagation as well as the final slip distribution shows a very good agreement. Figure 2.4 shows the comparison of the temporal accumulation of slip as obtained by the kinematic source inversion (solid) and the dynamic modeling (dashed), respectively. Even though we did not take any information except the final slip distribution from the kinematic model (i.e., no rupture time information), the rupture time distribution shows a clear similarity. The temporal evolution of slip is for the most part consistent between the two models. The most notable exception is immediately beneath the city of Kobe. It is surprising that we can model the behavior of this event with such a simple dynamic model that assumes largely uniform dynamic properties, with an especially simple fracture energy distribution.

Reproduced with permission of the copyright owner. Further reproduction prohibited without permission.

2.4. Discussion

Our very simple dynamic model of the Kobe earthquake produces kinematic motions on the fault consistent with the finite source inversion in terms of the slip and rupture time distribution even though the dynamic model is constructed using only the final slip distribution of the kinematic model. This supports the notion that reasonable estimates of the temporal evolution of slip in an earthquake can be inferred from the slip distribution alone (Guatteri *et al.*, 2003). There are several other slip models for the Kobe earthquake (Sekiguchi *et al.*, 1996; Wald, 1996; Yoshida *et al.*, 1996) and the details of those slip distributions are different, even though large-scale features, such as the location of asperities, agree with one another. We applied the same dynamic modeling approach to the slip model of Sekiguchi *et al.* (1996), which has a more strongly variable slip distribution and failed to generate kinematic motions consistent with the temporal evolution of rupture in their model. Our modeling approach may not be capable of producing highly variable dynamic models, unless we allow quantities, such as the fracture energy to be strongly variable.

Although there are strong tradeoffs between the slip weakening distance and the yield stress (Guatteri and Spudich, 2000), our assumed value for τ_s, which is just above the peak initial stress, places an upper bound on the size of the slip weakening distance, which otherwise would trade off with the peak stress and might be much smaller. Our analysis indicates that the smaller slip weakening distance (~ 0.1 m) than the estimate (0.5 ~ 1 m) of Ide and Takeo (1997) is required, especially near the nucleation area, for spontaneous rupture propagation. Our approach has some limitations for constraining the slip weakening distance of the Kobe

Reproduced with permission of the copyright owner. Further reproduction prohibited without permission.

earthquake due to the simplified assumptions we have made. In contrast to our model, heterogeneity in the distribution of the slip weakening distance has been suggested for this earthquake (Mikumo *et al.*, 2003). However, allowing the slip weakening distance to be heterogeneous greatly increases the degrees of freedom in the rupture modeling. We show both that the behavior of the slip weakening distance may be simple and that the slip weakening distance of the Kobe earthquake might be smaller than the estimate of Ide and Takeo (1997), as they mentioned based on their resolution analysis.

Our dynamic modeling approach can not uniquely constrain the distribution of dynamic parameters, however, simple and plausible dynamic models can be developed provided the slip model is relatively smooth.

Acknowledgements. We thank Joe Andrews for allowing us to use his dynamic simulation code (dynelf) and Satoshi Ide for giving us his kinematic inversion results for the Kobe earthquake. We thank Takashi Miyatake, Eiichi Fukuyama, David Oglesby, and Kim Olsen for helpful discussions. This research was sponsored by NSF grant CMS-0200436.

Reproduced with permission of the copyright owner. Further reproduction prohibited without permission.

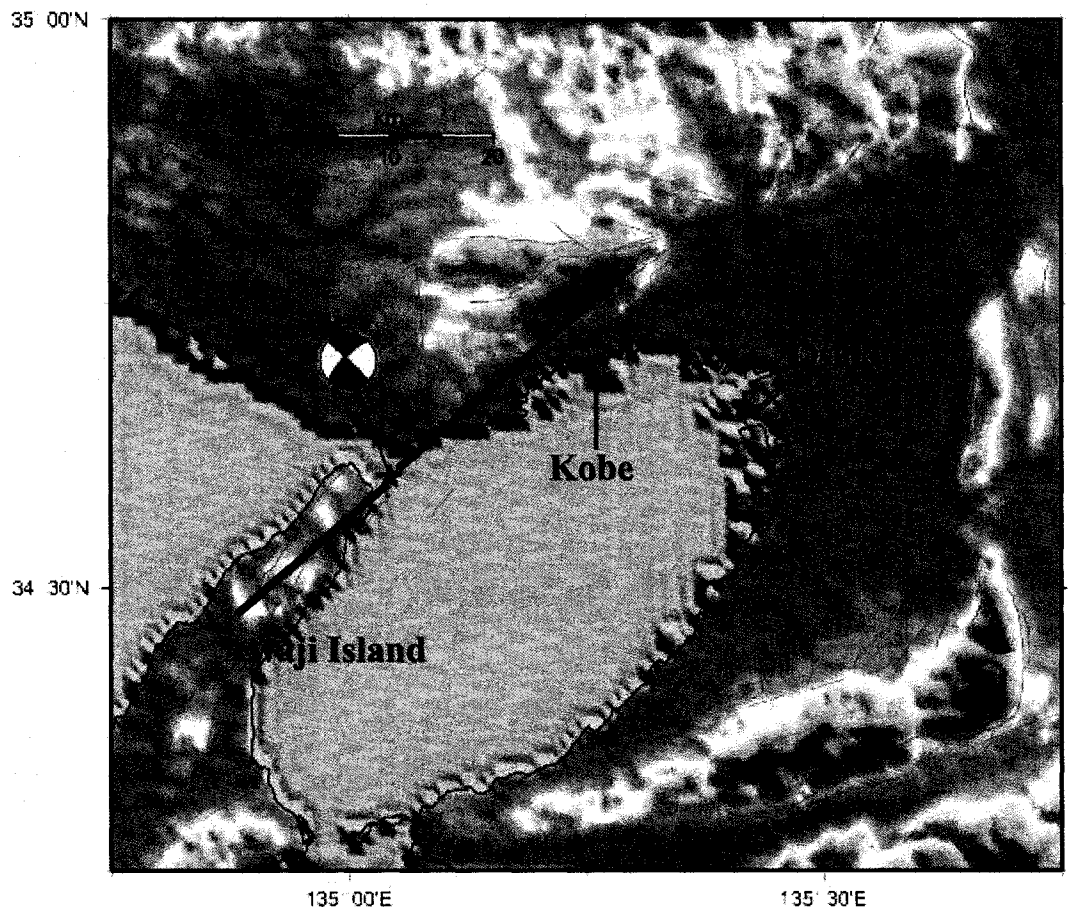

Figure 2.1. Map showing the focal mechanism and surface projection of the fault plane used by Ide and Takeo (1997) of the 16 January 1995 Kobe earthquake (Mw 6.9). It shows The Kobe earthquake was a right-lateral strike slip event on a nearly vertical fault whose ruptured area extends from Awaji island to Kobe.

Reproduced with permission of the copyright owner. Further reproduction prohibited without permission.

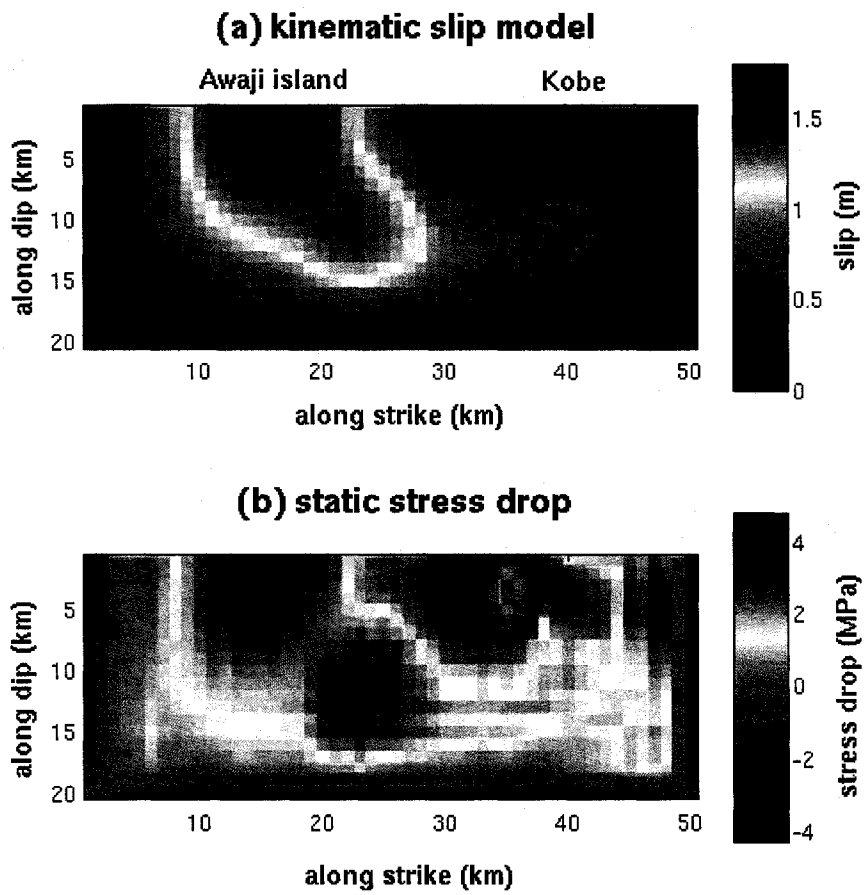

Figure 2.2. Final slip distribution of the Kobe earthquake obtained from kinematic source inversion (Ide and Takeo, 1997) and its static stress drop distribution calculated from the given slip model using the Okada's method (Okada, 1992), which calculates static stress drop from a given slip distribution in a homogeneous half space.

Reproduced with permission of the copyright owner. Further reproduction prohibited without permission.

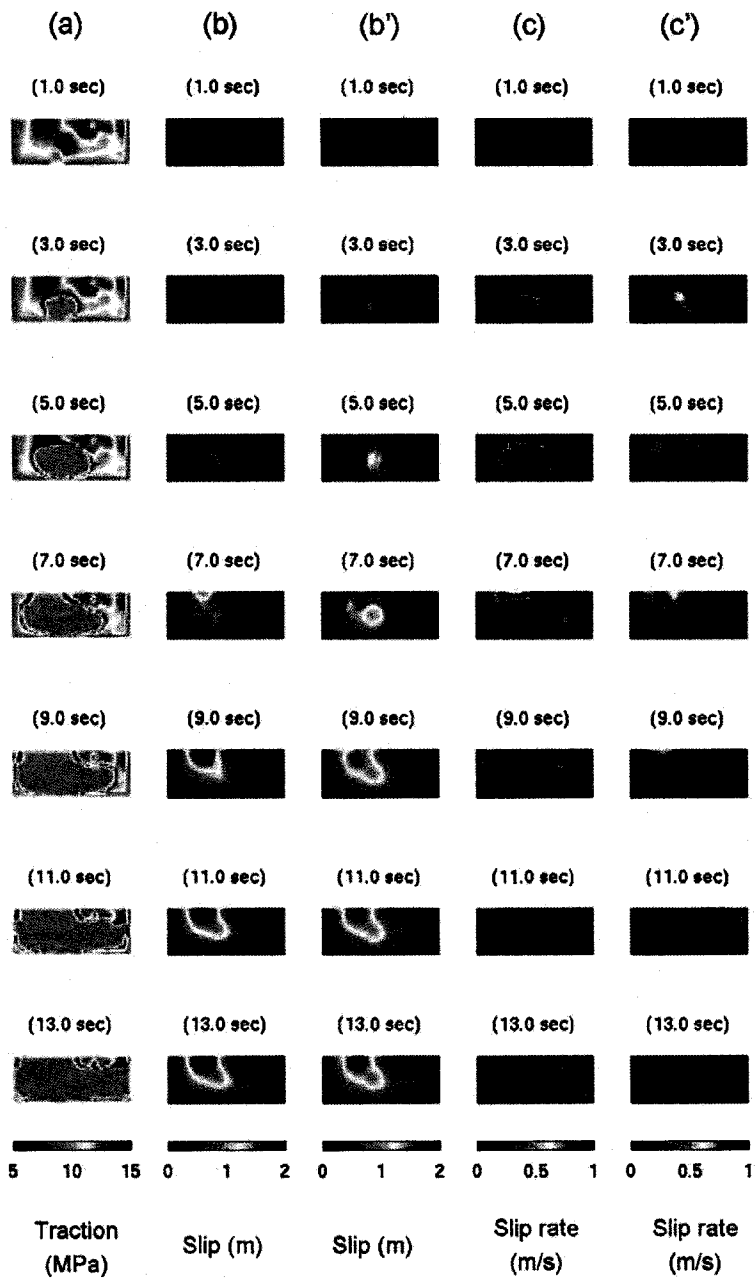

Figure 2.3. Snapshot images of the rupture propagation for the Kobe earthquake obtained from our dynamic modeling (Column (a), (b), (c)) and from waveform inversion (Column (b') and (c')), respectively. Each window (fault plane) has dimension of 20 km × 50 km.

Reproduced with permission of the copyright owner. Further reproduction prohibited without permission.

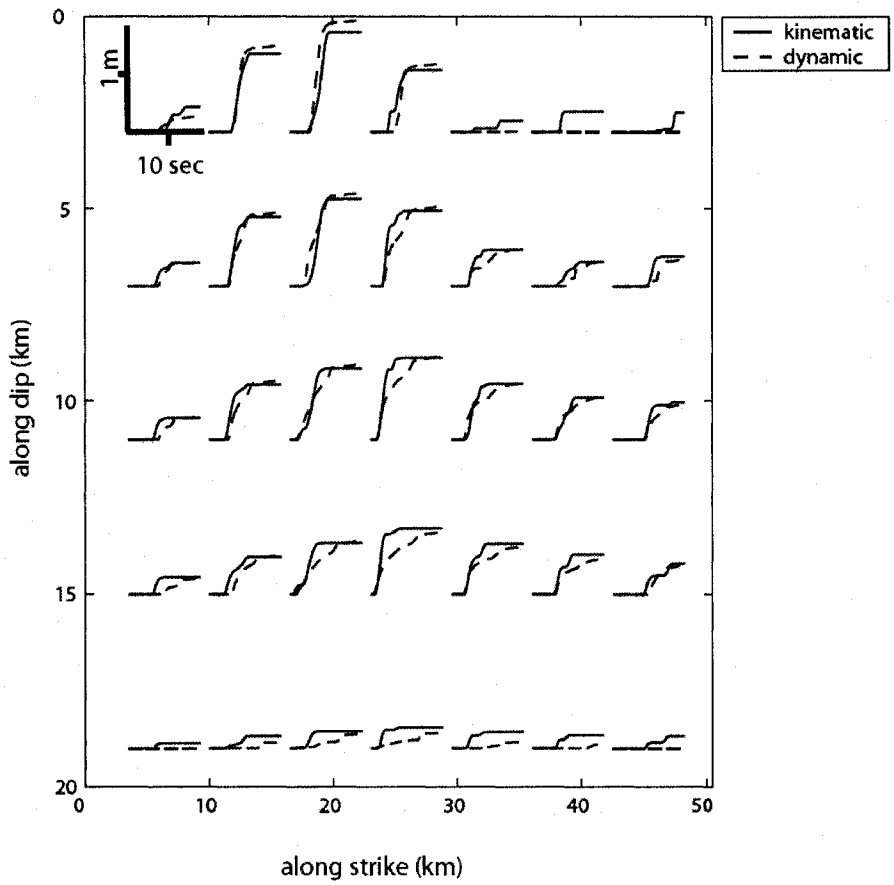

Figure 2.4. The comparison of the slip evolution obtained by the kinematic source inversion (solid) and the dynamic modeling (dashed), respectively.

Reproduced with permission of the copyright owner. Further reproduction prohibited without permission.

Chapter 3. Dynamic Rupture Models of Recent Large Earthquakes: Toward scaling of fracture energy and stress drop in dynamic rupture

This chapter consists of my contributions to the publication: P.M. Mai, P. Somerville, A. Pitarka, L. Dalguer, **S. Song**, G. Beroza, H. Miyake, and K. Irikura (2006). On Scaling of Fracture Energy and Stress Drop in Dynamic Rupture Models: Consequences for Near-Source Ground-Motions, AGU Chapman Monograph Series on Radiated Seismic Energy (*edited by R. Abercrombie, A. McGarr, H. Kanamori, and G. Toro*), 283-294.

Abstract

We have constructed spontaneous dynamic rupture models for three recent earthquakes in California including the Mw 6.9 1989 Loma Prieta, Mw 7.2 1992 Landers, and Mw 6.0 1987 Whittier Narrows earthquakes. Given slip models obtained from kinematic finite source inversions, stress drop is calculated and corresponding fracture energy is obtained by using simple assumptions or scaling. This avoids time-consuming trial and error procedure in the fracture energy estimation. Our dynamic models successfully reproduce slip and overall rupture duration of the kinematic models and in that sense they can be considered plausible, though non-unique, models to represent the dynamic rupture characteristics of the selected events. The constructed models, as well as other models developed by other research groups (Mai et al., 2006) are used to derive scaling relations for dynamic parameters (i.e., stress drop and fracture energy). These scaling relations can be used not only in constraining initial conditions in dynamic rupture modeling, but also in developing physics-based finite-source characterization tools for ground motion prediction (Guatteri et al., 2004).

Reproduced with permission of the copyright owner. Further reproduction prohibited without permission.

3.1. Introduction

Earthquakes can be considered dynamic fracture inside the Earth and earthquake rupture dynamics provides us with a unique opportunity to study the complex dynamic fracturing process and resulting ground motion characteristics with a physics-based approach (Madariaga, 1983; Kostrov and Das, 1988; Freund, 1990; Scholz, 1990). In the framework of earthquake rupture dynamics we now have a better understanding on how the earthquake rupture initiates, propagates, and stops, depending on applied stress conditions and friction laws on a fault plane. This leads to mixed boundary conditions involving slip and stress on the fault plane. Solutions for this problem are provided by many theoretical works (Kostrov, 1964; Kostrov, 1966; Burridge, 1973; Andrews, 1976a; Freund, 1979) in simple geometries. More complex 3-D problems with heterogeneous stress field can be handled with numerical modeling approaches.

Given initial stress conditions and known frictional behavior on a fault, it is relatively straightforward to model the dynamic rupture process and resulting ground motions using numerical dynamic rupture modeling techniques like finite difference (FD: Andrews, 1976b; Madariaga, 1976; Day, 1982a,b; Olsen et al, 1997) or boundary integral equations (BIE: Das and Aki, 1977; Fukuyama and Madariaga, 1995), but the inverse problem, to constrain the dynamic parameters from observed ground motions, introduces more challenging problems. So far no closed analytic expressions are developed to relate dynamic source parameters (e.q., stress drop and fracture energy) with either kinematic motions on a fault or ground motions on the surface. Thus constraining the dynamic parameters from the observed data requires time-

Reproduced with permission of the copyright owner. Further reproduction prohibited without permission.

consuming trial and error procedures because we need to adjust the dynamic parameters manually and perform the forward modeling numerous times, often several hundred iterations (Peyrat et al., 2001). In a spatially heterogeneous field the problem is even more challenging so that it is not only a time-consuming procedure, but many times we end up with different sets of dynamic estimates to reproduce band-limited (or low-pass filtered) ground motion data equally well. As a result, dynamic rupture models based on seismic data are highly non-unique.

Following the simple dynamic modeling of the 1995 Kobe, Japan, earthquake (Song and Beroza, 2004), we tried to develop simple, but plausible dynamic rupture models for three recent earthquakes in California. In formulating these models we attempted to reproduce the kinematic models that were developed to fit strong ground motion data. Our goal was to fit the final slip distribution and overall rupture duration. We placed much less emphasis on the temporal evolution of rupture, as that is typically much less well constrained in kinematic models. We recognize the non-uniqueness problem for the dynamic inversion. Thus our dynamic models must be considered only one of many possible models that reproduce the overall characteristics of the rupture process for the selected events and this must be kept in mind when we use our models to extract dynamic features of the earthquake rupture, such as developing scaling relations between dynamic parameters (Mai et al., 2006).

3.2. Spontaneous dynamic rupture modeling

In the spontaneous dynamic rupture modeling, earthquake rupture is completely controlled by the specified stress conditions and friction laws, in the sense that the direction and speed of the rupture front is fully determined by the boundary conditions and rupture criterion without any

Reproduced with permission of the copyright owner. Further reproduction prohibited without permission.

prescribed assumptions like fixed rupture velocity. Thus the spontaneous dynamic modeling provides a unique opportunity to understand the role that stress conditions and frictional behavior on a fault play in determining kinematic motions on the fault, and the resulting ground motions on the surface. Several key elements to define the boundary conditions and our systematic dynamic modeling procedure are described in the section below.

3.2.1. Stress drop and fracture energy

Stress drop controls many different features of earthquake rupture process. Final slip, rupture velocity, and peak slip rate at each point on a fault are all affected by stress drop distribution and its temporal decay patterns. Thus the stress drop is one of the primary input parameters in spontaneous dynamic rupture modeling; however, the dynamic stress drop we need in the modeling is hard to obtain since it depends on the whole temporal history of slip. Given the spatio-temporal evolution of slip on a fault, traction changes can be completely calculated by solving the elasto-dynamic equation of motion:

$$\rho \ddot{u}_i = \tau_{ij,j} . \tag{3.1}$$

ρ and $\ddot{u}_i$ are density and the second time-derivative of a displacement vector, respectively. $\tau_{ij,j}$ is spatial derivative of the stress tensor. The entire history of the temporal traction change can be extracted from kinematic models obtained from finite source inversion in this way and this has been used to understand various dynamic features of the rupture process such as the slip-weakening distance and fracture energy (Ide and Takeo, 1997; Tinti et al., 2005) and fault

Reproduced with permission of the copyright owner. Further reproduction prohibited without permission.

re-strengthening (Day et al., 1998). The reliability of the approach depends strongly on how accurately we can resolve the complete slip history on the fault. On the other hand, static stress drop is relatively easier to calculate because the estimate depends only on the final slip, not its temporal history. Solving the elasto-dynamic equation without the inertia term (eq. 3.2) will give us the static stress drop distribution.

$$\tau_{ij,j} = 0 \tag{3.2}$$

Even though the static stress drop is computed using only the final slip and differs from the dynamic stress drop given the same slip distribution; the dynamic stress drop can be either smaller than the static stress drop (dynamic overshoot), or vice versa (dynamic undershoot). Their actual difference may be small on the order of 10-20%, in most instances, compared to the uncertainty in finite-source inversion and consequent stress drop estimates (Madariaga, 1976; Day, 1982). We used the static stress drop as an input to our dynamic modeling. The static stress drop can be easily computed with several different approaches (Andrews, 1980; Okada, 1992). We used the Okada's method, in which a set of closed-form analytical solutions are used to calculate internal displacement and strain fields from shear or tensile faulting in a homogeneous half-space. We can take the free surface effect into account using Okada's method, which is not so easily done with whole space solutions (e.g., Andrews 1980).

Fracture energy (or surface energy) is defined as energy required to create unit crack surface (Andrews, 1976a), which indicates that energy should be absorbed by crack tip for propagation of the crack to occur. In Griffith theory, the crack can keep propagating if energy flowing into the crack tip is equal to the fracture energy (Scholz, 1990). Fracture energy distribution, as well as stress drop, plays a critical role in determining the evolution of fault

Reproduced with permission of the copyright owner. Further reproduction prohibited without permission.

rupture. In particular, it plays a dominant role in controlling the velocity of rupture front propagation (Andrews, 1976a; Guatteri and Spudich, 2000). Several studies have attempted to constrain fracture energy from real observed data (Beroza and Spudich, 1988; Guatteri et al., 2001; Peyrat et al., 2001; Rice et al., 2005; Tinti et al., 2005), but we are quite limited to constrain the fracture energy from the band-limited ground motion data or kinematic models constrained by the ground motion. As shown in a previous study (Song and Beroza, 2004), dynamic models with simple assumptions about the fracture energy distribution can reproduce target kinematic models successfully as long as the kinematic slip models are not too strongly spatially variable. We followed the same strategy here and tried to assign the fracture energy distribution by making relatively simple assumptions. The details are described in the modeling procedure section.

3.2.2. Fault constitutive law

Our knowledge about frictional behavior on a fault during rupture propagation, in particular, near the rupture front (crack tip), is critical in understanding rupture propagation characteristics. The slip-weakening law was first suggested by Ida (1972) and Andrews (1976a) to resolve the non-physical stress singularity when abrupt stress drop is assumed at the crack tip. In this friction law (Figure 3.1), traction change right behind the crack tip is controlled by the amount of slip. Once the crack tip passes and the fault starts slipping, the traction decays as a function of slip until the slip reaches the slip weakening distance (d_c). Thereafter it remains at the final stress level without any re-strengthening. Under this law, the frictional behavior on the fault is fully described by four parameters: initial and final stress, yield stress, and the slip weakening distance. Since our knowledge of the absolute level of

Reproduced with permission of the copyright owner. Further reproduction prohibited without permission.

stress field in active fault zones is limited and because band-limited ground motions are less sensitive to the absolute stress level, it is more reasonable to focus on their differences like stress drop and strength excess as defined in Figure 3.1. We can further simplify our parameterization using the fracture energy, which seems to be better constrained by observed ground motions than the yield stress and slip weakening distance (Guatteri and Spudich, 2000). The shaded area in Figure 3.1 indicates the fracture energy which can be computed by the yield stress and slip weakening distance in the slip weakening law.

3.2.3. Modeling procedure

It is straightforward to constrain kinematic motions on a fault from observed ground motions, at least in theory, because the resulting ground motions are clearly related to the kinematic motions on the fault if propagation effects (Green's function) are known. Most derivative-based inversion methods, however, do not perform well for dynamic parameter estimation and past studies have tended to use forward (iterative) modeling for this purpose (Ide and Takeo, 1996; Peyrat et al., 2004). In addition ground motions, especially band-limited low frequency data, are less sensitive to many of dynamic parameters. For example it is difficult to differentiate the effects of the strength excess and slip-weakening distance from strong motion data (Guatteri and Spudich, 2000). It is also difficult to constrain the level of absolute stress. Several studies have attempted to estimate dynamic parameters directly from observed data or to constrained kinematic rupture models (Fukuyama and Mikumo, 1993; Mikumo and Miyatake, 1995; Ide and Takeo, 1996; Beroza and Mikumo, 1996; Peyrat et al., 2001; Peyrat et al., 2004), however their results show that many different combinations of the estimated

Reproduced with permission of the copyright owner. Further reproduction prohibited without permission.

dynamic parameters can fit well not only the kinematic models on the fault, but also the observed ground motions.

Instead of the time-consuming iterative trial and error modeling, or computationally intensive statistical optimization methods to obtain a single best dynamic rupture model, we decided to adopt a simple procedure to obtain plausible dynamic models that reproduce estimated kinematic motions reasonably well. Even though our model is not unique, it is a plausible dynamic model in a sense that it contains primary features of the dynamic rupture for the target event.

Figure 3.2 shows the flowchart of our dynamic modeling procedure. Given slip models from various kinematic inversion studies, the static stress drop distribution is computed by Okada's method (1992) and added to a constant final stress level (τ_f) to construct initial stress field (τ_o). The static stress drop is scaled by a factor of ~ 0.9 to account for the effect of dynamic overshoot effect as mentioned above and to produce roughly the same amount of slip as that of the kinematic model, but the amplitude of the effect is not always the same because we deal with a heterogeneous field. As shown in Figure 3.3 (a), the constant yield stress model was quite successful in reproducing kinematic motions in the previous study (Song and Beroza, 2004) since the chosen kinematic slip model is relatively smooth (Ide and Takeo, 1997). That assumption doesn't seem to work for all cases, in particular when slip distribution is highly variable and rupture is initiated at a low slip zone. The rupture often stops in the middle instead of propagating through to the fault boundaries. Here we adopted more flexible assumptions to avoid the premature termination of the rupture, i.e., constant strength excess (Figure 3.3, (b)). Instead, the initial and final stress field are assigned in the same ways in the constant yield stress model, but the yield stress is constructed with constant strength excess as

Reproduced with permission of the copyright owner. Further reproduction prohibited without permission.

shown in Figure 3.3. In the negative stress drop region, the yield stress is set to be equal to the final stress level to prevent the static friction level from being lower than the sliding friction. The slip-weakening distance is assumed to be a spatially constant value in this modeling. We used the 3-D finite difference dynamic code developed by Andrews (1999). It allows for material heterogeneity, non-vertical faulting, and the effect of the Earth's free surface on dynamic rupture.

Our primary purpose in this modeling is to investigate the earthquake rupture propagation process. The interesting questions of how the rupture is initiated and terminated, is not our focus. As in many dynamic rupture modeling studies, we artificially initiated the rupture. Our approach was to lower the stress from its initial to final level within a circular shape of initial nucleation patch (radius ~ 2.5 km). The rupture is constrained to propagate at a constant speed of ~ 3.0 km/sec within the patch, but is allowed to propagate spontaneously after that. The minimum crack length required to guarantee continuous crack propagation can be pre-calculated using assigned dynamic quantities in the homogeneous case (Andrews, 1976a; Day, 1982b) and the approach works well for the heterogeneous stress case as well. Regarding the termination of the rupture, we can use either very low initial stress or very high yield stress outside the assumed faulting area. In either case the stress fields are tapered to minimize unrealistic boundary effects arising from the abrupt change.

3.3. Dynamic models

3.3.1. 1989 Loma Prieta earthquake (Mw 6.9)

Reproduced with permission of the copyright owner. Further reproduction prohibited without permission.

The Loma Prieta earthquake occurred to the southwest of the San Andreas fault (in the southern Santa Cruz Mountains). It is an oblique dip-slip event (rake: 135°, dip: 70°) with the shallowest slip extending to approximately 5 km depth. Several finite source models were obtained by inverting strong-motion and teleseismic data (Beroza, 1991; Steidl et al., 1991; Wald et al., 1991). These models show that rupture initiated in the middle of about 35 km along-strike rupture and propagated bi-laterally, with a region of concentrated high slip on both sides. We developed a plausible dynamic model for the event to reproduce kinematic slip from the finite source inversion following the modeling procedure described above. We used the kinematic slip model obtained by Beroza (1991). Some key parameters and the 1-D velocity structure used in the modeling are listed in Table 3.1 and 3.2, respectively. We would have determined different dynamic models if other kinematic models were used, but those variations are the level of uncertainty in the kinematic models.

In order to set up an initial dynamic rupture model, static stress drop is computed from the slip distribution using Okada's method (1992) and added to a uniform final stress. The static stress drop is not scaled to account for the dynamic overshoot since the static drop itself produced the kinematic slip well in this case. Trial and error modeling was used to determine the level of the uniform strength excess, 50% of the mean stress drop, i.e. 1.8 MPa, is added to the initial stress to construct the yield stress. The yield stress in the negative stress drop region is set to be the same as the uniform final stress level to prevent the yield stress from being below the final friction level. Finally, a uniform 0.5 m slip weakening distance is assigned for the whole rupture area after several trials of different values.

Figure 3.4 shows the dynamic modeling results for the Loma Prieta earthquake. The dynamic slip model successfully captures all the main features of the spatially variable kinematic slip

Reproduced with permission of the copyright owner. Further reproduction prohibited without permission.

without much of the smoothing effect often observed in the dynamic model (Peyrat et al., 2001). The constant strength excess model seems to be useful to reproduce spatially variable slip distribution by dynamic modeling, but it often generates high rupture velocity and peak slip rate, particularly where slip is large, possibly because no high strength excess/low prestress barriers exist in this model. In order to remove this problem, we adopted the empirical scaling relations between fracture energy (G_c) and stress intensity factor ($\Delta\sigma * L^{1/2}$) suggested by Guatteri et al. (2004) as shown in Figure 3.5. Thus we expect larger strength excess in the asperity area, and the strength excess increases as the rupture propagates from the initial nucleation area. The new yield stress produces better results both in terms of rupture velocity and peak slip rate compared to the previous constant strength excess model. The rupture time distribution in Figure 3.4 shows that overall rupture duration has values consistent with the kinematic inversion (Beroza, 1991), implying that we can construct a plausible dynamic model, with simple assumptions in the model construction, to reproduce primary parameters in the kinematic model such as final slip and rupture duration.

3.3.2. 1992 Landers earthquake (Mw 7.2)

The 1992 Landers earthquake occurred in the Mojave Desert in southern California on a series of 3 principal right-lateral strike-slip fault segments (e.q., Landers-Johnson Valley, Homestead Valley, and Camp Rock-Emerson Valley). It is one of the well-recorded and well-studied earthquakes in California and several finite-source models have been obtained by analyzing strong motion, teleseismic and geodetic (GPS and InSAR) data (Cohee and Beroza, 1994; Wald and Heaton, 1994; Cotton and Campillo, 1995; Hernandez et al., 1999). There have also been several studies that developed dynamic rupture models for this event (Olsen et al., 1997;

Reproduced with permission of the copyright owner. Further reproduction prohibited without permission.

Peyrat et al, 2001) starting from one of the kinematic models (Wald and Heaton, 1994). We developed a dynamic model using the kinematic rupture model developed by Cohee and Beroza (1994) to add one more plausible dynamic model for this event, considering the non-uniqueness in the dynamic modeling, and also to develop a more systematic way of modeling construction that will avoid tedious manual perturbation in the dynamic model construction, which often requires hundreds of iterations (Peyrat et al., 2001).

As mentioned above, the Landers earthquake is a vertical strike-slip event that ruptured over at least three distinct fault segments. In our modeling we simplify the true behavior of the Landers earthquake by assuming that rupture occurred on a simple planar fault. The dynamic stress drop is obtained after scaling the computed static stress drop by a factor of 0.9 in order to correct for dynamic overshoot. Similar approaches used in the Loma Prieta earthquake modeling were adopted to construct the yield stress, with a 0.5 m slip weakening distance determined after several trial and error modeling procedures. 0.8 m slip weakening distance is suggested for the Landers earthquake by previous dynamic modeling studies (Olsen et al., 1997; Peyrat et al, 2001). Our estimate is within a reasonable range compared with them although we are limited to estimate the accurate slip weakening distance in this modeling, just fitting the final slip and overall rupture duration. Modeling parameters and velocity structure used in the modeling are listed in Table 3.3 and 3.4, respectively. For the Landers earthquake, high stress drop regions are located near the surface, in particular, in the middle of the fault, that can lead to an unrealistic large surface rupture (large slip) due to the free surface effect in the dynamic modeling. This can be prevented by using a velocity strengthening friction law near the surface, but we chose to taper the stress drop near the surface and retain the slip weakening instead. The negative stress drop regions between the nucleation and high stress drop areas cause the rupture to be delayed for several seconds or stopped, which is not evident

Reproduced with permission of the copyright owner. Further reproduction prohibited without permission.

in the kinematic model, so we reduced the negative stress drop by a half in this region to allow the earthquake to propagate spontaneously across this part of the fault. After these adjustments, the dynamic modeling reproduces the kinematic final slip distribution successfully (Figure 3.6). Super-shear rupture is observed over a limited region in the high stress drop area for the dynamic model.

3.3.3. 1987 Whittier Narrows earthquake (Mw 6.0)

The 1987 Whittier Narrows earthquake is a moderate-sized event (Mw 6.0), but it raised concerns because it occurred within the major metropolitan area of Los Angeles in the form of a blind-thrust event, with no rupture shallower than approximately 10 km depth. It also has a small dip angle (30°) with a rake of 150°. It is also of interest because it is an example of a "buried" rupture and there is some evidence that such earthquakes have different strong motion characteristics (Somerville, 2003). We developed a dynamic rupture model using the kinematic slip obtained by strong motion data analysis by Hartzell and Iida (1990), following the same modeling procedure above. The static stress drop is scaled by a factor of 0.8 to account for the dynamic overshoot and 50% of the mean stress drop (0.6 MPa) was added to the initial stress to build up the yield stress. Some modeling parameters and velocity structure used in the modeling are listed in Table 3.5 and 3.6, respectively. The constant strength excess model was used here with a 0.3 m slip weakening distance. The Whittier Narrows earthquake has a relatively small rupture area (10 km by 10 km). Since a circular region with a radius of 2.5 km was used as an initial nucleation area in the dynamic modeling near where large slip occurs, the heterogeneity of the slip distribution in the center of the rupture area could not be

Reproduced with permission of the copyright owner. Further reproduction prohibited without permission.

well reproduced. However, the overall dimension of the final slip and rupture time distribution is well reproduced (Figure 3.7).

3.4. Scaling of fracture energy and stress drop

Estimating the fracture energy distribution requires laborious trial and error procedure even with well constrained kinematic motions on a fault as well as well recorded observations. Thus scaling relations of fracture energy with well-defined parameters like stress drop are very useful. They can be used in both determining initial conditions for dynamic rupture modeling and as the basis for physics-based (pseudo-dynamic) earthquake source characterization for ground motion prediction (Guatteri et al., 2004).

The dynamic models developed in the study, with dynamic models obtained by other research groups, are used for analyzing the scaling properties of fracture energy and stress drop (Mai et al., 2006). Following Guatteri et al. (2004), we investigated the fracture energy scaling with respect to the stress intensity factor ($\Delta\sigma * L^{1/2}$, stress drop times square root of crack length). Figure 3.8 shows the scaling results obtained from 12 dynamic rupture models of 9 well-recorded moderate to large earthquakes. Clear scaling of fracture energy with the stress intensity factor is observed in the plots. These results are encouraging because dynamic models used in the analysis are obtained from different groups with different dynamic modeling schemes and kinematic source models.

The scaling relations behave differently in surface vs. subsurface rupture earthquakes, i.e., fracture energy increases significantly faster with the stress intensity factor for the surface

Reproduced with permission of the copyright owner. Further reproduction prohibited without permission.

rupture earthquakes than for the subsurface rupture, indicating that surface breaking events consume more fracture energy than buried events. These results are consistent with the observation that recorded ground motions from earthquakes that produce large surface rupture are systematically weaker than those from buried events (Somerville, 2003). This phenomenon could be explained in dynamic rupture modeling with either velocity strengthening friction, or large fracture energy at shallow depths (Pitarka et al., 2005).

3.5. Discussion

It is not uncommon that several different kinematic models are determined even for the same event by different research groups. These models will differ due to the non-uniqueness inherent in this underdetermined inverse problem, and depends on the data and methods used. For example, the 1992 Landers, California, earthquake has several kinematic source models obtained by different groups (Cohee and Beroza, 1994; Wald and Heaton, 1994; Cotton and Campillo, 1995; Hernandez et al., 1999). Even though they share some common macroscopic features, such as the location of the high-slip regions, these models have significant dissimilarities. Since we construct dynamic models by reproducing kinematic models with them, it is natural to question the uniqueness of the constructed models. As mentioned previously, our primary goal is to produce a set of plausible dynamic models that capture the overall features of the targeted dynamic models, and ultimately to use them to develop realistic models for ground motion simulation.

Our simple dynamic model of the three recent major earthquakes in California produces kinematic motions on the fault consistent with the finite-source inversion in terms of the slip

Reproduced with permission of the copyright owner. Further reproduction prohibited without permission.

and rupture time distribution, even though the dynamic model is constructed using only the final slip distribution of the kinematic model. This supports the notion that reasonable estimates of the temporal evolution of slip in an earthquake can be inferred from the slip distribution alone (Guatteri et al., 2003). It is encouraging that plausible dynamic models can be constructed only with given final slip distribution. Since it is much easier to synthesize feasible finite-slip models for future scenario earthquakes than the entire slip history (Mai and Beroza, 2002), we can obtain all the finite-source parameters we need in order to simulate near-field ground motions by the dynamic rupture modeling by starting with the synthesized slip models (Guatteri et al., 2003).

Reproduced with permission of the copyright owner. Further reproduction prohibited without permission.

Table 3.1. 1989 Loma Prieta earthquake

Kinematic slip model	Beroza, 1991
Event Type	Oblique dip-slip (dip = 70°, rake = 135°)
d_c	0.5 m
Grid size	dx = 170 m, dy = 500 m, dz = 470 m
Time increment	dt = 19 msec

Table 3.2. 1-D Velocity structure used in the Loma Prieta earthquake modeling

Top depth (km)	Vp (km/sec)	Vs (km/sec)	Density (g/cm3)
0.0	1.730	1.000	1.500
0.1	3.380	1.950	1.550
0.5	4.290	2.480	1.850
1.0	4.800	2.770	2.050
3.0	5.370	3.100	2.260
5.0	5.740	3.310	2.450
7.0	6.150	3.550	2.580
9.0	6.250	3.610	2.620
13.0	6.270	3.620	2.630
18.0	6.670	3.850	2.770
25.0	8.000	4.620	3.280

Reproduced with permission of the copyright owner. Further reproduction prohibited without permission.

Table 3.3. 1992 Landers earthquake

Kinematic slip model	Cohee and Beroza, 1994
Event Type	Vertical strike-slip (dip = 90°, rake = 180°)
d_c	0.5 m
Grid size	dx = 500 m, dy = 500 m, dz = 500 m
Time increment	dt =36 msec

Table 3.4. 1-D Velocity structure used in the Landers earthquake modeling

Top depth (km)	Vp (km/sec)	Vs (km/sec)	Density (g/cm3)
0.0	3.8	1.98	2.3
1.5	5.5	3.15	2.6
4.0	6.2	3.52	2.7
26.0	6.8	3.83	2.87
32.0	8.0	4.64	3.5

Reproduced with permission of the copyright owner. Further reproduction prohibited without permission.

Table 3.5. 1987 Whittier Narrows earthquake

Kinematic slip model	Hartzell and Iida, 1990
Event Type	Oblique dip-slip (dip = 30°, rake = 150°)
dc	0.3 m
Grid size	dx = 433 m, dy = 500 m, dz = 250 m
Time increment	dt = 24.8 msec

Table 3.6. 1-D Velocity structure used in the Whittier Narrows earthquake

Top depth (km)	Vp (km/sec)	Vs (km/sec)	Density (g/cm3)
0.0	3.8	1.98	2.3
1.5	5.5	3.15	2.6
4.0	6.2	3.52	2.7
26.0	6.8	3.83	2.87
32.0	8.0	4.64	3.5

Reproduced with permission of the copyright owner. Further reproduction prohibited without permission.

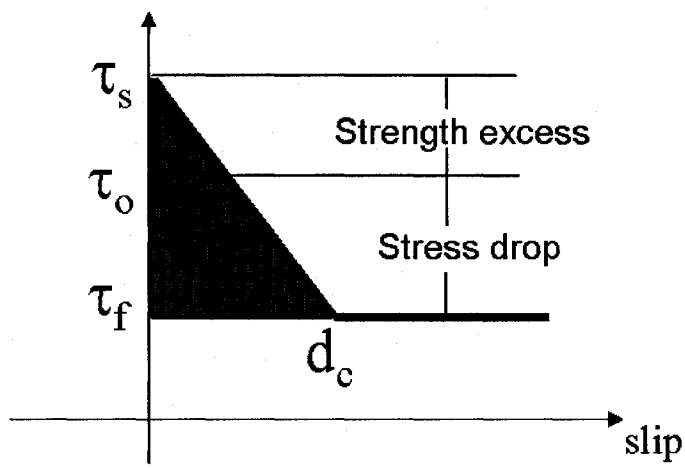

Figure 3.1. Slip-weakening friction law (Ida, 1972; Andrews, 1976a). τ_o, τ_f, and τ_s indicate initial, final, and yield stress (or rock strength), respectively. d_c denotes the slip weakening distance and the gray area represents fracture energy. In this friction law, traction on a fault decays as the fault starts slipping as a function of slip until the slip reaches the slip weakening distance and it remains at the final stress level without any fault re-strengthening procedure until the end of the slipping.

Reproduced with permission of the copyright owner. Further reproduction prohibited without permission.

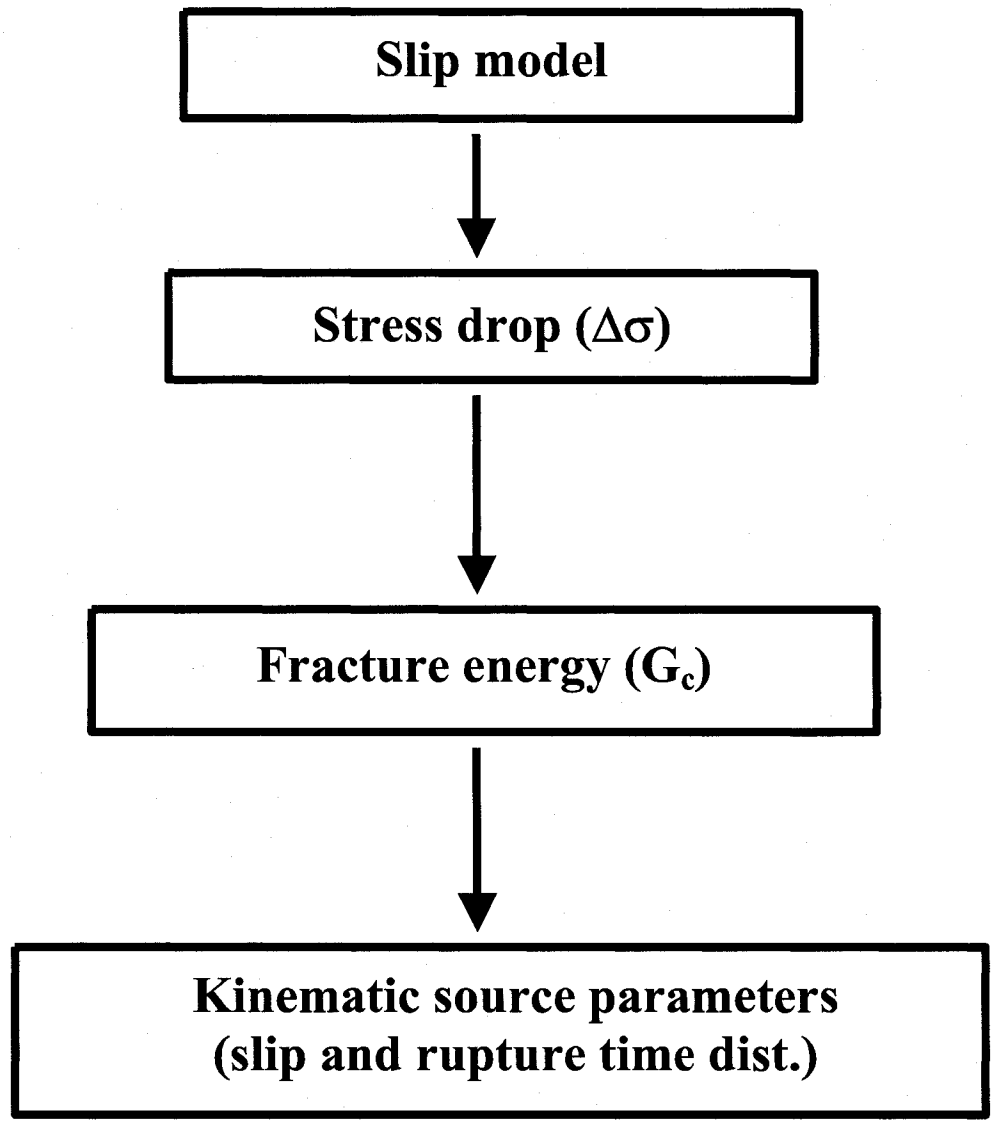

Figure 3.2. Flowchart of the dynamic modeling procedure.

Reproduced with permission of the copyright owner. Further reproduction prohibited without permission.

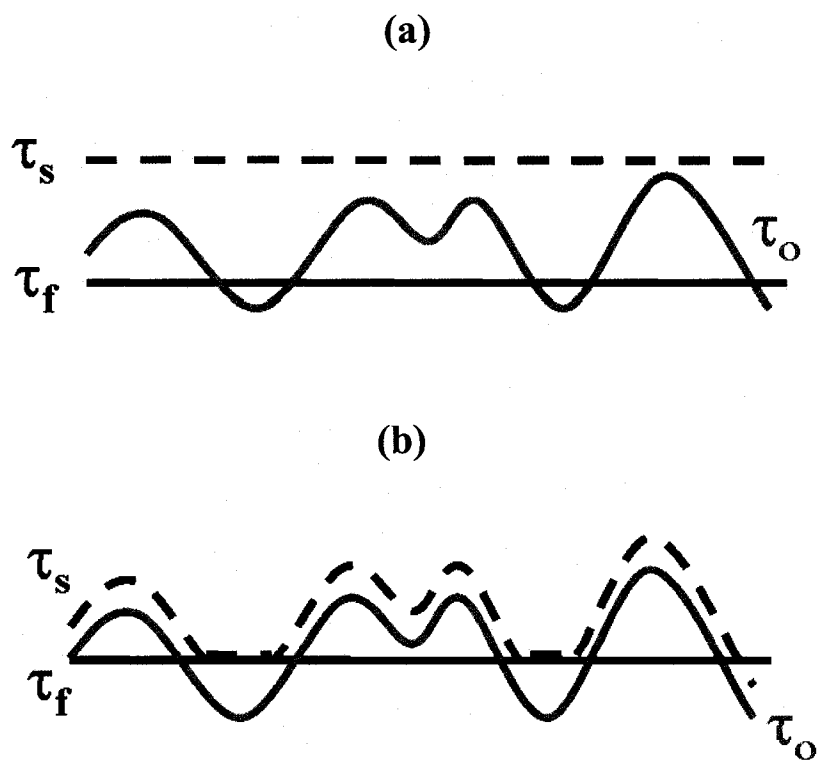

Figure 3.3. Two simple dynamic rupture models. (a) Constant yield stress. Final stress is assumed to be distributed uniformly. And a heterogeneous stress drop distribution is added to it to construct an initial stress field. A uniform yield stress is assumed to be located above the maximum initial stress field. (b) Constant strength excess. Initial and final stress field are assigned in the same ways in the constant yield stress model, but the yield stress is constructed with the strength excess constant as shown in the figure. In the negative stress drop region, the yield stress is set to be equal to the final stress level to prevent the static frictional level from being smaller than the sliding frictional level.

Reproduced with permission of the copyright owner. Further reproduction prohibited without permission.

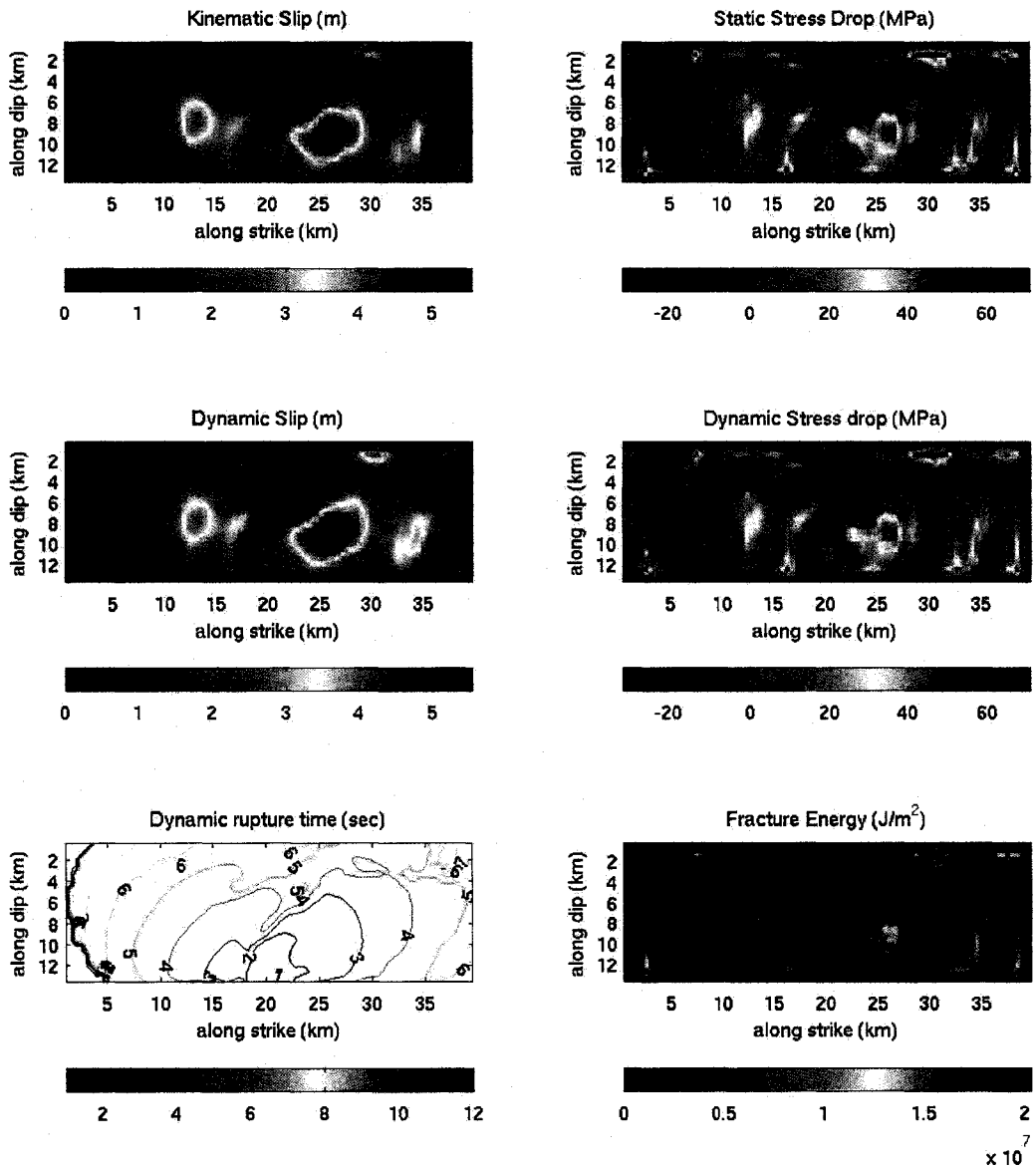

Figure 3.4. Dynamic modeling results of the 1989 Loma Prieta earthquake. Stress drop and fracture energy distribution used in the modeling are shown on the right panel. The kinematic slip model (Beroza, 1991) is successfully reproduced by the dynamic modeling and overall duration of rupture is also reasonable.

Reproduced with permission of the copyright owner. Further reproduction prohibited without permission.

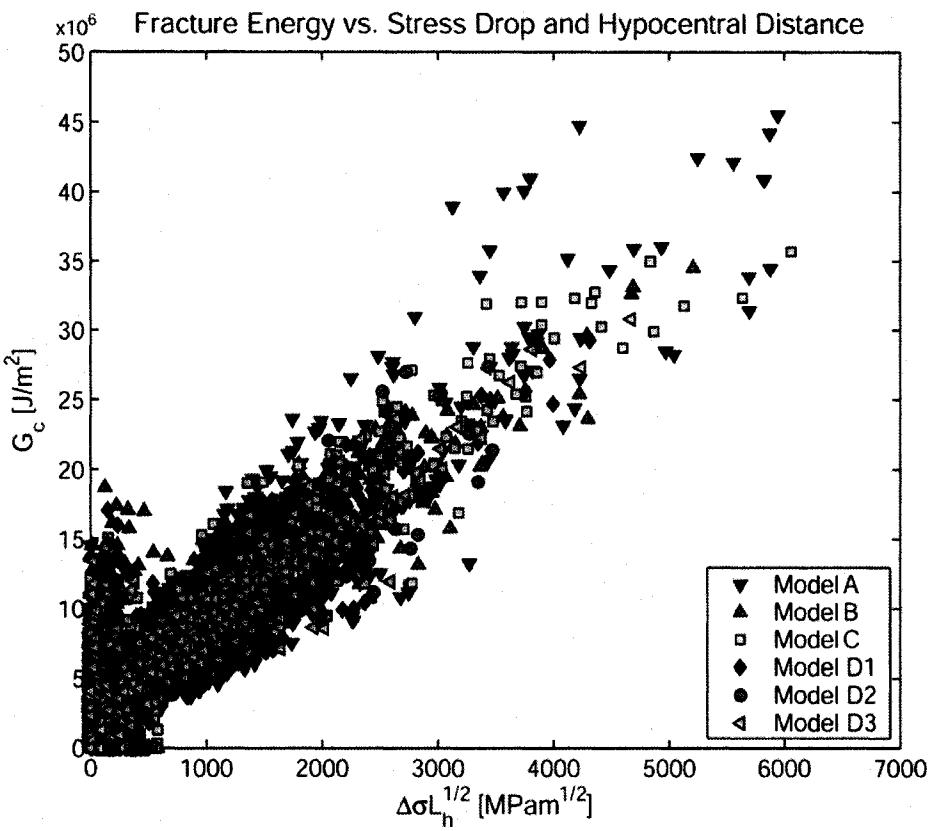

Figure 3.5. Fracture energy scaling with stress intensity factor (stress drop times square root of crack length) shown in Guatteri et al. (2004). A clear linear relation is observed between two parameters.

Reproduced with permission of the copyright owner. Further reproduction prohibited without permission.

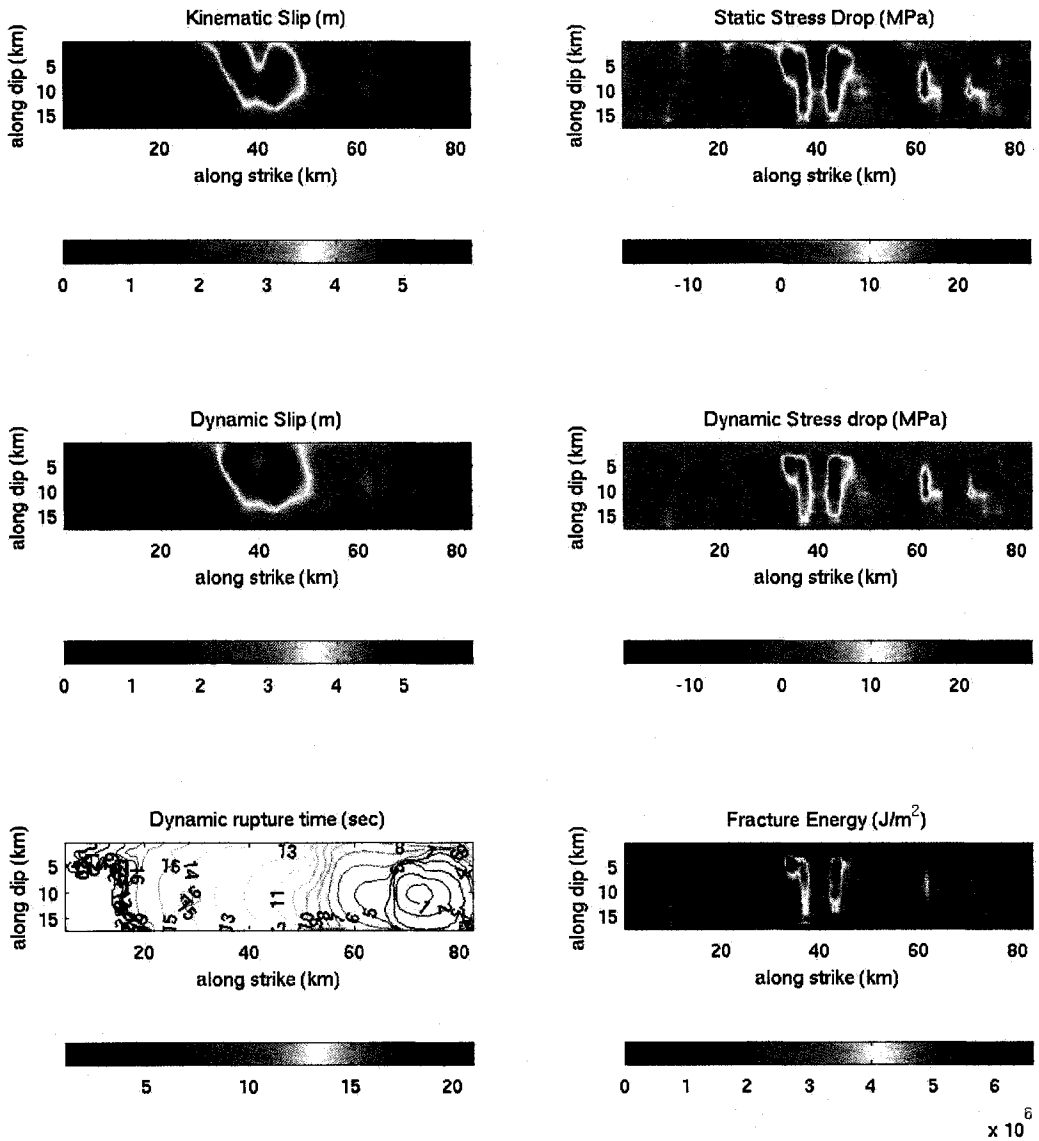

Figure 3.6. Dynamic modeling results for the 1992 Landers earthquake. Stress drop and fracture energy distribution used in the modeling are shown on the right panel. The kinematic slip model (Cohee and Beroza, 1994) is successfully reproduced by the dynamic modeling and overall duration of rupture is reasonable, though parts of the rupture are super-shear in the dynamic model.

Reproduced with permission of the copyright owner. Further reproduction prohibited without permission.

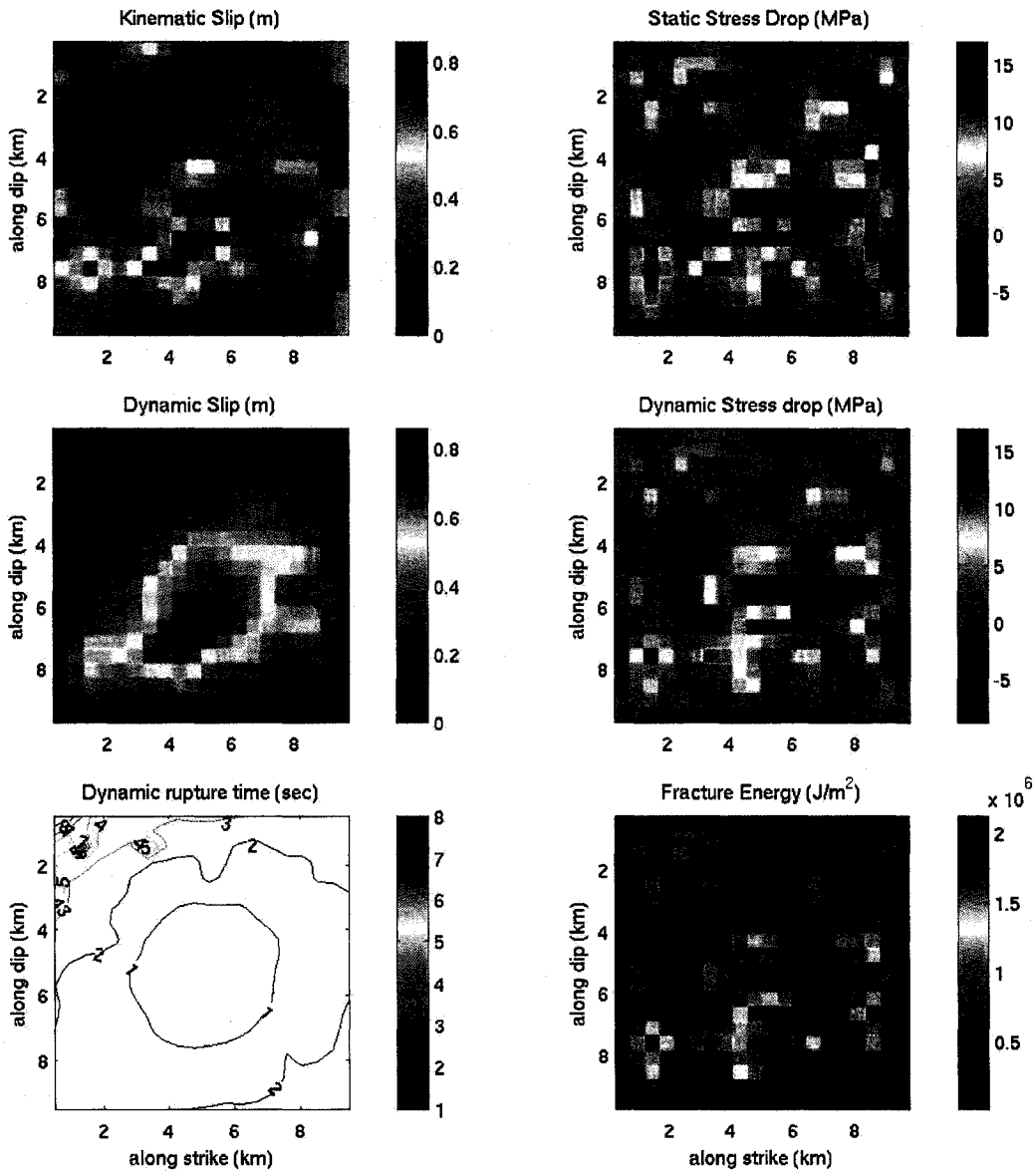

Figure 3.7. Dynamic modeling results of the 1987 Whittier Narrows earthquake. Stress drop and fracture energy distribution used in the modeling are also shown on the right panel. The kinematic slip model (Hartzell and Iida, 1990) is successfully reproduced by the dynamic modeling and overall duration of rupture also seems reasonable.

Reproduced with permission of the copyright owner. Further reproduction prohibited without permission.

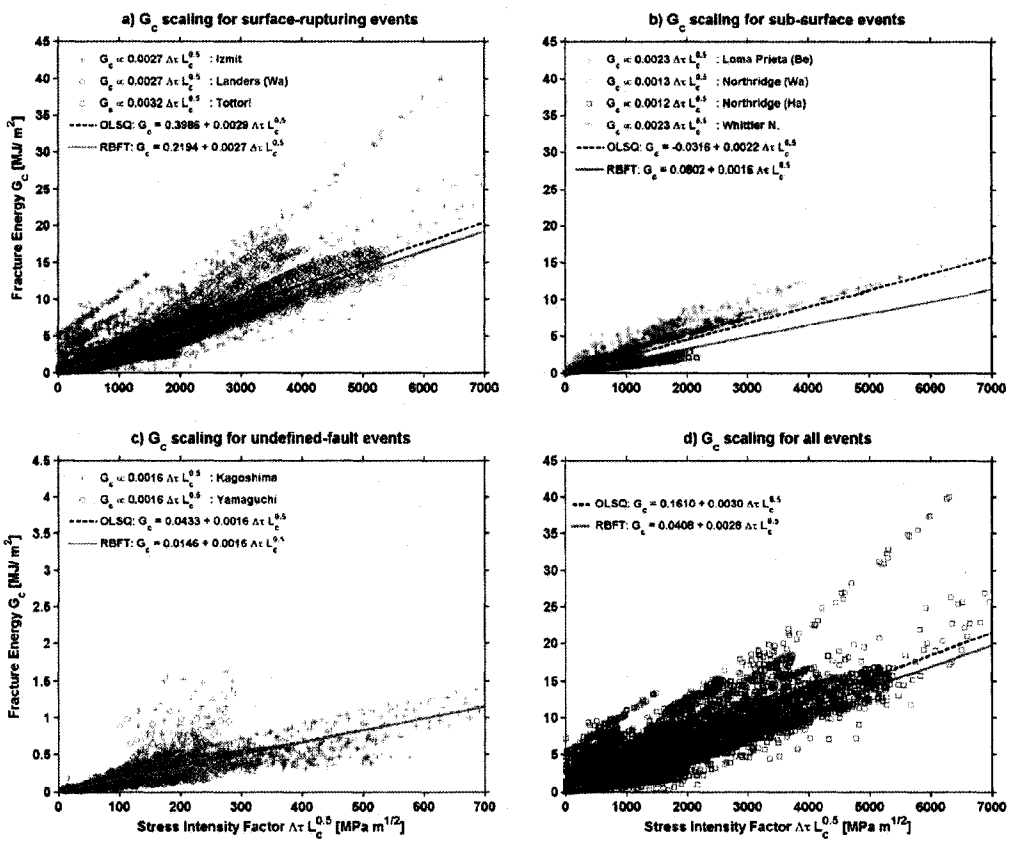

Figure 3.8. Scaling of fracture energy with stress intensity factor obtained by Mai et al. (2006). Overall fracture energy is scaled with the stress intensity factor in all events. More interestingly the scaling relations appear differently in surface and subsurface rupture earthquakes, i.e., fracture energy increases significantly faster with the stress intensity factor for the surface rupture earthquakes than for the subsurface rupture, indicating that surface breaking events consume more fracture energy than buried events.

Reproduced with permission of the copyright owner. Further reproduction prohibited without permission.

Chapter 4. A Unified Source Model for the 1906 San Francisco Earthquake

Accepted in Bull. Seism. Soc. Am. (2008), A Special issue on the 1906 San Francisco Earthquake. A little modification from the accepted version.

Abstract

We reconcile two previously discordant source models of the 1906 San Francisco earthquake and obtain a model that satisfies both triangulation and seismic data by allowing the rupture velocity to exceed the shear wave velocity. Employing a projection method to remove the dependence on initial station positions allowed us to make use of a more stable triangulation network, including non-repeated angle observations along the northern San Andreas fault. This strengthens the case for significant slip over the entire northern segment of the San Andreas fault from San Juan Bautista to Cape Mendocino during the 1906 earthquake. We also found that the teleseismic body wave data can be reconciled with the geodetically derived slip model by allowing super-shear rupture. This resolves a longstanding conflict between the two previous slip models (geodetic and seismic) of this earthquake. Super-shear rupture has long been recognized as a theoretical possibility for strike-slip faulting, and it has been observed in several recent large strike-slip earthquakes, which raises the prospect that it might be typical for such events. Super-shear rupture leads to substantially different strong ground motion and as a result, may need to be taken into account when developing ground motion prediction relations for large strike-slip earthquakes. Our final slip model has a seismic moment of 7.9×10^{20} N-m, which corresponds to a moment magnitude of Mw 7.9

Reproduced with permission of the copyright owner. Further reproduction prohibited without permission.

4.1. Introduction

The 1906 San Francisco earthquake ruptured the northern segment of the San Andreas Fault at the dawn of the twentieth century and is perhaps the single most important earthquake in the history of earthquake science (Figure 4.1). Despite the importance of the earthquake, the two most recently published source models, one based on geodetic data (Thatcher *et al.*, 1997) and the other based on seismic data (Wald *et al.*, 1993), differ substantially from one another, particularly in the total rupture length as shown in Figure 4.2. The geodetic slip model maps slip from San Juan Bautista to Cape Mendocino (~500 km rupture length); whereas, the seismic model finds almost no slip north of Point Arena (~300 km rupture length). We find that these two models can be reconciled if the rupture velocity exceeded the shear wave velocity of the Earth's crust north of San Francisco.

While it is often assumed that earthquake rupture velocity does not exceed the Rayleigh wave velocity, theoretical studies indicate that in-plane rupture can propagate at inter-sonic speeds; i.e., between the *S*-wave and the *P*-wave velocities (Burridge, 1973; Andrews, 1976b). Recent large strike-slip earthquakes: the 1999 Izmit, Turkey; the 2001 Kunlunshan, Tibet; and the 2002 Denali events, have all exhibited characteristics of super-shear rupture (Bouchon *et al.*, 2001; Bouchon and Vallée, 2003; Dunham and Archuleta, 2004; Ellsworth *et al.*, 2004). Recent laboratory experiments (Rosakis *et al.*, 1999; Xia *et al.*, 2004) confirm and extend previous theoretical work on super-shear rupture propagation. Thus it seems plausible that super-shear rupture could have occurred during the 1906 San Francisco earthquake.

Reproduced with permission of the copyright owner. Further reproduction prohibited without permission.

4.2. Geodetic Analysis

The differences between existing source models are primarily north of Point Arena, where the San Andreas fault runs offshore, rendering direct observation of surface rupture impossible. 4.9 meters of slip was measured at Alder Creek, the northernmost observation of unambiguous faulting in the 1906 earthquake (Lawson, 1908). The same report found offset at Seal Cove, farther to the north, where the fault comes on shore again, but raised the possibility that this offset might have been due to landslides rather than tectonic faulting.

Only repeated triangulation observations were used to estimate slip in the previous geodetic study (Thatcher *et al.*, 1997), resulting in a weakly connected network especially north of Point Arena and hence large uncertainties in the inferred displacements. In this study we utilize all of the available triangulation measurements in the northern region, employing a projection method to remove the dependence on initial station positions (Yu and Segall, 1996). This allows us to strengthen this part of the network using non-repeated observations (Figure 4.3). It can be shown that the Yu and Segall (1996) method reduces to the standard approach, using only repeated angle measurements, when all of the measurements are repeated before and after the earthquake (Appendix I). Our data set in this region contains 60 pre-1906 and 172 post-1906 angle observations, respectively, compared with the 37 angle changes used in the previous study. We used the same data set, consisting of repeated angles, in the southern region.

The geodetic displacements along the entire rupture trace of the 1906 earthquake were estimated (Figure 4. 4 and 5, Table 4.1) using a model coordinate solution (Segall and

Reproduced with permission of the copyright owner. Further reproduction prohibited without permission.

Matthews, 1988) to constrain rigid body motions and scale changes. The result shows a displacement field characteristic of the co-seismic faulting as far north as Cape Mendocino (Figure 4.4. (a)). Two stations near the fault trace immediately south of Cape Mendocino show large displacements parallel to the changing local strike of the fault, which strongly supports fault slip as opposed to land-sliding in this area. As shown in Figure 4.6, we used a full length of singular values theoretically available in the inversion. Thus the displacement estimates can be considered stable physical solutions constrained by the data themselves, not from artifacts in the inversion. The magnitude of these displacement vectors indicates that the amount of fault slip that caused them is substantial.

We estimate the co-seismic slip distribution by a linear inversion of the triangulation data (Figure 4.7 and Table 4.2) using the surface trace from the new 3-D geologic model constructed by Jachens *et al.* (2006). A homogeneous elastic half-space was assumed in the forward calculation. An appropriate level of smoothing was determined by cross validation (Matthews and Segall, 1993) and used in the inversion (Figure 4.8). The idea behind cross validation is that a good model should predict data not used in the estimation. The appropriate smoothing is determined by testing what level of smoothing generates a model that best predicts the unused data. In our model slip varies only in the horizontal direction along the fault trace. Each value along the fault indicates averaged slip on a 10 km long and 12 km wide (deep) vertical fault patch. The fault is assumed to be extended vertically with 90° dip. We note that the average slip on each patch trades off with the assumed vertical extent of the fault (12 km in this study), with the result that, for example, models with greater depth extent but smaller averaged slip can fit the data equally well. But the integral of slip in the vertical direction should not change much irrespective of the assumed rupture width within a reasonable range of the seismogenic zone in California. Due to our inability to obtain the

Reproduced with permission of the copyright owner. Further reproduction prohibited without permission.

original data records, the slip distribution south of Point Arena is constrained only by the same repeated angle observations used in the previous study (Thatcher *et al.*, 1997). The slip north of Point Arena is significantly improved by the use of non-repeated angle measurements. Our slip on a ~500 km long rupture successfully fits the triangulation data, both confirming and refining the previous geodetic analysis (Thatcher *et al.*, 1997).

4.3. Seismic Analysis

With the mapped surface slip and geodetic data both consistent with the longer fault rupture, the short rupture length inferred from the seismic data stands out. For long strike slip events like the 1906 San Francisco earthquake, the duration of observed waveforms is related to the ratio of rupture length to rupture velocity; however, the duration of the observed teleseismic waves and the fixed 2.7 km/sec sub-Rayleigh rupture velocity assumed previously (Wald *et al.*, 1993), favors a shorter fault rupture. Our hypothesis is that by allowing more flexibility in the rupture velocity, including the potential for super-shear rupture, we might fit all data with a single model.

The 1906 earthquake was recorded by over 90 seismographic stations worldwide and both seismograms and background information are well preserved (Reid, 1910). One good example of the records is shown in Figure 4.10. However, the data quality reflects the fact that these were the early days of instrumental seismology. Most stations are not useful for waveform inversion. We used 5 stations, 8 components in total (Figure 4.9); two Wiechert Pendulum records from Europe (Uppsala, Sweden and Gottingen, Germany), two Omori records from Japan (Kobe and Osaka), and one Bosch-Omori record from the Caribbean (Puerto Rico). Two

Reproduced with permission of the copyright owner. Further reproduction prohibited without permission.

Omori stations in Japan have only one component. Those 5 stations were selected based on the proximity of observed Green's functions to the 1906 records and the need for spatial/azimuthal coverage. Detailed information on the seismic data is well documented by the previous study (Wald *et al.*, 1993).

We apply a Bayesian inversion approach coupled with a Monte Carlo sampling method (the Metropolis algorithm) (Mosegaard and Tarantola, 2002; Metropolis *et al.*, 1953). The posterior distribution of the model (slip and rupture velocity) is proportional to the product of a prior distribution and a likelihood function. The likelihood function contains only the seismic data and the geodetic inversion results obtained above were used in the prior distribution in order to stabilize the slip in the inversion, which we believe was relatively well resolved in the linear geodetic inversion. The prior for the rupture velocity is a Gaussian distribution centered at the previously used sub-Rayleigh velocity (2.7 km/sec) with a 0.5 km/sec standard deviation. By assuming sub-shear rupture velocity in the prior, we ensure that the method will only find super-shear rupture if the data require it.

We use waveforms from the 1984 M 6.2 Morgan Hill earthquake as empirical Green's functions to calculate teleseismic waveforms (Wald *et al.*, 1993). Both the Morgan Hill and the 1906 San Francisco earthquake are vertical strike-slip events and share approximately the same strike (~ N35°W), in particular, in the central portion of the 1906 rupture. But the San Andreas fault bends in the northern and southern portion of the study area as shown in Figure 2. The average strike of these segments is about 10 ~ 15° different from that of the Morgan Hill earthquake, such that modest error is introduced by using the same Green's function for the entire fault trace. The Green's function is time-lagged with elapsed rupture time along the fault trace from the hypocenter and a linear summation of the time-lagged Green's function

Reproduced with permission of the copyright owner. Further reproduction prohibited without permission.

weighted by slip provides synthetic waveforms for the 1906 earthquake. We did not explicitly consider the detailed shape of temporal evolution of slip and rise time in the inversion because that is well beyond the resolving power of the data.

As discussed in detail by Wald *et al.* (1993), the age and quality of the seismic data limit the resolution of source characteristics for the 1906 earthquake. The uncertain instrument response, limited accuracy of the available Green's functions, particularly when applied to the northernmost end of the fault, and complex wave propagation effects for the SV component, all contribute to the data residuals. A waveform inversion without the analysis of very long period data (>40 sec) may underestimate the rupture area of large earthquakes as observed in the Sumatra earthquake (Stein and Okal, 2005). Despite the limited data coverage quality, forward modeling indicates that the duration and amplitude of the teleseismic waves can constrain the overall duration of the rupture, and hence the average rupture velocity when combined with the fault length determined from the geodetic data.

4.4. Super-shear Rupture and Combined Slip Model

Sensitivity tests indicate that, because of the geometry of the problem, rupture north of the hypocenter is primarily constrained by the two European seismograms (Gottingen and Uppsala) while rupture to the south is primarily constrained by the Puerto Rico data. Thus, we first tried a two-segment rupture velocity model split at the hypocenter and solved for a single rupture velocity on each of these two segments. Several locations have been suggested for the hypocenter of the earthquake by analyzing local and teleseismic observations (Reid, 1910; Bolt, 1968; Lomax, 2005). We used the latest estimate determined by A. Lomax (2005), which

Reproduced with permission of the copyright owner. Further reproduction prohibited without permission.

is located about 3 km west of the San Francisco zoo. We find that it takes about 85 and 52 seconds, respectively, for the rupture to propagate along the northern (330 km long) and southern (150 km) segment from the hypocenter, which indicates that the rupture travels to the north at an average speed of 3.9 +/- 0.1 km/sec, exceeding the average shear wave velocity of the Earth's crust north of San Francisco, and to the south at 2.9 +/- 0.1 km/sec, respectively. The standard errors of the rupture velocity estimates are quite small, due to the fact that neighboring points in seismic waveforms are highly correlated, a fact not accounted for in the inversion. In an attempt to localize the rupture velocity, we divided the rupture into five segments (3 segments north of the hypocenter, 110 km for each; 2 segments to the south, 70 and 80 km for each). While it is possible that the data could resolve such spatial variations in rupture velocity, the fact that the total rupture durations north and south of the hypocenter are about the same in both the two and five segment models (Figure 4.11) suggests that while super-shear rupture to the north of the hypocenter is required to fit the data, it may be difficult to localize it further.

Figures 4.12 and 4.13 show the slip and waveform comparisons, respectively, obtained from the two segment model. A digitized version of the slip estimates are given in Table 4.2. The slip in the northern segment is smoother than that obtained solely from geodetic data (Figure 4.7), but there is significant slip in the northern region of the fault. This confirms that the long rupture length (~500 km) is compatible with the seismic data, although the amount of slip is somewhat smaller than the geodetically preferred value. The synthesized waveform envelopes capture the duration and amplitude of the seismograms and reasonable waveform fits are achieved at the European stations even though the objective function is defined using the waveform envelopes (Figure 4.13). The polarity of the synthetic waveform (SV component) at the PTR station is reversed. This can occur while fitting the waveform envelope because it

Reproduced with permission of the copyright owner. Further reproduction prohibited without permission.

does not preserve polarity information. Inaccurate arrival time alignment, an inaccurate Green's function, reversed polarity on the instrument, and delayed rupture propagation to the southeast are all possible explanations of this mismatch. Because the fit at PTR is primarily controlled by the slip and rupture propagation to the southeast of the hypocenter, it does not affect the inference that the rupture extended a total length of 500 km nor that rupture to the north of the hypocenter was super-shear.

Our final slip model has an average slip of 4.3 meters and a seismic moment of 7.9×10^{20} N-m, which corresponds to a moment magnitude of Mw 7.9. Although the final slip model was obtained by a joint inversion of the geodetic and seismic data, the final static slip distribution is primarily constrained by the triangulation data. Because the triangulation survey data used in this study span an interval as long as 40 years, our slip estimates include postseismic and interseismic, as well as coseismic deformation. Because the long-term aseismic strain accumulates in the opposite direction of the deformation caused by earthquakes, i.e. right-lateral strain accumulation between earthquakes vs. right-lateral strain release during the earthquake, our estimate of Mw 7.9 should be considered a lower bound on the size of the 1906 earthquake in that sense. However afterslip at seismogenic depths, which is very difficult to constrain given the data available, could bias the estimated magnitude to higher values.

4.5. Discussion and Implications

The long rupture length is also strongly supported by seismic intensity data from the 1906 earthquake as shown in Figure 4.14 (Boatwright and Bundock, 2005). The intensity map clearly shows the severely damaged area (intensity VII or larger) extending north to the

Reproduced with permission of the copyright owner. Further reproduction prohibited without permission.

Mendocino triple junction and rules out the possibility that the slip on the fault north of Point Arena occurred aseismically. Moreover, a recent examination of the northernmost San Andreas fault near Shelter Cove concluded that slip mapped there in 1906 was likely tectonic, extensive, and located on the main trace of the San Andreas fault (Prentice *et al.*, 1999).

A simpler analysis of the waveform data that does not directly model the spatial variation of slip also supports super-shear rupture north of the hypocenter (Figure 4.15). Deconvolution of the empirical Green's functions from the 1906 seismograms yields an estimate of the apparent source duration and, given the fault length, the average rupture velocity. Using the European stations and employing positivity, smoothness, and moment-minimization constraints in a time domain deconvolution of the empirical Green's function event from the 1906 mainshock, we find a duration of ~ 75 seconds, which corresponds to an average rupture velocity of ~3.4 km/sec north of the hypocenter. This should be regarded as a lower bound since the smoothness constraint on the source time function deconvolution results in a longer duration, and hence lower inferred rupture velocity.

Both the intensity data and the deconvolution support our long rupture length slip model with super-shear rupture. If the rupture velocity in this earthquake were super-shear, as we have suggested, then it has important implications for seismic hazard. First it demonstrates that slip models derived from geodetic and seismic observations are compatible, which is relevant for northern California because it provides a unified slip model to be used in recurrence models for future earthquakes. More generally, because the nature of strong ground motion for earthquakes that undergo super-shear rupture is profoundly different from those where the rupture is sub-shear (Aagaard and Heaton, 2004), it will be necessary to account for this when

Reproduced with permission of the copyright owner. Further reproduction prohibited without permission.

predicting both the level and the variability of strong ground motion in future large strike-slip earthquakes.

Acknowledgments. We thank David Wald for providing us with his digitized teleseismic data and Wayne Thatcher for sharing his notes on the triangulation data. We also thank the National Geodetic Survey for helping us extract triangulation data from their archives. We greatly benefited from the advice, criticism, and assistance of David Wald, Jack Boatwright, and Brad Aagaard throughout the study and thank two reviewers, David Wald and Pengcheng Liu, for their insightful comments, which improved the manuscript. This research was supported by the U.S. Geological Survey (USGS), Department of Interior, under USGS award number 06HQGR0025. The views and conclusions contained in this document are those of the authors and should not be interpreted as necessarily representing the official policies, either expressed or implied, of the U. S. Government.

Reproduced with permission of the copyright owner. Further reproduction prohibited without permission.

Table 4.1. Estimated (model coordinate) displacement fields in meter from triangulation data with predicted ones from the geodetic slip model

Latitude (N)	Longitude (W)	Predicted disp. (E)	Predicted disp. (N)	Estimated disp. (E)	Estimated disp. (N)
40.4975	124.2947	-0.0725	-0.3474	1.0229	-0.6778
40.3339	123.5545	-0.0299	-0.2331	-0.8785	-0.5907
40.1568	124.1243	0.6708	-0.9777	0.4780	-1.0715
40.0140	124.0045	0.2794	-1.8202	-0.2958	-2.3543
39.6865	123.5795	0.2114	-0.4999	-0.4852	-0.6305
39.5159	123.0962	0.1044	-0.2336	0.1828	0.3065
39.3769	122.7587	0.0817	-0.1767	0.9721	-0.0794
39.3617	123.4461	0.2064	-0.4649	0.1353	-0.2383
39.3411	123.7207	0.4331	-0.8950	0.4117	-0.6125
39.1355	123.3128	0.2229	-0.4127	0.6054	-0.0751
39.0662	123.5874	0.4641	-1.0393	1.0637	-0.7565
39.0222	123.5232	0.5639	-0.8466	0.9283	-0.8087
39.0111	123.6446	1.0557	-1.7062	1.2884	-1.2452
39.0096	123.6932	1.3658	-2.5333	1.0983	-1.9538
38.9938	123.6316	1.1332	-1.6839	1.3244	-1.3728
38.9879	123.6706	1.4835	-2.1606	1.6264	-1.9706
38.9662	123.6827	-1.1208	1.7465	-1.7292	0.8487
38.9552	123.7400	-0.7289	1.2423	-0.8116	1.2262
38.9219	123.7269	-0.6825	1.1356	-0.7415	1.0239
38.9125	123.6934	-0.7906	1.2841	-0.7915	1.2924
38.9110	123.7053	-0.7320	1.2018	-0.7271	1.1973
38.9011	123.6981	-0.7214	1.1836	-0.7136	0.9647
38.6693	122.6335	0.1675	-0.3021	0.6527	-0.0174
38.6078	123.3693	-1.1823	0.9315	-1.1146	1.0087
38.5764	123.3020	-1.3732	1.4765	-1.3239	1.5153
38.5667	123.3327	-1.1874	1.1729	-1.2685	1.1507
38.5466	123.2410	1.0857	-1.6759	0.8408	-1.3975
38.5332	123.2765	-1.3793	1.4247	-1.5068	1.2408
38.5128	123.2535	-1.4618	1.4885	-1.5984	1.5603
38.5085	123.1985	1.0762	-1.9281	0.9160	-1.5840
38.5053	123.1200	0.7751	-1.7320	0.8454	-1.1162
38.5008	123.2341	-1.5584	1.5530	-1.1689	1.6747
38.4316	123.1179	1.3238	-2.8148	1.6587	-2.1002
38.3235	122.5744	0.3772	-0.4189	1.0499	-1.1421
38.3081	123.0626	-1.1734	2.2122	-1.4496	2.8624
38.3066	123.0010	1.4137	-2.0005	1.2892	-1.9271
38.2476	122.9358	1.4924	-2.0333	1.3020	-2.4510
38.2127	122.9707	-1.8644	2.1571	-1.8215	1.5488
38.1821	122.9463	-1.9068	2.2089	-1.9916	1.8872
38.1820	122.9017	1.8662	-2.5440	0.8010	-3.1824
38.1371	122.9065	-1.8548	2.4265	-2.6622	2.4845
38.1329	122.8672	2.0200	-2.6411	1.9482	-3.5059
38.0801	122.8669	-1.6236	2.3450	-1.6509	1.5519
37.9958	123.0222	-0.4610	0.8138	-0.5734	0.8719
37.9243	122.5959	1.0456	-1.1379	1.0856	-1.3246

Reproduced with permission of the copyright owner. Further reproduction prohibited without permission.

Table 4.1. (Continued)

Latitude (N)	Longitude (W)	Predicted disp. (E)	Predicted disp. (N)	Estimated disp. (E)	Estimated disp. (N)
37.8826	122.2418	0.3681	-0.3557	0.5164	-0.5773
37.8821	121.9134	0.2137	-0.1719	-0.1820	-0.9223
37.8160	122.5288	0.9325	-1.2259	0.8425	-1.2557
37.7484	122.4665	0.8610	-1.0940	0.9408	-1.0301
37.7195	122.5035	0.9770	-1.3840	1.0988	-1.2884
37.6995	123.0010	-0.1323	0.4229	-0.4406	0.2670
37.6878	122.4348	0.7871	-1.1553	1.1511	-1.1161
37.6327	122.4746	-0.5409	1.3172	-0.8709	0.9610
37.6144	122.4598	-0.5429	1.2965	-0.7765	0.7895
37.6140	122.4947	-0.4650	1.1527	-0.9203	0.6503
37.5956	122.5229	-0.3871	0.9747	-0.6041	1.4115
37.5732	122.2621	0.6089	-0.7509	0.4927	-0.5559
37.5618	122.4769	-0.4745	0.9809	0.2861	1.7407
37.5513	122.0947	0.4007	-0.4434	0.6404	-0.1435
37.4802	122.2544	0.7951	-1.0468	0.9127	-1.0247
37.4777	121.5552	0.2074	-0.0867	-0.2657	-0.3667
37.4767	122.1356	0.5482	-0.6372	0.6397	-0.6523
37.4106	122.3078	-0.6842	0.9667	-0.6743	0.7911
37.3194	122.1471	1.0952	-1.2563	1.2955	-1.4097
37.1114	121.8435	0.9819	-0.5563	1.0182	-0.4017
36.9784	122.0552	-0.1793	0.3503	-0.5763	0.6391
36.9524	122.0260	-0.1645	0.3319	-0.1630	0.3337
36.9054	121.2327	0.1948	-0.0069	0.1983	0.5413
36.7559	121.5199	0.0066	0.2497	0.1509	-0.0512
36.6332	121.9255	0.0053	0.1648	0.2432	0.4134
36.5263	121.6090	0.0151	0.1240	0.5806	0.6782

Reproduced with permission of the copyright owner. Further reproduction prohibited without permission.

Table 4.2. Slip models from inversion of geodetic data only and combined inversion of the geodetic and seismic data

Latitude (N)	Longitude (W)	Geodetic slip (m)	1 sigma (m)	Combined slip (m)	1 sigma (m)
40.2730	124.3966	5.5048	1.1259	5.9488	0.6627
40.2125	124.3096	5.5469	1.0789	5.2461	0.7254
40.1543	124.2201	4.6582	0.9762	3.4777	0.9477
40.0846	124.1469	4.4663	0.9905	3.3096	0.7966
40.0123	124.0771	8.4355	0.9718	5.5837	1.1535
39.9322	124.0248	9.2715	0.9634	6.5132	1.0257
39.8443	124.0005	8.3581	0.9060	6.3355	0.8098
39.7550	123.9857	7.2505	0.8642	5.8493	0.7475
39.6659	123.9702	6.1543	0.8596	5.8416	0.7214
39.5769	123.9545	5.0232	0.8839	6.1799	0.6666
39.4886	123.9328	3.8733	0.8872	6.5109	1.2041
39.4008	123.9068	2.9302	0.8015	5.7567	1.1582
39.3174	123.8634	2.1978	0.6866	5.0934	1.1479
39.2298	123.8369	2.0909	0.6062	4.0424	0.6566
39.1456	123.7962	3.0856	0.4692	4.0167	0.6227
39.0655	123.7433	5.6843	0.0846	5.6925	0.0863
38.9868	123.6871	4.8330	0.0978	4.8199	0.1012
38.9119	123.6231	4.4670	0.4132	3.8181	0.4549
38.8405	123.5528	3.1380	0.4920	1.9279	0.6903
38.7668	123.4868	2.4013	0.5247	1.1627	0.7113
38.6956	123.4163	2.7229	0.5147	1.7309	0.6554
38.6254	123.3443	4.1614	0.1670	4.1459	0.1736
38.5546	123.2734	4.2642	0.0670	4.2693	0.0682
38.4842	123.2019	5.9573	0.2577	6.1564	0.2599
38.4125	123.1331	9.3333	0.3820	9.6600	0.4373
38.3389	123.0671	4.3777	0.1950	4.4989	0.1824
38.2643	123.0032	6.1433	0.0849	6.1569	0.0873
38.1947	122.9310	6.9541	0.0920	6.9483	0.0941
38.1231	122.8623	7.4083	0.2777	7.2586	0.2649
38.0509	122.7941	5.7766	0.3043	5.5592	0.3456
37.9764	122.7304	4.2121	0.4234	4.0618	0.4125
37.9062	122.6594	3.9169	0.3972	4.0345	0.4020
37.8318	122.5952	4.2240	0.4244	4.3851	0.3855
37.7556	122.5345	3.4892	0.3935	3.7255	0.4093
37.6786	122.4765	3.1962	0.3009	3.0154	0.3339
37.5983	122.4258	3.1737	0.4505	2.8933	0.4946
37.5233	122.3629	2.9955	0.3653	3.3051	0.3448
37.4510	122.2954	3.3602	0.3191	3.6820	0.3089
37.3788	122.2280	3.1323	0.4428	3.5137	0.5651
37.3083	122.1577	3.4946	0.5126	2.6810	0.5709

Reproduced with permission of the copyright owner. Further reproduction prohibited without permission.

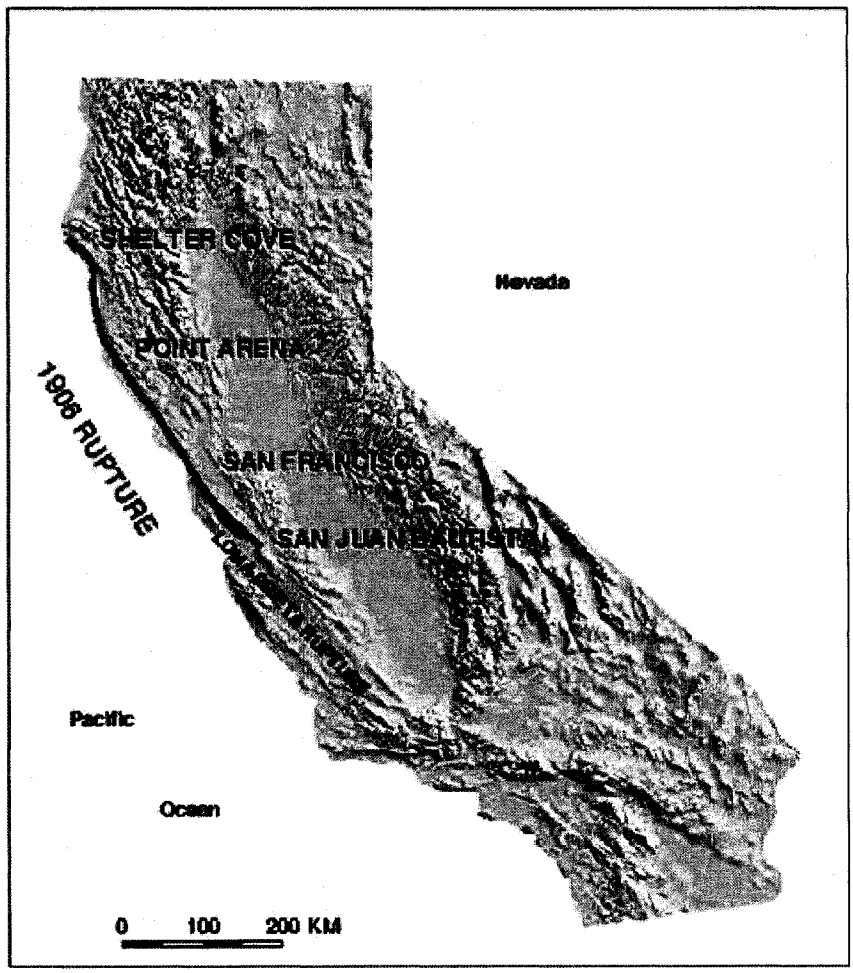

Figure 4.1. 1906 San Francisco earthquake. The red line shows an approximate rupture trace (~ 500 km) of the event. The epicenter is located near San Francisco as shown with the star in the figure (Lomax, 2005) and the 1989 Loma Prieta earthquake rupture segment is also shown for comparison.

Reproduced with permission of the copyright owner. Further reproduction prohibited without permission.

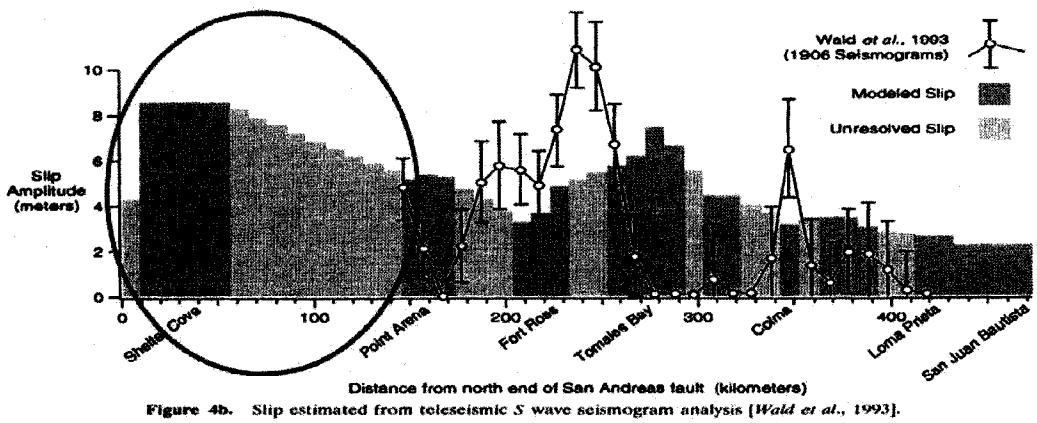

Figure 4b. Slip estimated from teleseismic *S* wave seismogram analysis [*Wald et al.*, 1993].

Figure 4.2. Comparison of two previous slip models for the 1906 event as shown in Thatcher et al. (1997). Shaded bars and solid line with circles show the geodetic (Thatcher et al., 1997) and seismic slip model (Wald et al., 1993), respectively. A clear difference between these two models is observed in the northern region as emphasized by a red circle. No slip variation in the vertical direction, slip varies only in the along-strike direction in these models.

Reproduced with permission of the copyright owner. Further reproduction prohibited without permission.

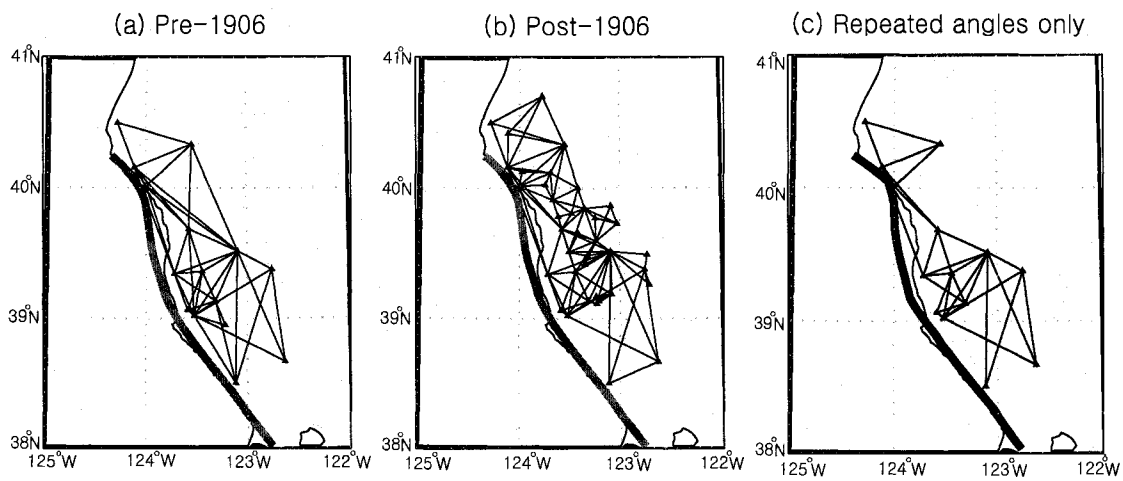

Figure 4.3. Triangulation network in the northern region of the San Andreas fault used in the inversion before (a) and after (b) the 1906 San Francisco earthquake compared with network (c) of repeated angles only (Thatcher *et al.*, 1997). The fault trace used in the study (Jachens *et al.*, 2006) is shown as a thick solid line in (a) and (b). The solid line in (c) shows a fault trace used in the previous study. The time spans of the triangulation surveys before and after the earthquake are 1878-1892 and 1925-1942, respectively. An average standard deviation in angle measurement errors is less than 1 arc-sec for the post 1906 data set and about two arc-seconds for the pre 1906 data.

Reproduced with permission of the copyright owner. Further reproduction prohibited without permission.

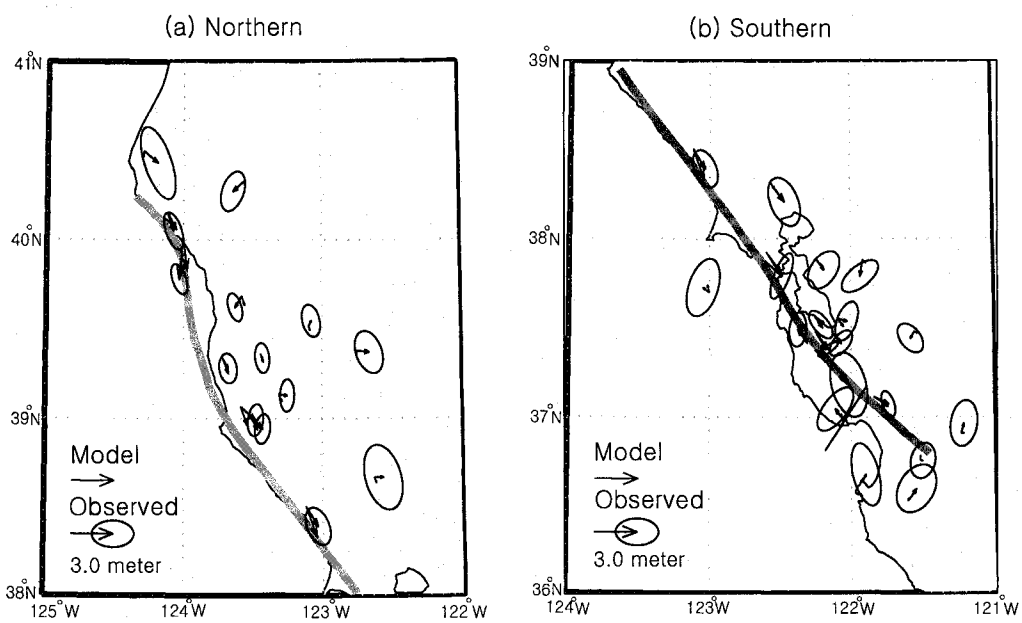

Figure 4.4. Estimated model coordinate displacement fields (blue arrows) with 95 % confidence ellipses in the northern (a) and southern (b) region of the 1906 rupture area. Predicted displacements from the estimated geodetic slip model and the San Andreas fault trace (Jachens *et al.*, 2006) in the region are shown as red arrows and thick solid line, respectively. Stations near the fault in the northern region (a) show large displacements parallel to the local fault strike.

Reproduced with permission of the copyright owner. Further reproduction prohibited without permission.

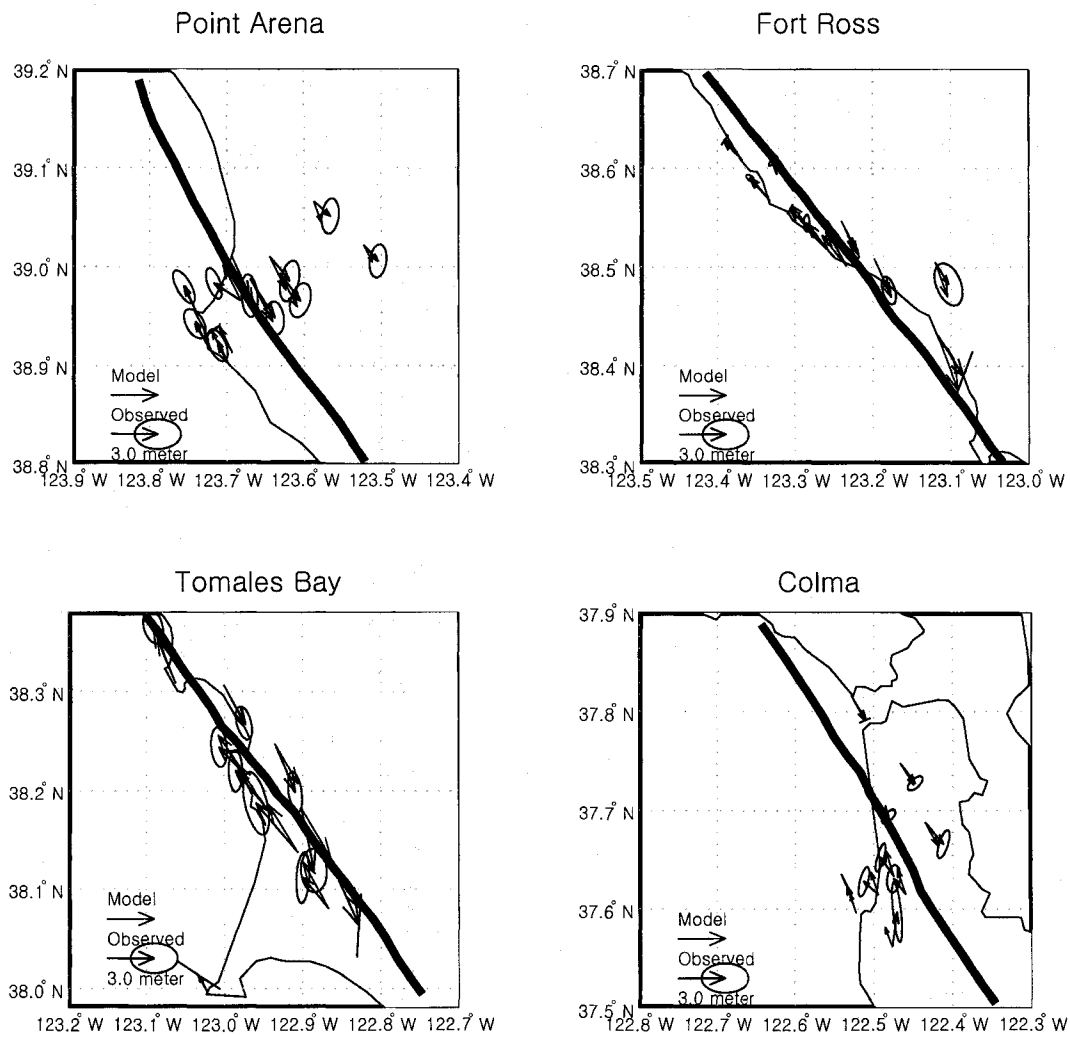

Figure 4.5. As for Figure 2, the estimated model coordinate displacement fields (blue arrows) with 95 % confidence ellipses in four local networks; (a) Point Arena, (b) Fort Ross, (c) Tomales Bay, (d) Colma.

Reproduced with permission of the copyright owner. Further reproduction prohibited without permission.

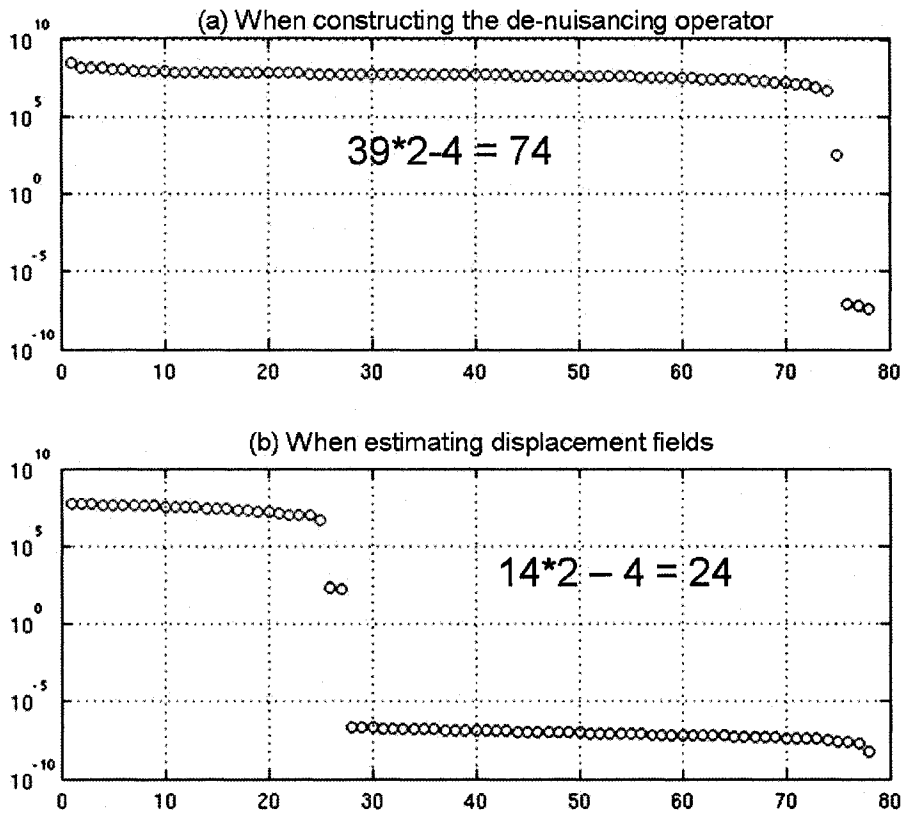

Figure 4.6. Singular values used in the inversion as marked with red circles. (a) The number of singular values used when constructing the de-nuisancing operator, (b) The number of singular values used when estimating the displacement fields (Figure 4.4. (a)). We used 39 stations in total in the northern region and 14 of them have repeated observations before and after the 1906 rupture, which means the coseismic displacement estimates can be obtained possible. Since a full length of singular values available except four intrinsic null vectors (i.e., translations in x and y, rotation, and expansion) are used in the inversion, the displacement estimates can be considered stable physical solutions. Note that the actual inversion is performed for the entire network including both the northern and southern network, but this singular value analysis is done only with the northern network (Figure 4.3. (a)) in order to analyze the reliability of the displacement estimates in the northern region independently.

Reproduced with permission of the copyright owner. Further reproduction prohibited without permission.

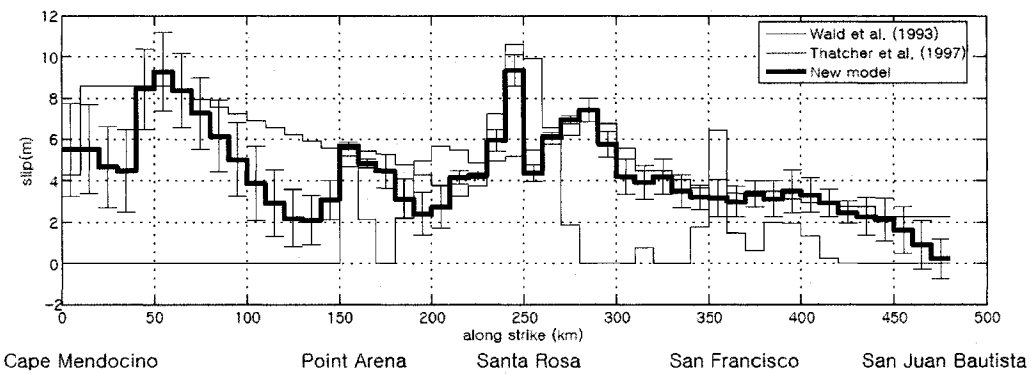

Figure 4.7. Slip model obtained from inversion of geodetic data only with 2 sigma errors. The two previous slip models are also given for comparison (Thatcher *et al.*, 1997; Wald *et al.*, 1993). Slip varies only in the horizontal direction and each value along the fault indicates averaged slip on each 10 km (length) by 12 km (width) fault patch. Slip in the northern region is primarily constrained by two nearby stations, resulting in relatively large errors in this region. The larger errors notwithstanding, these results strongly support large slip in this region. Slip distribution in the southern region is very similar to the previously obtained geodetic model because we used the same data set in that region. We did, however, find large slip between Fort Ross and Tomales Bay, although it was smoothed in the previous geodetic model (Thatcher *et al.*, 1997).

Reproduced with permission of the copyright owner. Further reproduction prohibited without permission.

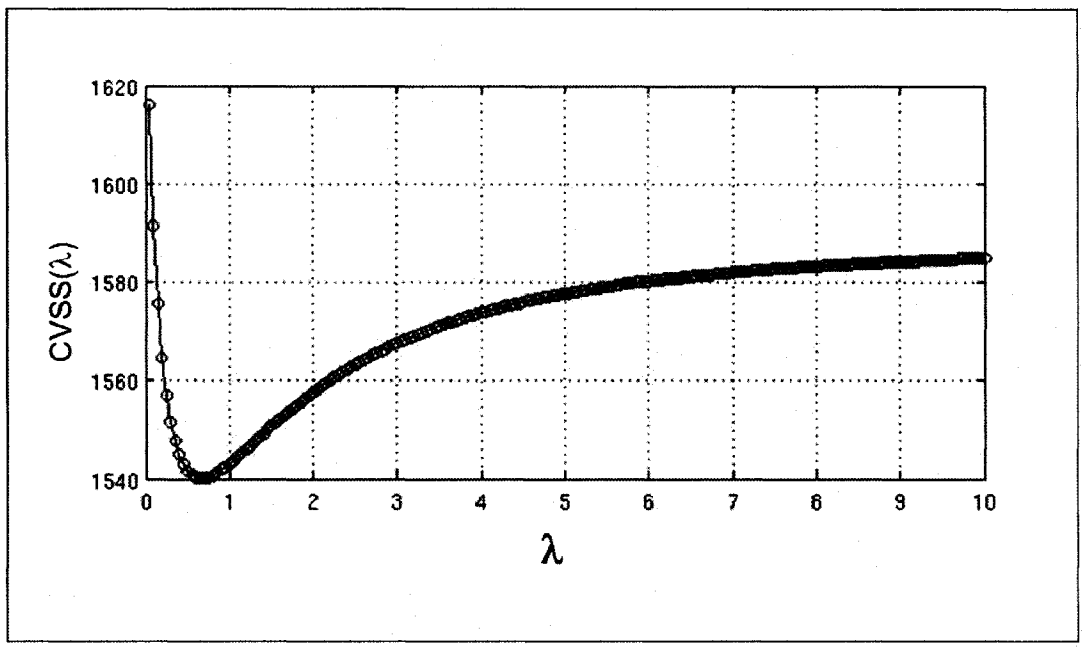

Figure 4.8. Cross validation curve used in the geodetic slip inversion. The CVSS(λ) curve indicates how well each estimated model predicts unused data as a function of λ, The smaller, the better. The appropriate smoothing level (λ) in the inversion can be determined based on the cross validation curve, i.e., λ with a minimum of the CVSS.

Reproduced with permission of the copyright owner. Further reproduction prohibited without permission.

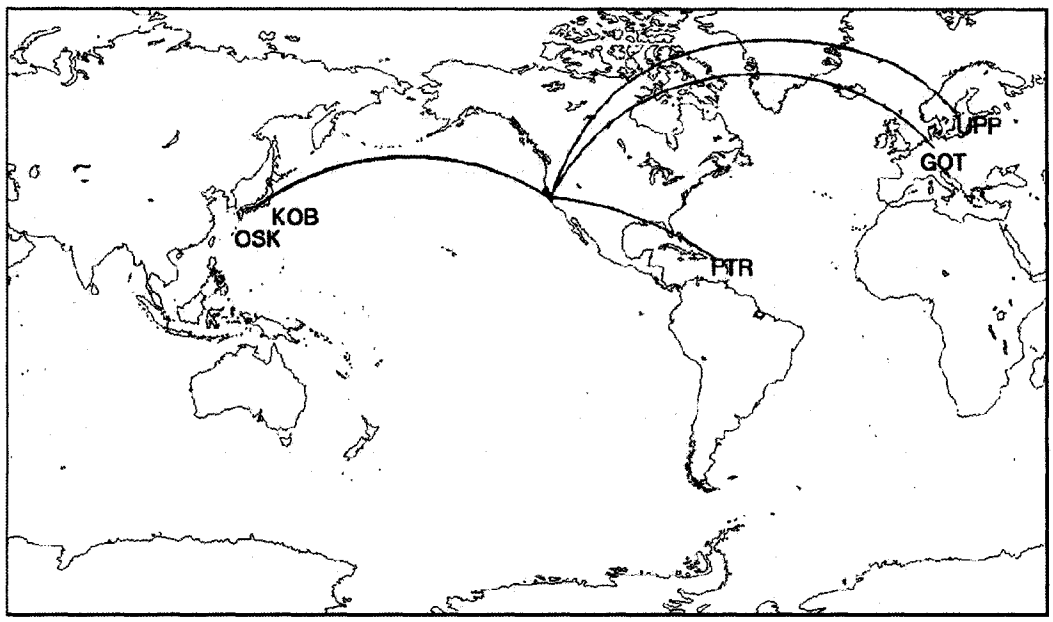

Figure 4.9. Five seismic stations used in the study. Two Wiechert Pendulum records from Europe (Uppsala, Sweden and Gottingen, Germany), two Omori records from Japan (Kobe and Osaka), and one Bosch-Omori record from the Caribbean (Puerto Rico). Two Omori stations in Japan have only one component.

Reproduced with permission of the copyright owner. Further reproduction prohibited without permission.

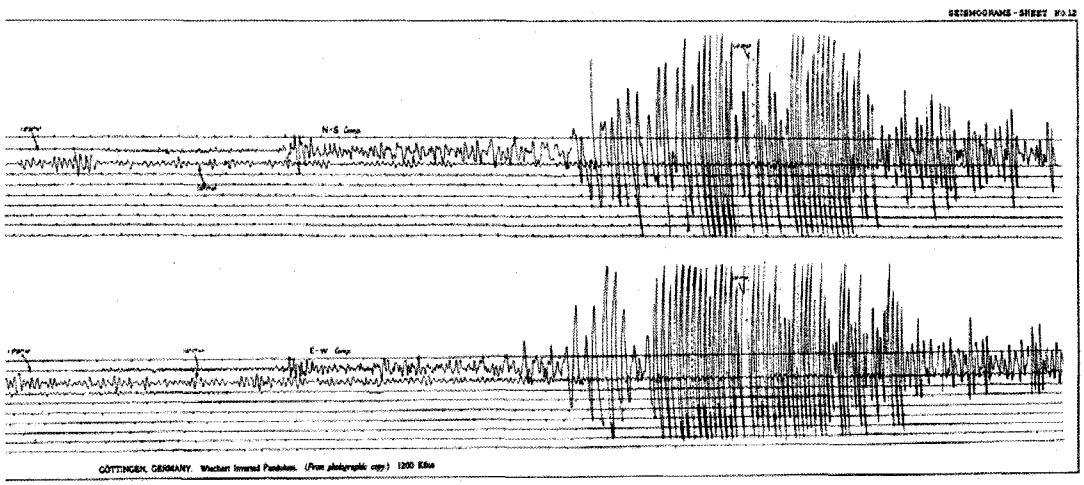

Figure 4.10. Waveforms recorded by the Wiechert Inverted Pendulum seismograph in Gottingen, Germany in the 1906 earthquake.

Reproduced with permission of the copyright owner. Further reproduction prohibited without permission.

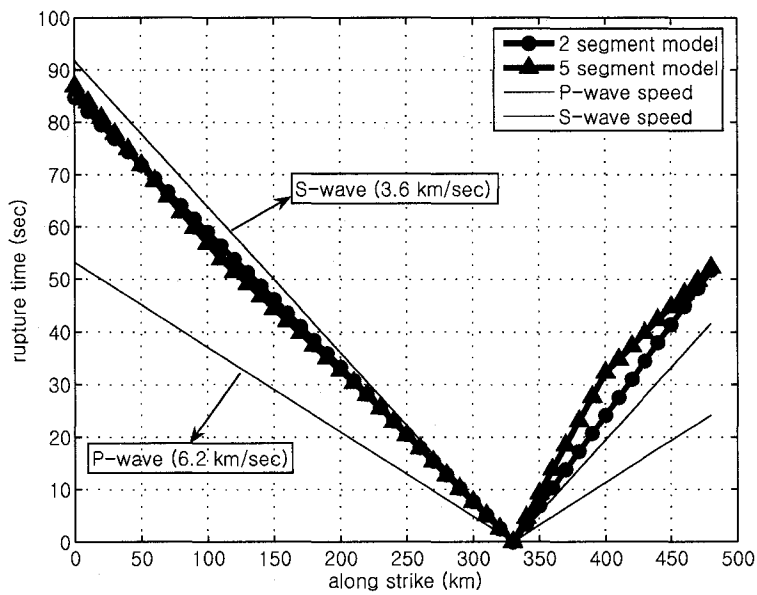

Figure 4.11. Rupture time distribution along the fault with two segment (a) and five segment model (b). *P*- and *S*-wave propagation times are also provided from the average *P*- and *S*-wave speed along the San Andreas fault. Despite variations in the five segment model, the total rupture durations north and south of the hypocenter are about the same for the two and five segment model, about 85 seconds for the 330 km northern segment and about 52 seconds for the 150 km southern segment, respectively.

Reproduced with permission of the copyright owner. Further reproduction prohibited without permission.

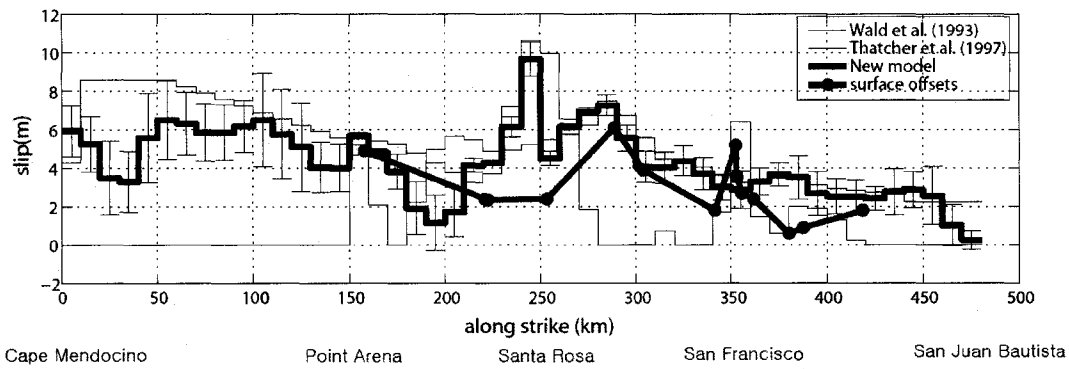

Figure 4.12. Final slip models with 2 sigma errors obtained from both geodetic and seismic data compared with two previous slip models. Surface offsets south of Point Arena are also shown in the plot. Significant slip is observed in the northern region of the fault although the actual amount of slip is somewhat smaller than the previous geodetic slip (Thatcher *et al.*, 1997). The rest is the same as Figure 4.

Reproduced with permission of the copyright owner. Further reproduction prohibited without permission.

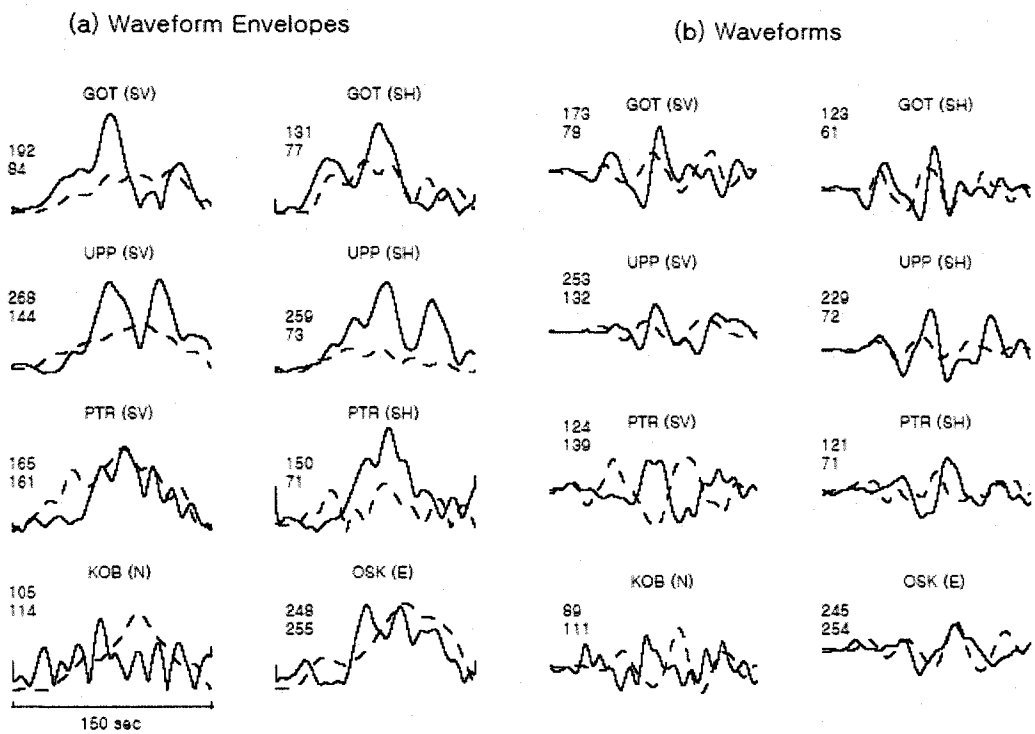

Figure 4.13. Comparison of observed (solid) and calculated (dashed) waveforms and their envelopes. Data are direct S-phases band-pass filtered between 0.01 and 0.1 Hz. Maximum amplitudes are given on the left of each trace in mm at the WWSSN LP seismograph (top: observed, bottom: calculated). The calculated waveform envelopes successfully reproduce most of the amplitude and duration information of the observed waveform envelopes. Some stations also achieve good waveform fitting although our objective function is based on the waveform envelopes (GOT: Gottingen, Germany, UPP: Uppsala, Sweden, PTR: Puerto Rico, W.I., KOB: Kobe, Japan, OSK: Osaka, Japan).

Reproduced with permission of the copyright owner. Further reproduction prohibited without permission.

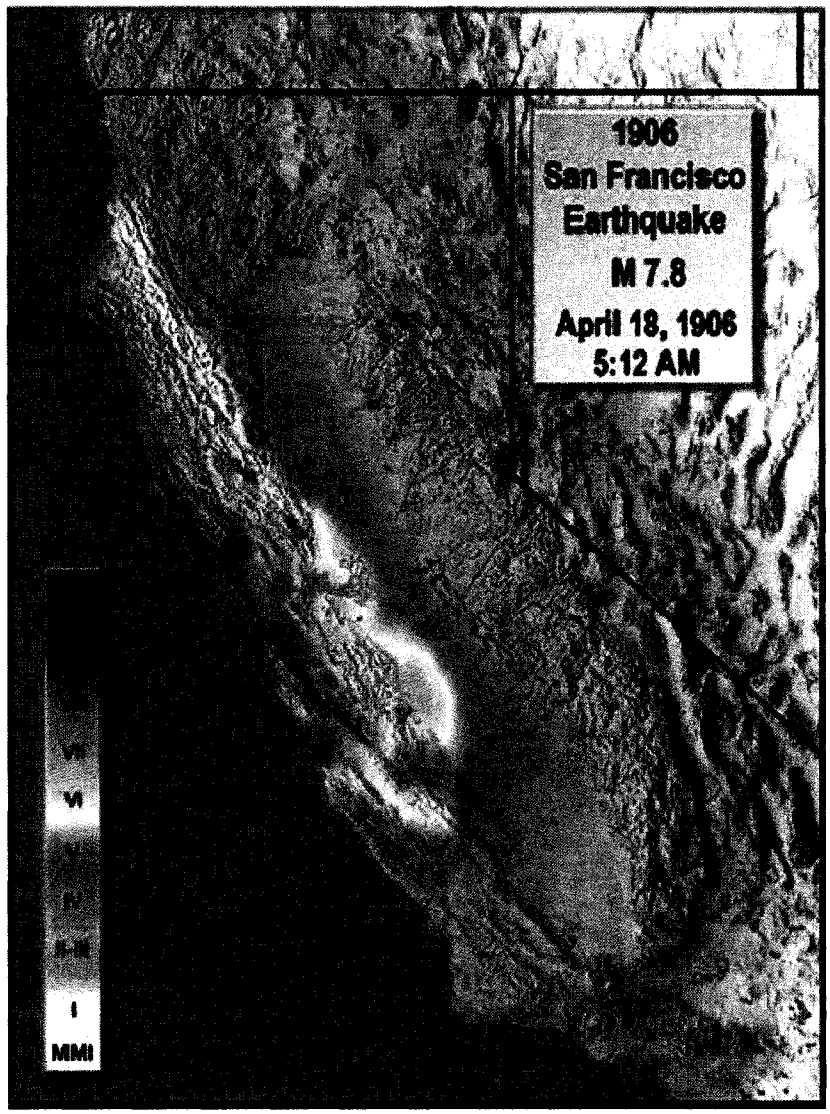

Figure 4.14. Intensity map for the 1906 San Francisco earthquake by Boatwright and Bundock (2005)

Reproduced with permission of the copyright owner. Further reproduction prohibited without permission.

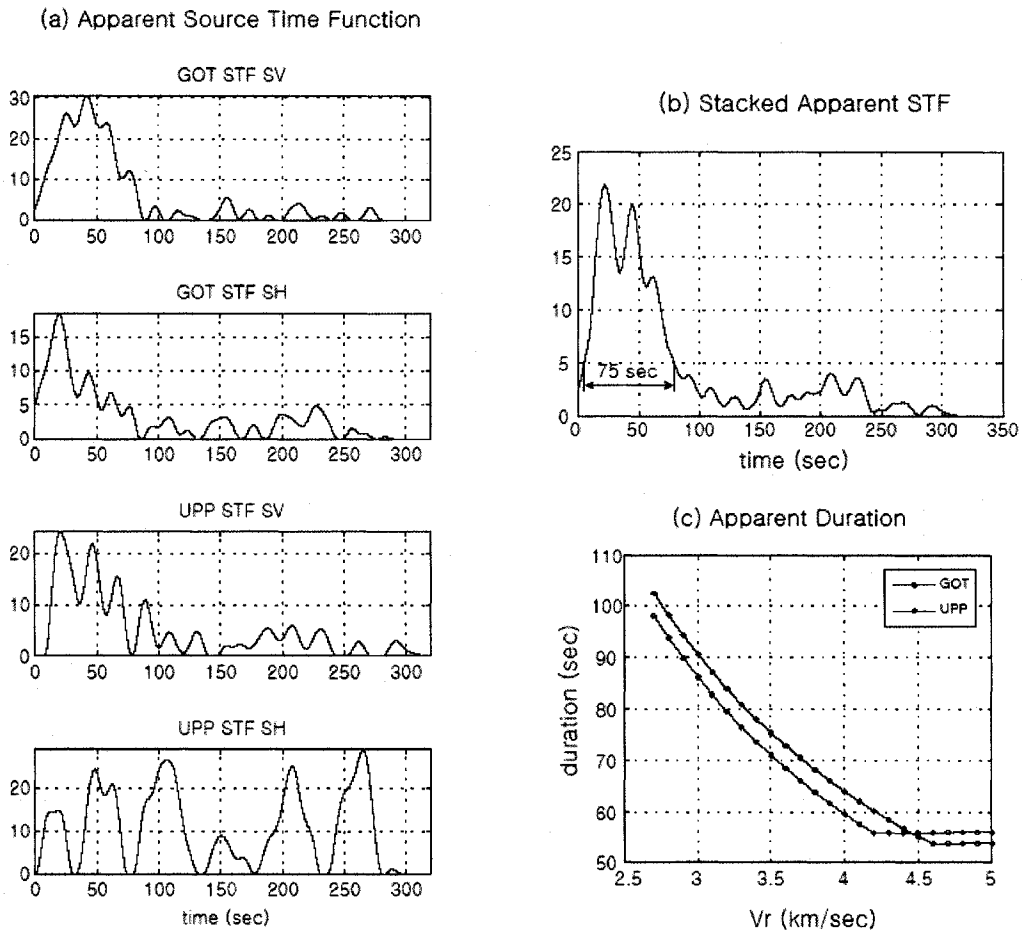

Figure 4.15. Total rupture duration of the earthquake inferred from the deconvolution of observed waveforms. (a) Apparent source time functions for two European stations (GOT and UPP), obtained from deconvolving the empirical Green's functions of the Morgan Hill earthquake from the observed waveforms. (b) Stacked version of the all source time functions except the SH component of the Uppsala station. (c) Expected duration of waveforms at each station as a function of the rupture velocity north of the hypocenter. The rupture velocity south of the hypocenter was fixed as 2.9 km/sec. The expected duration of waveforms were calculated from the maximum difference of arrival times from each fault patch. The duration of the apparent source time functions are well defined at each component except for the Uppsala SH, and is quite well resolved in the stacked source time function (b). The apparent rupture duration at the two European stations is about 75 seconds which is equivalent to a 3.4 km/sec average rupture velocity north of the hypocenter. This independent measure of the total rupture duration of the earthquake supports the high rupture velocity, although the estimated velocity is somewhat less than in the kinematic slip inversion.

Reproduced with permission of the copyright owner. Further reproduction prohibited without permission.

Chapter 5. Pseudo-Dynamic Modeling of Large Strike-Slip Earthquakes

Abstract

Accurate prediction of the intensity and variability of near-field strong ground motion for future large earthquakes strongly depends on our ability to simulate realistic earthquake source models for those events. Guatteri et al. (2004) developed a pseudo-dynamic source modeling method to generate physically self-consistent finite source models without high-cost full dynamic rupture simulation, but still retaining important characteristics of dynamic faulting. We improve their method and extend its magnitude coverage to develop efficient finite-source characterization for ground motion predictions to larger strike-slip events (M > 7.2). For this we constructed 15 spontaneous dynamic rupture models with different slip realizations and hypocenter locations for large, Mw 7.5, strike-slip earthquakes. These earthquakes have a very long and narrow rupture dimension (150 km long and 15 km wide), which leads to behavior that is substantially different from the smaller events used by Guatteri et al. (2004). A set of empirical relationships, derived from the analysis of these spontaneous rupture models outputs, exhibit interesting features that were not observed in the previous study. We also allow greater latitude for supershear rupture in the present study, because it has been observed recently for a number of long strike-slip earthquakes (Bouchon et al., 2001; Bouchon and Vallèe, 2003; Dunham and Archuleta, 2004; Song et al., 2008). We find that the relatively fixed fault width of these long, narrow ruptures plays a critical role in controlling rupture behavior even if the rupture dimension increases in the along-strike direction as predicted by Day (1982a). Our

Reproduced with permission of the copyright owner. Further reproduction prohibited without permission.

improved pseudo-dynamic modeling method can be used to generate realistic finite-source earthquake models for large strike-slip events to simulate strong ground motion in the near-field of large events.

5.1. Introduction

Recent kinematic source inversion studies show that earthquake rupture is a complex process (Mai and Beroza, 2002). Not only final slip distribution, but all other elements of the rupture process, including both rupture velocity and shape of the temporal evolution of slip, show strong spatial heterogeneity. Dynamic rupture modeling with a heterogeneous stress field also shows that the rupture process can be significantly changed simply by altering the hypocenter (Guatteri et al., 2003). The complex source process plays a critical role in determining near-field ground motion characteristics, especially from large earthquakes. Thus, it is important for realistic strong ground motion prediction, to effectively characterize the source process. Classical kinematic approaches often fail to generate feasible source models for future events because arbitrary combinations of the source parameters, which are a characteristic of a kinematic source description, are likely to generate unrealistic ground motions, even though the earthquake rupture that the kinematic model is based on is a real physical process.

Dynamic rupture modeling is a useful tool for developing a physical understanding of the earthquake rupture process in terms of Newtonian mechanics. It also provides a basis for developing relationships between kinematic source parameters. Incorporating these relationships into kinematic rupture models has the potential to provide more reliable ground motion predictions. Complete dynamic modeling is a computationally demanding approach;

Reproduced with permission of the copyright owner. Further reproduction prohibited without permission.

whereas, kinematic modeling is not. Despite the computational attractiveness of the kinematic approach, however, if it can't be considered a viable alternative if it leads to unrealistic ground motions. Guatteri et al. (2004) developed a compromise approach that combined the efficient finite-source characterization of kinematic models, with important characteristics of physically self-consistent finite-source dynamic models. This has the potential to deliver the benefits of dynamic modeling, without the associated high computational cost. They termed it "pseudo-dynamic" modeling because it is a kinematic approach that seeks to emulate dynamic faulting behavior. To accomplish their objective, they developed several empirical relations between dynamic and kinematic source parameters that were based and inspired by a combination of theoretical results for dynamic rupture propagation in simple (semi-infinite) geometry and empirical analysis of spontaneously propagating dynamic rupture models. Their results seem promising for generating physics-based, finite-source models for ground motion simulations. Moreover, the derived empirical relations give us insights into how the kinematic source parameters are affected by dynamic parameters and source geometry. The method was originally designed for strike-slip earthquakes with a magnitude range of $6.4 < M < 7.2$. We need another validation process to apply the same method to larger events ($M > 7.2$).

In extending the magnitude range of the pseudo-dynamic modeling procedure to larger earthquakes ($M > 7.2$), we targeted large strike-slip events with long and narrow rupture dimensions. It is interesting to see how the earthquake rupture behavior changes with increasing rupture dimension. In large scale strike-slip (in-plane rupture) events, the sub-shear constraint used in by *Guatteri et al.* (2003) might be inconsistent with recent observations for supershear rupture in large strike-slip events (Bouchon et al., 2001; Bouchon and Vallèe, 2003; Dunham and Archuleta, 2004; Song et al., 2008). Also, the relatively fixed rupture width with increasing rupture lengths because of the limit in the seismogenic depth is likely to

Reproduced with permission of the copyright owner. Further reproduction prohibited without permission.

produce interesting features, in particular, in controlling the behavior of slip duration (rise time) with rupture length. We are now developing the next generation of the pseudo-dynamic modeling to cover larger earthquakes than before.

5.2. Constructing dynamic rupture models

The goal of our research is to avoid dynamic rupture modeling when constructing kinematic rupture models, but in order to develop the relationships between parameters that the pseudo-dynamic approach is based on, we need dynamic rupture models on which to base them. For this reason we developed a set of dynamic rupture models, consisting of 9 bi-lateral and 6 uni-lateral ruptures, for M_w 7.5 strike-slip earthquakes. Each of these models has different, heterogeneous slip realizations and hypocentral locations. The computational demands of the problem for dynamic rupture models require high-performance computing. The details of the modeling procedure are fully described below.

5.2.1. Slip realizations

Once the target magnitude and event type (strike-slip/dip-slip, etc.) are decided on, the rupture dimension can be determined using established source scaling relations (Wells and Coppersmith, 1994; Somerville et al., 1997; Mai and Beroza, 2000) that are consistent with observations of past earthquakes. We used a spatial random field model developed by Mai and Beroza (2002) to generate spatially variable slip distributions. In their study, previously published slip models (44 models for 24 events) obtained by kinematic finite-source inversion

Reproduced with permission of the copyright owner. Further reproduction prohibited without permission.

were collected and analyzed to understand their spectral behavior in the wave-number domain. They concluded that a von Karman autocorrelation function (ACF) best explains slip heterogeneity in past earthquakes. They also found that correlation lengths in the von Karman spectral density scale with earthquake size, i.e., magnitude and/or rupture dimension (length and width). These scaling relations are used to determine appropriate characteristic correlation lengths for our target events. Thus, to generate realistic slip models for future scenario earthquakes that honor the spatial distribution characteristics of the slip models of past events, we allow the phase spectrum to vary randomly, but preserve the decay in the spectral amplitude spectrum based on the correlation lengths with the von Karman autocorrelation function.

One example of a slip realization for a target earthquake of M_w 7.5 is shown in Figure 5.1 (a). This strike-slip earthquake has a long narrow rupture dimension (150 km along-strike, 15 km along-dip), which is typical of large strike-slip events. It is important to note that the correlation lengths in the along-strike and down-dip directions are significantly different for events with large ratios of rupture length to rupture width (Mai and Beroza, 2002). The correlation lengths used in this study are inferred more from the estimates of the long strike-slip events like the 1992 Landers, California and 1999 Izmit, Turkey, earthquake rather than averaged estimates, which include more equi-dimensional dip-slip events in subduction zones. The slip is tapered near the rupture boundaries except at the free surface, to prevent unrealistic boundary effects, such as high stress drop. Although we used the particular spatial random field model of Mai and Beroza (2002), there are other approaches available to characterize the spatial variability of earthquake slip (Andrews, 1980; Herrero and Bernard, 1994; Zeng et al., 1994; Sommerville et al., 1999; Lavallée et al., 2006).

Reproduced with permission of the copyright owner. Further reproduction prohibited without permission.

5.2.2. Stress drop and fracture energy

Stress drop and fracture energy are critical input parameters for dynamic rupture modeling. Although we are able to simulate realistic slip models for future scenario earthquakes, it is more challenging to take the same approach for the stress-related parameters because they are more spatially variable, and thus less well constrained by data. Stress drop, for example, is related to the spatial derivative of slip, which cannot be easily constrained by low-pass filtered ground motion data (< 1Hz). We compute the static stress drop from the assumed slip distributions using Okada's method (1992). This static stress drop is conceptually distinct from the dynamic stress drop that we need to use in the dynamic rupture modeling, but the expected difference (dynamic overshoot or undershoot) is assumed to be small – on the order of 10 or 20 % (Day, 1982a; Madariaga, 1976) – compared to the uncertainty we expect in the kinematic finite-source models (Mai et al., 2006). The computed static stress drop is used directly in the modeling without further modification. Okada's method (1992) uses a set of closed analytical solutions to calculate internal displacement and strain fields from shear or tensile faulting in a homogeneous half-space. We can take the free surface effect into account by using Okada's method whereas Guatteri et al. (2004) used the convolution integral method conducted in a whole space (Andrews, 1980).

Fracture energy (or surface energy) is a key element in earthquake rupture dynamics and is defined as the amount of energy per unit area required to extend the crack (Scholz, 1990). It is an important quantity because it controls many critical features of kinematic fault behavior, particularly the rupture velocity (Guatteri and Spudich, 2000), which is a major controlling factor for near-field ground motions. We used scaling relations developed by Mai et al. (2006)

Reproduced with permission of the copyright owner. Further reproduction prohibited without permission.

to generate corresponding fracture energy distribution for each event. This relationship is based on dynamic rupture modeling of a suite of earthquakes. In this formulation, the fracture energy scales with the stress intensity factor (stress drop times square root of crack length), based on dynamic rupture models constructed by spontaneous dynamic modeling (12 rupture models for 9 different earthquakes) as:

$$G_c = 0.041 + 0.0028\Delta\sigma\sqrt{L_h} \tag{5.1}$$

G_c is the fracture energy. $\Delta\sigma$ and L_h indicate stress drop and crack length, which is taken to be the distance from the hypocenter. They also derived scaling relations for both surface and sub-surface rupture earthquakes separately, but here we use the combined version for all events. Figure 5.1 (b) and (c) show one example of a computed stress drop and fracture energy distribution from a given slip model. Note that the area where the stress drop is negative, is assigned a constant minimum value (~ 0.1 MJ/m^2) to avoid the unphysical situation of negative fracture energy.

5.2.3. Slip weakening friction law

In the dynamic rupture modeling we need a fault constitutive law to govern the frictional behavior on the fault during slip. We assume a simple slip-weakening friction law without any healing regimes in the modeling (Ida, 1972; Andrews, 1976a) as shown in Figure 5.2. Even if our primary concern is the fracture energy, we need to divide it further into the slip-weakening distance and strength excess, in order to perform the dynamic rupture modeling under the slip-weakening friction law. The strength excess is the difference between the yield stress and the

Reproduced with permission of the copyright owner. Further reproduction prohibited without permission.

initial stress as shown in Figure 5.2. The fracture energy is the area under the slip-weakening curve. Given the stress drop distribution, we varied the ratio S given below (eq. 5.2) between 0.5 and 2.0 depending on the relative level of the fracture energy at each point with respect to the maximum fracture energy. Once the strength excess is determined, it is straightforward to compute the slip-weakening distance from the fracture energy and the strength excess. In this study it varies mostly between 0.3 and 1.3 m. The minimum slip-weakening distance is set to be 0.3 m if it is smaller than the minimum value.

$$S = \frac{\tau_s - \tau_o}{\tau_o - \tau_f} \tag{5.2}$$

Several studies have attempted to estimate the slip-weakening distance from real earthquake data, relating to fracture energy estimates (Ide and Takeo, 1997; Olsen et al., 1997), or independent of the fracture energy (Mikumo et al., 2003). Their estimates vary approximately between 0.5 and 1.0 m and are compatible with our values although resolving the slip weakening distance of real earthquakes is beyond the scope of this paper.

5.2.4. High performance computing

We need to treat dynamic rupture propagation for very large rupture dimension (rupture length ~ 150 km), which requires high performance computing capabilities of the recently launched computational facility in the Stanford School of Earth Sciences (CEES cluster, http://cees.stanford.edu). This facility contains two main clusters, one designed for Distributed Memory Programming (DMP) and the other for Shared Memory Programming (SMP). The

Reproduced with permission of the copyright owner. Further reproduction prohibited without permission.

DMP cluster is composed of a multiple set of nodes, and each node contains its own processor and memory while the SMP machine has multiple processors with large, shared memory. We decided to use the SMP machine because it is easier to parallelize existing dynamic rupture modeling codes in a shared-memory configuration. The SMP machine has 24 dual processors with about 200 gigabyte memory, which can handle about 4 billion nodes in our dynamic rupture modeling in its full capacity, but we used about 50 gigabyte memory in each modeling to handle about 1 billion nodes.

Because our immediate objective in this study is to investigate and characterize the rupture process on a fault, rather than to calculate ground motions that account for low velocity layers in the near surface, relatively coarse grid spacing (> 500 m) seems to be acceptable; however, in order to implement the slip-weakening friction law stably in the dynamic modeling, at least several grid points should be placed inside the cohesive zone so that the gradual decay of traction on the fault during slip is reproduced (Andrews, 2004; Day et al., 2005). We used 250 m grid spacing in the modeling and checked that at least 2-3 points represent the cohesive zone through the entire rupture propagation in most cases. It would be desirable to reduce the grid spacing even further (~100 m), so that we have more than 5 points in the cohesive zone to reduce numerical instability caused by the coarse discretization; however, our ability to decrease the grid spacing further is limited because of the limit in the available computing power. It may be helpful to implement an effective absorbing boundary condition in the current dynamic code to remove the large buffer zones that are currently used in the modeling to prevent non-physical boundary reflected phases from distorting the stress field on the fault.

5.2.5. Dynamic models

Reproduced with permission of the copyright owner. Further reproduction prohibited without permission.

We parallelized a 3-D finite difference dynamic rupture code (Andrews, 1999) using OpenMP in order to take advantage of the high performance computing. With it we performed spontaneous dynamic rupture modeling for a set of Mw 7.5 strike-slip (scenario) earthquakes. The 1-D velocity structure used in the modeling and some of the modeling parameters are given in Table 5.1 and 5.2, respectively. 15 dynamic rupture models were constructed using different slip realizations and hypocenter locations. 9 of the ruptures are bi-lateral where the hypocenter is located in the middle of the along-strike fault rupture, while 6 of them are uni-lateral where the hypocenter is located near the left or right end of the rupture. It can be difficult to assess in advance whether or not a dynamic rupture will propagate spontaneously, and there is always the possibility that rupture will terminate in the middle of the assumed rupture extent. This holds true even if we use the approximate relations of Guatteri et al. (2004); however, in this study we found that the fracture energy scaling works quite well and required only 18 runs to obtain the 15 spontaneous dynamic rupture models.

Figure 5.3 shows an example of the dynamic modeling results for 5 key parameters in kinematic fault motions for both bi- and uni-lateral rupture. Both have the same starting slip distribution, but their hypocenters differ. Although they produce approximately the same slip distribution, other parameters show strong dependency on the hypocenter location. It is interesting to note the almost constant rise time after the rupture has propagated a certain distance, in particular, in the uni-lateral rupture shown in Figure 5.3. These five parameters (slip, rupture time, peak slip velocity, pulse width, and rise time) will be used to characterize our pseudo-dynamic source models for ground motion simulations. Depth-averaged slip rate is also shown for both bi- and uni-lateral rupture (Figure 5.4). Rupture velocity and approximate rise time in the along-strike direction is also inferred in the plot. Super-shear rupture occurs

Reproduced with permission of the copyright owner. Further reproduction prohibited without permission.

locally at approximately 20 km from the hypocenter in both cases, but the rupture velocity tends to revert to sub-shear as the rupture approaches the fault boundary.

5.3. Pseudo-dynamic source characterization

For strong ground motion prediction we need to perform multiple, perhaps hundreds to thousands, realizations of an earthquake in order to take into account of the full range of earthquake rupture scenarios. Exploring the sources of variability due to source processes is essential to reliable ground motion predictions (attenuation relations), because stable and accurate measures of the intensity and variability of ground motions are not likely to be obtained with a small set of simulations. Although full dynamic rupture modeling provides us with a unique opportunity for physics-based earthquake source modeling, it is a computationally intensive approach, which makes it less efficient to use for such ground motion simulations. Here we extract key parameters in kinematic fault motions, i.e., rupture velocity, peak slip velocity, pulse width, and rise time, from the dynamic models and derive empirical relations between the dynamic and kinematic source parameters. Using the derived empirical relations, we develop an efficient finite-source characterization for ground motion prediction. We first start with rupture velocity and determine how it is related to other source properties. We then discuss in detail how to characterize the shape of temporal evolution of slip, i.e., slip velocity function (SVF), in our pseudo-dynamic modeling approach.

5.3.1. Toward the next generation of pseudo-dynamic modeling

Reproduced with permission of the copyright owner. Further reproduction prohibited without permission.

The pseudo-dynamic modeling method was introduced by Guatteri et al. (2004) as an efficient way of producing physics-based earthquake source models for ground motion predictions. The method was originally designed for strike-slip earthquakes with a magnitude range of $6.4 < M < 7.2$, thus its application to larger earthquakes ($M > 7.2$) where the width of the source has a strong effect on the evolution of rupture, requires an updated procedure that is validated for these larger magnitudes. Increased earthquake size and rupture dimension will introduce interesting and important changes in the earthquake rupture process that are not observed in moderate-sized earthquakes (Scholz, 1982). Currently, we can generate dynamic models as large as $M \sim 7.5$ for strike-slip events with rupture lengths of ~150 km compared to 30 - 40 km in the previous study.

Much larger, i.e. longer, strike-slip earthquakes are possible. For example, the M_w 7.9 1906 San Francisco earthquake experienced significant rupture through the entire ~500 km northern segment of the San Andreas fault (Song et al., 2008). Thus, earthquakes that are larger than we can handle in the current study are of great interest. Ideally we would include dynamic models of such events in developing our pseudo-dynamic formulation, but it is not practical given our computational limitations. On the other hand, a rupture length of 150 km with a width of 15 km has an aspect ratio of 10:1 and is sufficiently long to span the transition to a long, narrow rupture (Shaw and Scholz, 2001). For that reason we expect that extending the model to even larger earthquakes than we can currently model should be straightforward.

5.3.1.1. Relaxing the sub-shear rupture velocity constraint

Reproduced with permission of the copyright owner. Further reproduction prohibited without permission.

The most important new characteristic of our target events is a long narrow rupture dimension, which is the norm for large strike-slip events due to the limited depth extent of possible elastic strain accumulation. This characteristic of large strike-slip events is found universally, although there is some controversy about the point at which it becomes important in rupture dynamics (Scholz, 1982; Shaw and Scholz, 2001). Recent source studies of large strike-slip earthquakes indicate that super-shear rupture, i.e., rupture velocity exceeding the shear wave velocity of the Earth's crust, is possible, and perhaps even typical for large in-plane strike-slip earthquake ruptures (Bouchon et al., 2001; Bouchon and Vallée, 2003; Dunham and Archuleta, 2004; Ellsworth et al., 2004; Song et al., 2008). The previous pseudo-dynamic formulation was based on the premise that rupture velocity ought to remain sub-shear, and hence it incorporates a constraint that encouraged this. Recent observations of super-shear rupture in earthquakes have motivated us to eliminate this constraint from the pseudo-dynamic formulation. Our dynamic modeling results show super-shear rupture velocity at least in some areas (Figure 5.3). The rupture velocity is an important factor for near-field ground motion and leads to different wave propagation patterns for the sub-shear and super-shear cases. As a result, super-shear rupture will generate profoundly different near-field ground motion attenuation characteristics compared with sub-shear rupture (Aagaard and Heaton, 2004). Thus, it is important to account for this feature of earthquake rupture in the pseudo-dynamic source characterization.

5.3.1.2. Rise time scaling

Most crack-type solutions suggest that after slip initiates, a point on a fault starts healing only when it receives a signal (stopping phase) from the fault boundary (Madariaga, 1976).

Reproduced with permission of the copyright owner. Further reproduction prohibited without permission.

Consequently, the duration of slip at a point on the fault (the rise time) tends to increase as the rupture dimension increases. Most kinematic source models support relatively short slip duration, which cannot be simply explained by the simple crack-type solutions (Heaton, 1990). Several mechanisms have been suggested to explain short slip duration in the framework of dynamic rupture propagation either due of dynamic frictional behavior on a fault during rupture (Cochard and Madariaga, 1994; Nielsen and Carlson, 2000) or due to spatial heterogeneities in the stress field (Beroza and Mikumo, 1996).

Guatteri et al. (2004) found that the rise time scales linearly with rupture duration in their spontaneous dynamic rupture models that used a slip-weakening law (Ida, 1972; Andrews, 1976). Their scaling relations for rise time with the rupture dimension seem feasible for moderate size earthquakes with relatively small rupture dimension, but are unlikely to apply for large, and hence long, strike-slip earthquakes. With such geometry, the rise time cannot increase linearly with the increasing rupture dimension. Instead, we expect that the finite width of the rupture will exert a strong influence on the rise time (Day, 1982a). Our modeling results (Figure 5.3 and 5.4) support this idea by showing that short, and nearly constant, rise time is observed after the rupture passes a certain distance from the initial nucleation area. This effect is most clearly observed in the uni-lateral rupture, where we expect it to be best developed. The duration of slip is controlled by the narrow rupture width (~15 km) used in the modeling although the rupture length is very large (~150 km). We need to incorporate this behavior in the pseudo-dynamic modeling relations.

5.3.2. Rupture velocity

Reproduced with permission of the copyright owner. Further reproduction prohibited without permission.

Rupture velocity exerts a strong control on near-field ground motion characteristics and it, in turn, is influenced by both the stress drop and fracture energy distribution. Guatteri et al. (2004) adopted a 2-D analytic solution to relate the rupture velocity with dynamic parameters, i.e., stress drop, fracture energy, and crack length, derived by Andrews (1976a). They found that the analytic solution developed in the simple 2-D homogeneous case could also be applied, locally, to their 3-D heterogeneous problems reasonably well. Our case is different, because in applying the same relation to the case of a long strike-slip event, the relation, which is derived for the 2-D anti-plane case, is clearly violated because our target events have a very long and narrow rupture dimension in the in-plane direction. Moreover, the solution is derived under the sub-shear rupture velocity assumption, which is an assumption we don't want to make.

It is challenging to infer the rupture velocity relation with available dynamic parameters since the rupture velocity is affected not only by local stress field, but by the dynamic load, which depends on entire rupture history, within the causal region. Furthermore we need to handle the rupture velocity in both the super- and sub-shear regimes and to transition between them in a 3-D heterogeneous field. All of this makes the problem difficult to treat (Eric Dunham, personal communication). Because of the complexities of the problem, we adopted an empirical, data-oriented approach to relate the rupture velocity with other source parameters. Figure 5.5 (a) shows an example of the rupture time distribution extracted from the dynamic rupture modeling. Instantaneous (or local) rupture velocity can be computed by equation (5.3) from the rupture time distribution as shown in Figure 5.5 (b).

$$v(x,y) = \frac{1}{|\nabla t(x,y)|} \tag{5.3}$$

Reproduced with permission of the copyright owner. Further reproduction prohibited without permission.

where t(x,y) represents rupture time distribution on a 2-D fault plane. We found that this instantaneous rupture velocity scales with the final slip distribution, as shown in Figure 5.6, although we note some significant deviations from the regression line that are not easily predicted. It is somewhat surprising that the rupture velocity scales with the scalar value slip at each point on the fault, without any consideration of the fracture energy or rupture propagation history. We might be able to predict better the rupture velocity and reduce the variance in the regression plot (Figure 5.6) if we accounted for other effects in the rupture velocity scaling relation in the 3-D heterogeneous field, but to first order, the slip regression does a reasonable job of predicting the rupture velocity. The resulting rupture velocity can be also weighted with azimuth and crack length to help account for the rupture propagation effect.

5.3.3. Slip velocity function (SVF)

How slip evolves and terminates after a certain point on a fault starts slipping, has long been a topic of great interests for seismologists. Compared to the final slip and the rupture velocity, however, the actual shape of the source time function is poorly constrained from kinematic waveform inversion. According to spontaneous dynamic rupture modeling results with slip-weakening, the fault starts slipping with high slip rate for a relatively short amount of time and continues to slip with a low and decreasing slip rate, leading to a long tail in the SVF. Despite the heterogeneity involved in the dynamic modeling, the overall shape of the temporal evolution of slip is well approximated by the Kostrov-type ($t^{-1/2}$ decay) slip velocity function. Guatteri et al. (2004) characterized this feature using two overlapping triangles (T1 and T2) as shown in Figure 5.7. The triangle T1 represents the portion of the SVF with high slip rate and short duration that we expect to make the major contribution to seismic radiation at high

Reproduced with permission of the copyright owner. Further reproduction prohibited without permission.

frequencies. The triangle T2 completes the SVF, with a long tail at low slip rate. T_p and τ_r represent the pulse width and the rise time, respectively. T_p is defined as the time until half of the total slip occurs. V_{max} is the peak slip velocity of the whole SVF and the constant, c, defines the height of the triangle T2, and is determined depending on the ratio of τ_r to T_p. Thus, we can generate the whole trace of the slip velocity function to capture most of the main features of the temporal evolution of slip inferred from rupture dynamics by determining only those three parameters, i.e., V_{max}, T_p, and τ_r. We now analyze the dynamic modeling outputs to determine the empirical relations that relate these quantities with available dynamic source parameters.

5.3.3.1. Peak slip velocity

Day (1982a) shows that V_{max} can be approximated by equation (5.4) for a long and narrow fault rupture in a homogeneous whole space. He extracted the peak slip velocity from the closed-form analytic SVF of Kostrov (1964) obtained from an expanding circular crack and replaced radius, r, in the solution with fault width, W, since the finiteness of the fault width terminates the growth of the peak slip velocity as rupture propagates. The approximation successfully captures the peak slip rate from the numerical modeling in his study. Even though the rupture dimension considered in this study is much larger (more than 10 times) and we consider heterogeneous 3-D problems, and the free surface, his prediction works quite well as shown in Figure 5.8.

$$V_{max} = \sqrt{2f_c W V_r}\,\frac{\Delta\sigma}{\mu} \tag{5.4}$$

Reproduced with permission of the copyright owner. Further reproduction prohibited without permission.

$\Delta\sigma$ and V_r are stress drop and rupture velocity, respectively. W is the fault width. f_c and μ indicate cut-off frequency of the slip velocity function and shear modulus, respectively. The slip velocity function from the dynamic modeling is low-pass filtered up to 1 Hz ($f_c = 1$) and μ is derived from the velocity structure given in Table 5.1.

5.3.3.2. Pulse width

Slip duration for the first half of slip, i.e., the pulse width, T_p, as defined in the previous study, is expected to be controlled strongly by V_{max} in the form of slip velocity function we adopted (Figure 5.8). Guatteri et al. (2004) suggests equation (5.5) for the pulse width calculation and their assumption works well even in this study (Figure 5.9).

$$T_p = \beta \frac{\text{slip}}{V_{max}} \tag{5.5}$$

β can be obtained from fitting a line to the data in Figure 5.9.

5.3.3.3. Rise time

Guatteri et al. (2004) showed that rise time has a linear scaling relation with the difference between the effective total rupture duration and rupture time for earthquakes with $6.4 < M < 7.2$. For the new set of dynamic models for M 7.5 strike-slip events, however, this relationship

Reproduced with permission of the copyright owner. Further reproduction prohibited without permission.

breaks down. Note the flattened area in the middle of the bi-lateral rupture (in Figure 5.10) and the short rise time (~ 2 secs) with very gradual decrease in the uni-lateral rupture after a certain rupture distance. This is somewhat surprising because we did not implement any healing schemes in the fault friction law, the traction remains at the final sliding friction level (τ_f) until the end of slip, and the total rupture duration is about 25 and 45 seconds for bi- and uni-lateral ruptures, respectively. This behavior is predicted by the relationship given in Day (1982a) that assumes that rupture behavior for long faults is largely controlled by rupture width, not length. Factors like local stress heterogeneities and proximity to fault boundaries and negative stress drop regions, which can be considered to act as a local barrier to rupture, may cause substantial variations from the regression line, but for all of the rupture models we developed, the major contribution in determining the slip duration and its behavior seems to be made by the relatively small fault width. This could be considered further evidence that short slip duration can be obtained by properly considering the fault geometry without appealing to, for example, healing due to velocity-dependent friction. The rise time here is defined as time it takes from 10 to 80 % of the total slip occurs. We ignore the 20 % of the total slip in the tail of the slip evolution so we don't overestimate the effective duration of slip in some regions of the rupture area that slip slowly for a long time. Since no self-healing scheme is included in the friction law, we expect to see continuous evolution of slip with very low slip rate in the tail of the slip velocity function in particular with relatively long rupture duration as in this study. Because this will have a negligible contribution to strong ground motion, we don't need to include it.

5.3.4. Pseudo-dynamic modeling results

Reproduced with permission of the copyright owner. Further reproduction prohibited without permission.

Figure 5.11 and 12 show the comparison of the pseudo-dynamic source modeling results with the dynamic modeling outputs. The pseudo-dynamic modeling is performed based on the regression analysis described above. Rupture time is calculated from the estimated local rupture velocity, assuming a straight line path between the hypocenter and each point. This will deviate from the real rupture propagation; however, the principal characteristics of the dynamic model are reproduced, including both the absolute time of the rupture and the pattern of the rupture front. Peak slip velocity is one of the most stable parameters predicted using the pseudo-dynamic approach. Although we used the pseudo-dynamic rupture velocity estimates in equation (5.4), the pseudo-dynamic peak slip estimates show a strong correlation with the dynamic modeling results; in most cases, the correlation coefficient between them is larger than 0.6. Figure 5.13 shows that the rupture time and peak slip velocity of large strike-slip earthquakes can be successfully predicted by the pseudo-dynamic modeling developed in this study within a reasonable range.

We now have a better understanding on the slip duration from the dynamic modeling outputs obtained in this study, especially when earthquake rupture has a very long and narrow rupture dimension; however, our ability to predict the details of the heterogeneity observed in the dynamic modeling in terms of both pulse width and rise time is limited. The pulse width has a strong correlation with the ratio of the slip to peak slip velocity as shown in Figure 5.9, but modeling errors accumulate in the pseudo-dynamic modeling, i.e., from rupture velocity through peak slip rate to pulse width estimation, which leads to the unsatisfactory pulse width predictions. It is encouraging that we still have rough, but realistic constraints on the slip duration from this study, but it may be helpful to perform ground motion simulations to test the effect of the limit in the slip duration prediction.

Reproduced with permission of the copyright owner. Further reproduction prohibited without permission.

5.4. Discussion

We used the fracture energy scaling relations obtained by Mai et al. (2006) to assign the fracture energy for a given stress drop distribution in the dynamic modeling and obtained dynamic rupture models effectively without the need for much trial and error modeling of the assumed fracture energy distribution. 18 dynamic runs were performed to obtain 15 spontaneous dynamic rupture models. Since the modeling is carried out for scenario earthquakes, not much in the way of kinematic constraints is available except for the final slip. The fracture energy scaling with stress drop proved to be very useful in assigning initial conditions for dynamic rupture modeling as expected previously (Guatteri et al., 2004, Mai et al., 2006). Several studies show that the fracture energy scales with earthquake size, i.e., seismic moment (Abercrombie and Rice, 2005; Tinti et al., 2005; Mai et al., 2006). It may be more reasonable to adopt different scaling relations as the earthquake size increases, in particular, if we want to model extremely large strike-slip earthquakes (M ~ 8.0). The scaling relation of the fracture energy with the stress intensity factor (stress drop times the square root of crack length) comes from spontaneous dynamic modeling experiments with a slip-weakening law (Guatteri et al., 2004) although linear elastic fracture mechanics suggests that fracture energy scales with the square of the stress intensity factor instead (Scholz, 1990). Rice et al. (2005) propose a model relating an average fracture energy for each event with the square of slip and this scaling relation is observed by Abercrombie and Rice (2005) and is also tested in heterogeneous finite rupture models (Tinti et al., 2005). We may also be able to use this scaling relation to assign the fracture energy.

Reproduced with permission of the copyright owner. Further reproduction prohibited without permission.

Mai et al. (2006) developed separate fracture energy scaling relations for surface and subsurface earthquakes, motivated by the observation that recorded ground motions from earthquakes that produce large surface rupture are systematically weaker than those from buried events (Somerville, 2003). They find that the fracture energy increases significantly faster with the stress intensity factor for the surface rupture earthquakes than for the subsurface rupture, suggesting that surface breaking events consume more fracture energy than buried events. It may be useful to develop a different version of the pseudo-dynamic modeling method for surface and subsurface rupture to see how earthquake source models are parameterized in both cases by the pseudo-dynamic modeling, and to understand the consequences for strong ground motion.

It is a bit surprising that the local rupture velocity scales with the slip amplitude as shown in Figure 5.6. In a 2-D homogeneous anti-plane rupture, Andrews (1976a) predicts that the rupture velocity should be related to a functional form of stress drop, fracture energy, and crack length. We may be able to predict better the perturbation in the regression plot to take into account the fracture energy and other propagation effects, but as a first approximation, the empirical relationship based on the slip is surprisingly effective.

Compared to rupture velocity and peak slip rate, we are quite limited in our ability to predict slip duration, either the pulse width or the rise time, although now we have a better idea of how fault width acts to limit the slip duration as earthquake rupture dimension increases in one direction only. The obvious next step is to perform ground motion simulations to test how this limit in slip duration affects characteristics of strong ground motion.

Reproduced with permission of the copyright owner. Further reproduction prohibited without permission.

In this study the shape of the slip velocity function is simplified with two overlapping triangles to represent main features of the temporal evolution of slip observed in the spontaneous dynamic rupture modeling with the slip weakening friction law. Tinti et al. (2005) suggested the regularized Yoffe function as a possible way of the slip velocity function parameterization to be used in kinematic ground motion modeling. Their parameterization is also based on dynamic rupture propagation with finite slip-weakening distances. It may provide a smoother version of the slip velocity function and can be adopted as an alternative SVF parameterization approach in our pseudo-dynamic source characterization.

Finally, we expand the magnitude coverage of the pseudo-dynamic modeling method greatly through this study to larger events (M > 7.5). Still larger earthquakes are also of interest, but dynamically modeling such events is beyond our present capabilities; however, we note that a rupture length of 150 km with a width of 15 km has an aspect ratio of 10:1 and is sufficiently long to span the transition to a long, narrow rupture (Shaw and Scholz, 2001). For that reason we expect that extending the model to larger earthquakes should be straightforward.

5.5. Conclusions

We have developed a new version of the pseudo-dynamic modeling method to produce physics-based finite earthquake source models for ground motion prediction for large strike-slip earthquakes (M ~ 7.5). The current dynamic rupture code is parallelized using OpenMP to take advantage of high performance computing in the dynamic rupture modeling. A set of dynamic rupture models for Mw 7.5 strike-slip earthquakes are constructed with different slip realizations and hypocentral locations and are analyzed to extract empirical relations between

Reproduced with permission of the copyright owner. Further reproduction prohibited without permission.

dynamic and kinematic source parameters. These relationships are used for the basis for pseudo-dynamic rupture modeling. The dynamic rupture modeling starts with simulating slip models for future scenario earthquakes. These are based on characteristics of past events, and the corresponding stress drop and fracture energy distributions are derived from them. The fracture energy scaling relations with stress drop obtained by Mai et al. (2006) can be successfully used to set initial conditions for dynamic rupture modeling as shown in this study.

The new results show that we need new approaches for the pseudo-dynamic modeling of large earthquakes. In particular, for large strike-slip events which have a long and narrow rupture dimension, scaling relations with earthquake size introduce some interesting features since the increasing rupture dimension is almost entirely the rupture length, while rupture width remains fixed because of the depth limit of the elastic-brittle crust in the Earth. For long strike-slip earthquakes, slip duration is controlled by the narrow fault width even though the rupture dimension continues to increase in the along-strike direction. The improved pseudo-dynamic modeling method allows for the possibility of super-shear rupture propagation, which has been observed recently in the large strike-slip earthquakes. Our regression analysis shows that local rupture velocity scales with slip at the same point and that this relation can be used to obtain rupture time distributions for future scenario earthquakes based on the assumed slip distribution. In our pseudo-dynamic source characterization, temporal evolution of slip is simplified with two overlapping triangles, which captures many of the main features of the source time function seen in the dynamic rupture modeling. The improved method enables us to simulate realistic strong near-field ground motions from more reliable physically self-consistent finite earthquake source models and our method can be applied to large strike-slip events ($M \sim 7.5$).

Reproduced with permission of the copyright owner. Further reproduction prohibited without permission.

Acknowledgements. We would like to thank Joe Andrews for letting us use his 3-D dynamic rupture code (Andrews, 1999) and the CEES (http://cees.stanford.edu) for generously providing us with the high performance computing facilities. This work was supported by SCEC and the National Science Foundation.

Reproduced with permission of the copyright owner. Further reproduction prohibited without permission.

Table 5.1. 1-D velocity structure used in the modeling (Boore and Joyner, 1997)

Top depth (km)	Vp (km/sec)	Vs (km/sec)	Density (g/cm3)
0.0	5.50	2.90	2.74
4.0	5.70	3.30	2.78
8.0	6.06	3.50	2.80
14.0	6.79	3.92	2.80
16.6	7.10	4.10	2.90
27.0	8.00	4.62	3.20

* The first four layers from the top in the near surface are removed from the original velocity model and the fifth layer is assumed to be extended to the surface to avoid very low wave-propagation velocities in the modeling.

Table 5.2. Modeling parameters used in the study

Grid spacing	dx = 250 m, dy = 250 m, dz = 250 m
Time increment	18 msec
Total time steps	1,500 ~ 2,500
Normal stress	200 MPa
μ_f (sliding friction)	0.4
Initial nucleation patch (circle)	radius: 1.5 ~ 2.5 km
Slip weakening distance	0.3 m < d_c < 1.3 m
S (ratio of strength excess to stress drop)	0.5 ~ 2.0

Reproduced with permission of the copyright owner. Further reproduction prohibited without permission.

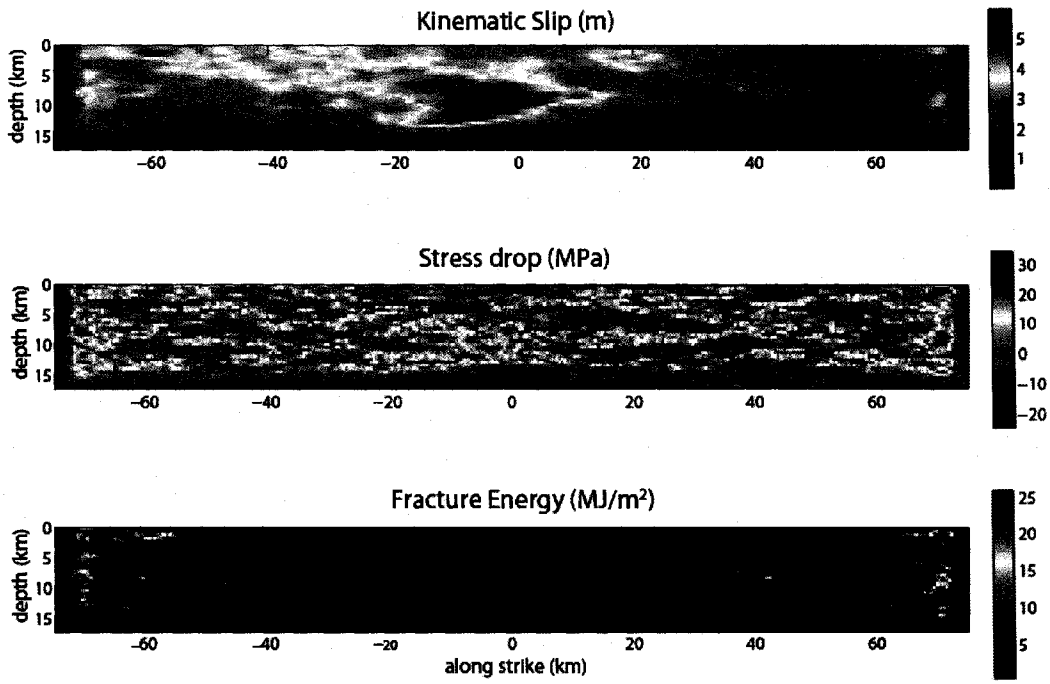

Figure 5.1. One example of slip realizations and stress drop and fracture energy distribution derived from the given slip distribution. The stress drop is computed from the given slip model using the Okada's method (1992) and the fracture energy distribution is obtained by the scaling relation with respect to stress intensity factor, $\Delta\sigma * L^{1/2}$ (Mai et al., 2006). Note that the plotted fracture energy has a minimum value of 0.1 MJ/m^2 in the negative stress drop region.

Reproduced with permission of the copyright owner. Further reproduction prohibited without permission.

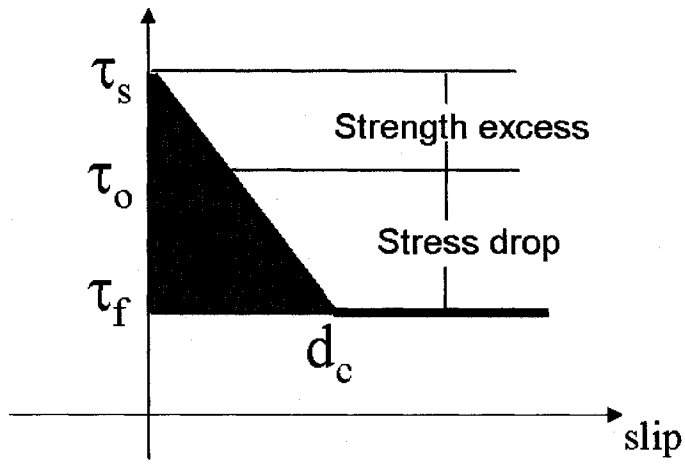

Figure 5.2. Slip weakening friction law (Ida, 1972; Andrews, 1976). τ_o, τ_f, and τ_s indicate initial, final, and yield stress (or rock strength), respectively. d_c denotes the slip weakening distance and the gray area represents fracture energy. In the friction law, traction on a faulting plane decays as the fault starts slipping as a function of slip until the slip reaches the slip weakening distance and it remains at the final stress level without any fault re-strengthening procedure until the end of the slipping.

Reproduced with permission of the copyright owner. Further reproduction prohibited without permission.

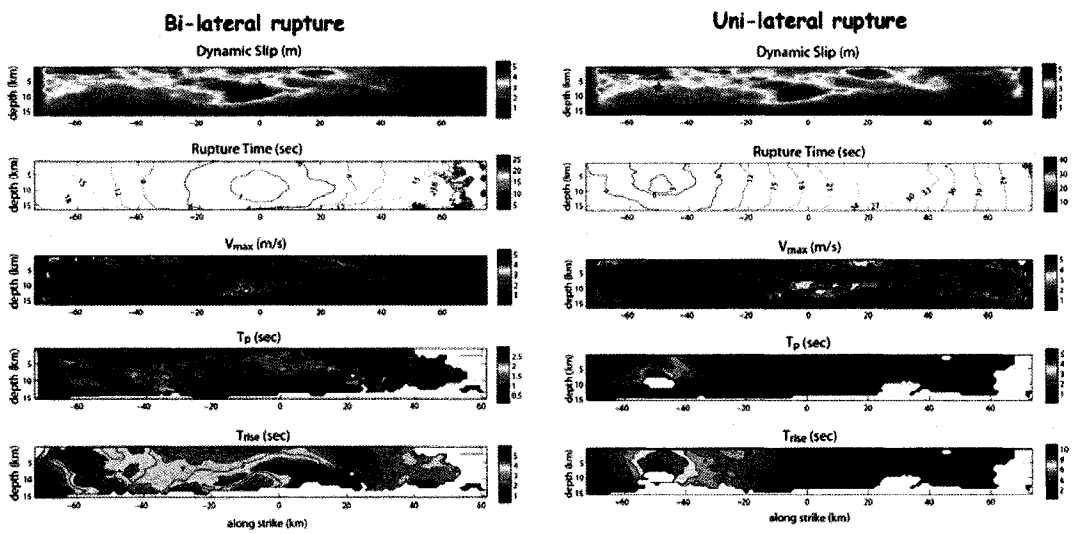

Figure 5.3. One example of dynamic modeling outputs for both bi- and uni-lateral ruptures. Five kinematic source parameters are extracted from dynamic modeling outputs and plotted for both bi- and uni- lateral ruptures. Both have the same starting slip distribution (Figure 5.1), but different hypocenter locations (stars in the plot). These five parameters are key elements in our "pseudo-dynamic" source characterization. The pulse width (T_p) is defined as the time it takes for half of the total slip to occur.

Reproduced with permission of the copyright owner. Further reproduction prohibited without permission.

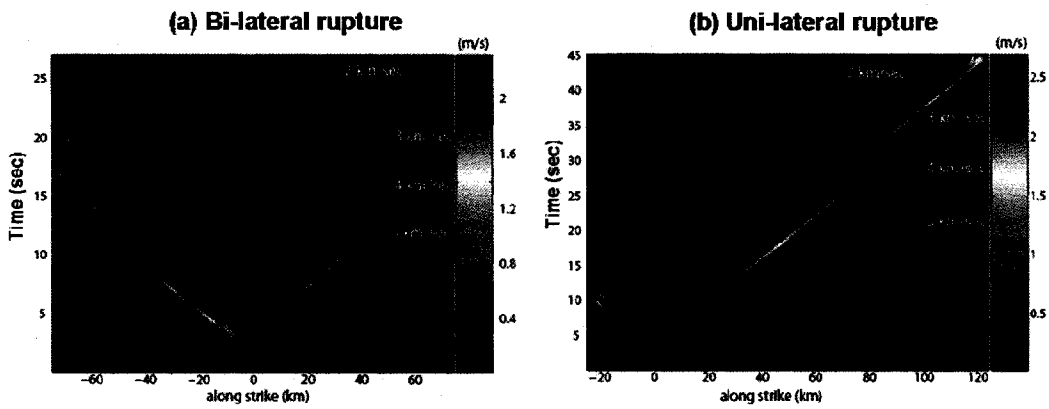

Figure 5.4. Depth-averaged slip rate as a function of along-strike distance and time for both bi- and uni-lateral ruptures. Four reference rupture velocity lines are also shown and approximate rise time along strike is also inferred in the figure. Note the short and almost constant rise time in the uni-lateral rupture after the rupture passes a certain distance.

Reproduced with permission of the copyright owner. Further reproduction prohibited without permission.

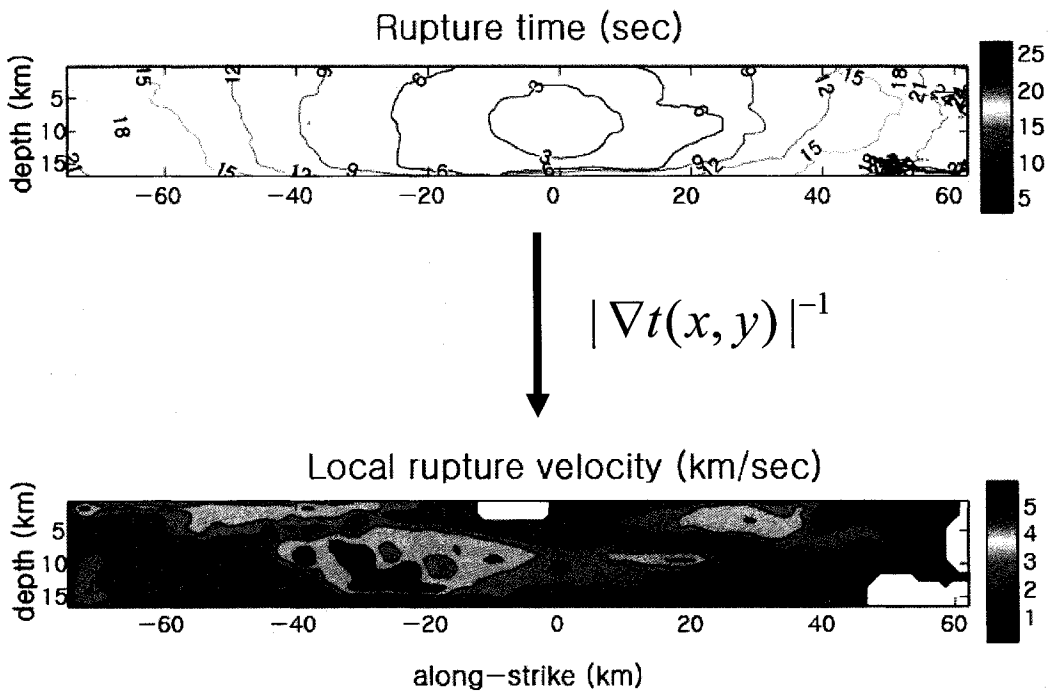

Figure 5.5. Rupture time distribution from Figure 5.4 (a) and instantaneous (local) rupture velocity derived from the rupture time distribution by equation (5.3).

Reproduced with permission of the copyright owner. Further reproduction prohibited without permission.

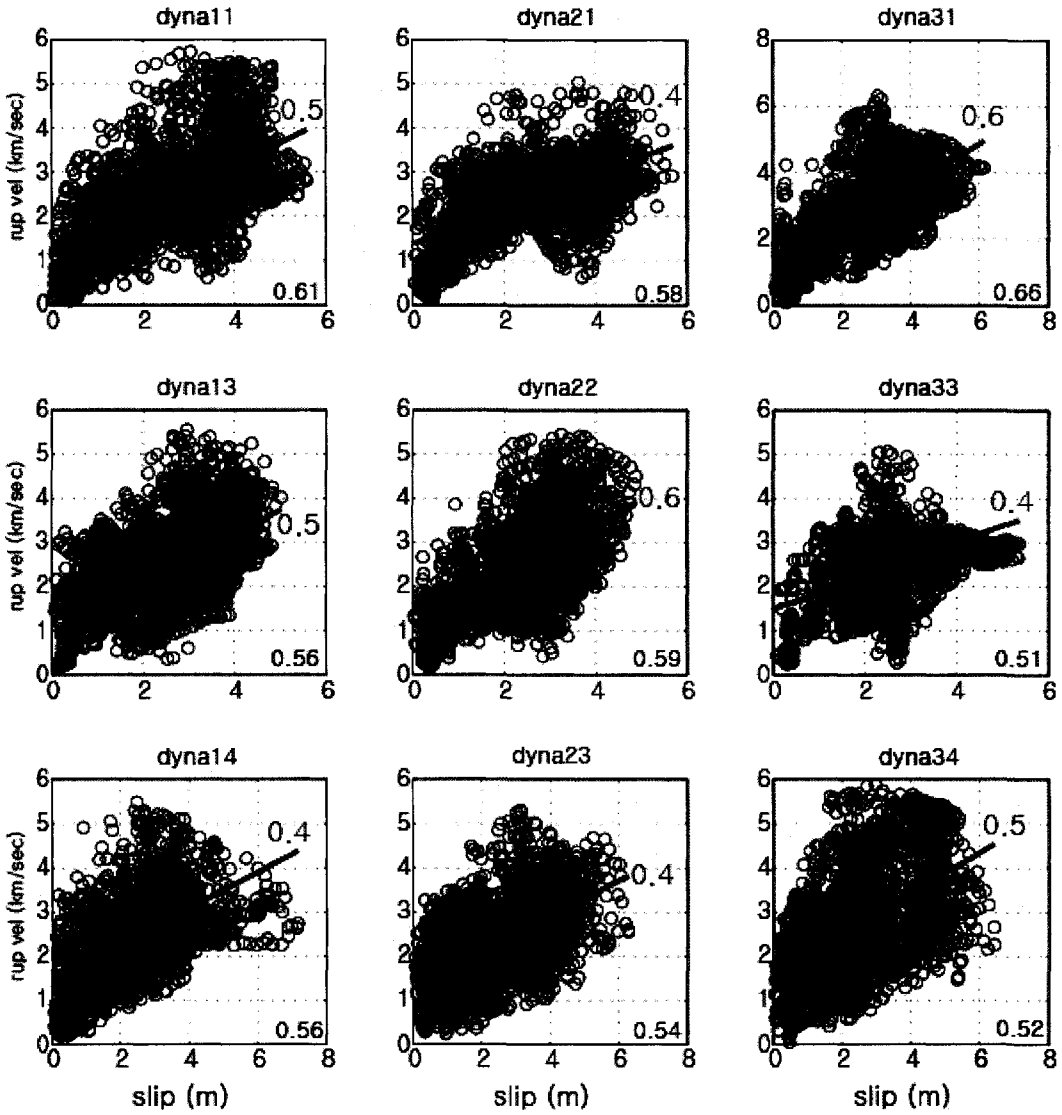

Figure 5.6. Scaling of (local) rupture velocity with slip for the set of 9 bi-lateral rupture models. Corresponding correlation coefficients are shown on the bottom right corner in blue and the regression lines are also shown in red with estimated slopes.

Reproduced with permission of the copyright owner. Further reproduction prohibited without permission.

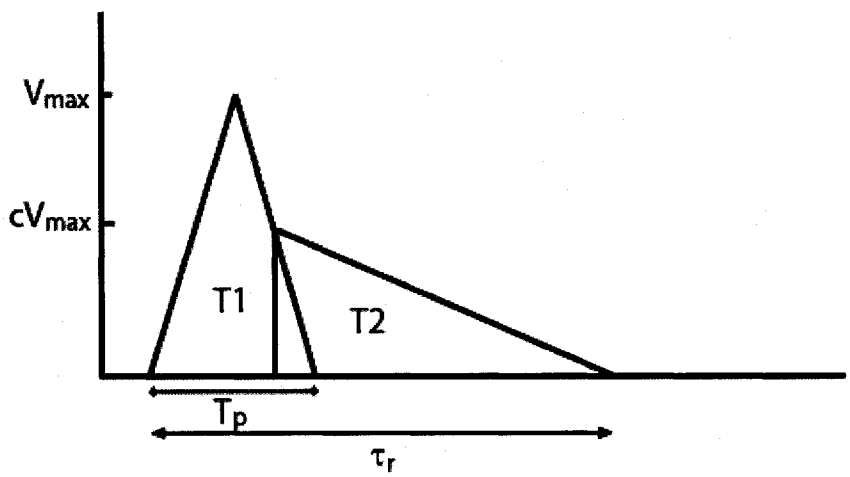

Figure 5.7. Slip velocity function parameterization using two triangles in the PD approach. T_p and τ_r represent pulse width and rise time, respectively. cV_{max} indicates the height of the rectangular triangle and the constant c is determined depending on the ratio of the pulse width to rise time.

Reproduced with permission of the copyright owner. Further reproduction prohibited without permission.

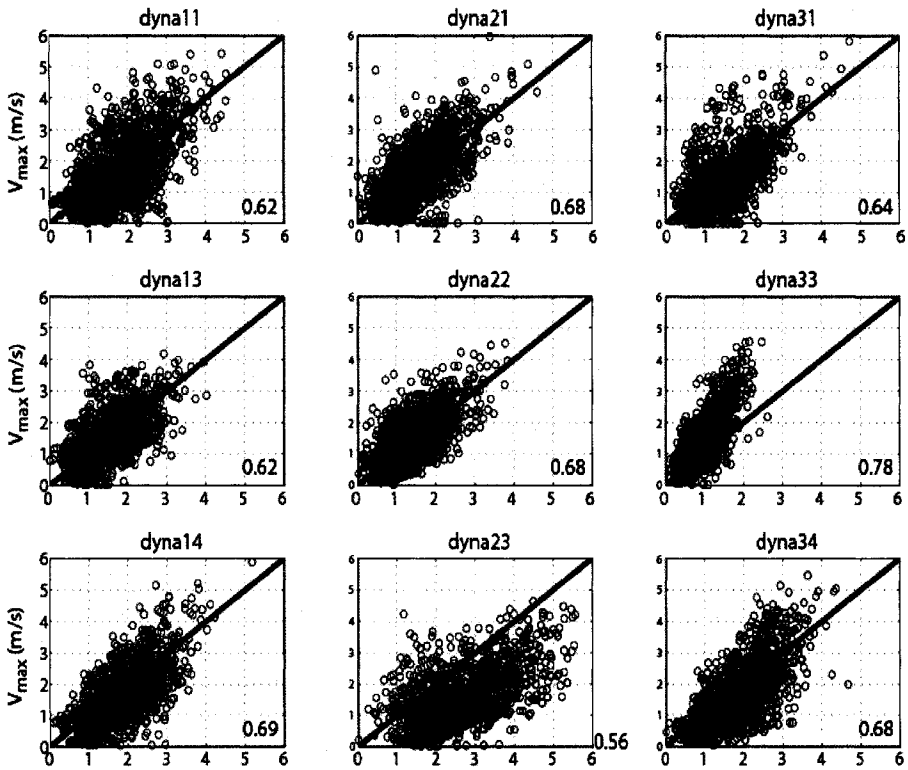

Figure 5.8. Peak slip velocity for the set of 9 bi-lateral rupture models vs. predicted values from the equation (5.4) suggested by Day (1982a). Corresponding correlation coefficients are given on the bottom right corner in blue. The red line shows a reference line with slope 1.

Reproduced with permission of the copyright owner. Further reproduction prohibited without permission.

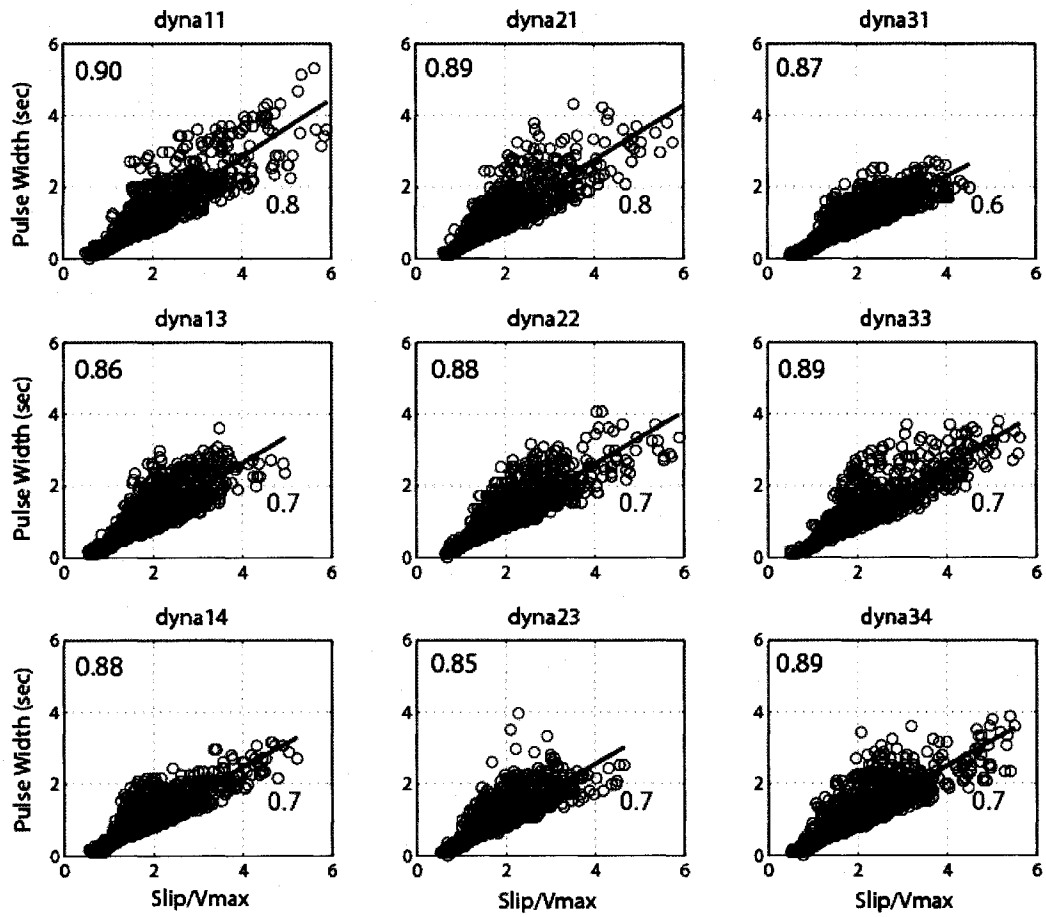

Figure 5.9. Pulse width for the set of 9 bi-lateral rupture models as a function of slip/V_{max}. Corresponding correlation coefficients are given on the top left corner in blue and estimated slopes below the regression line in red

Reproduced with permission of the copyright owner. Further reproduction prohibited without permission.

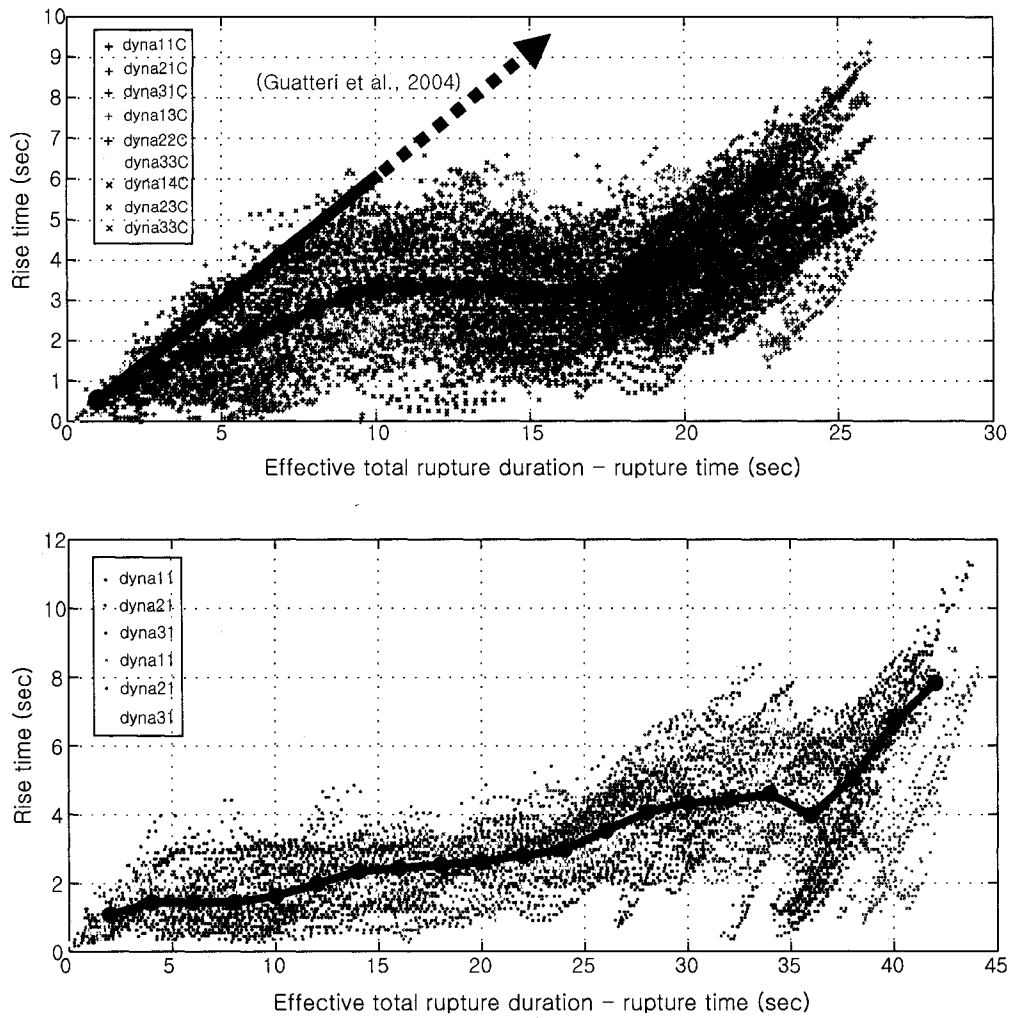

Figure 5.10. Rise time as a function of total fault rupture duration and rupture time for all 9 bi-lateral (a) and 6 uni-lateral (b) dynamic rupture models constructed in this study. The line in brown shows the median line of all those dots.

Reproduced with permission of the copyright owner. Further reproduction prohibited without permission.

Reproduced with permission of the copyright owner. Further reproduction prohibited without permission.

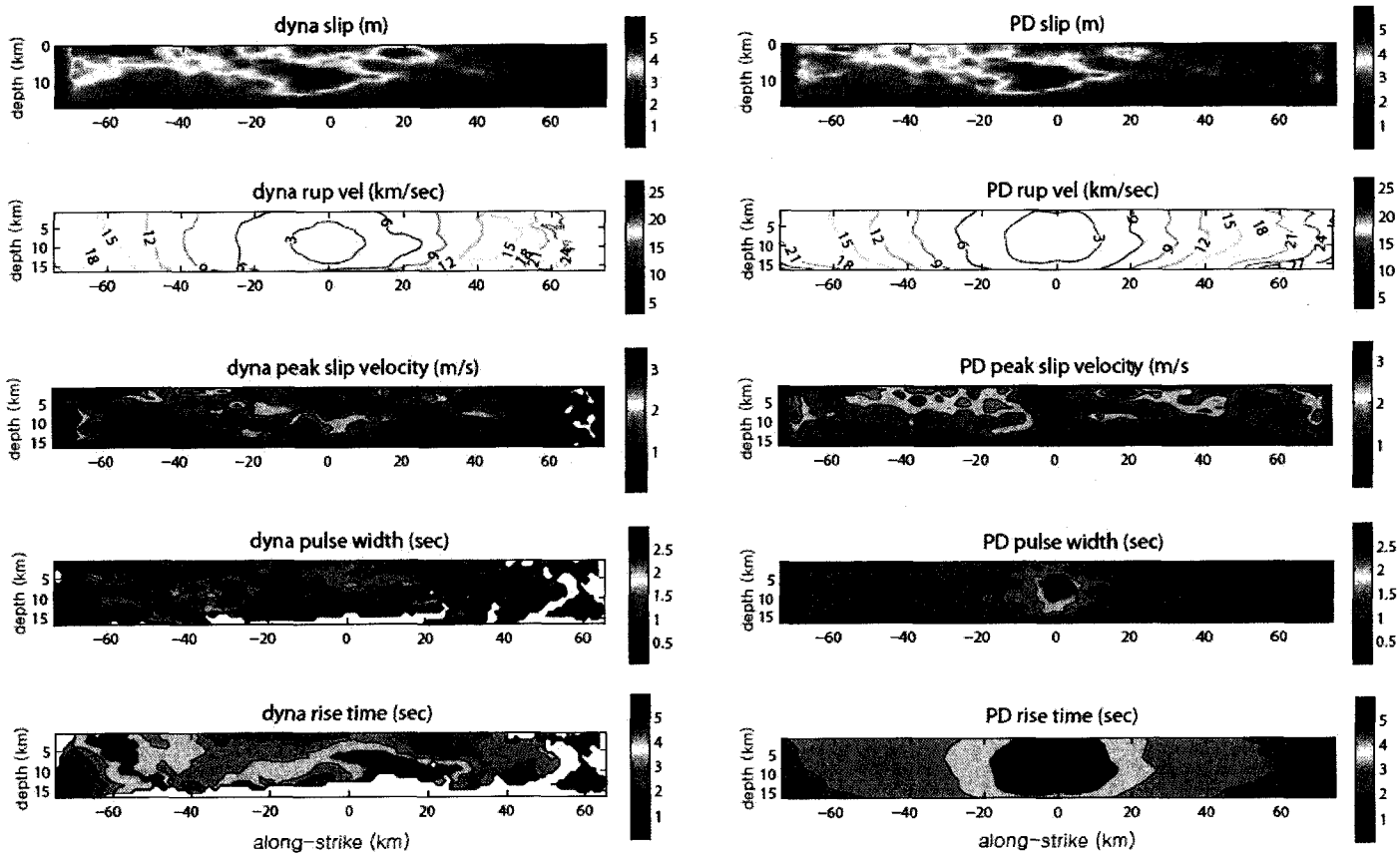

Figure 5.11. Comparison of the pseudo-dynamic modeling results with the full dynamic approach (Model: dyna31)

Reproduced with permission of the copyright owner. Further reproduction prohibited without permission.

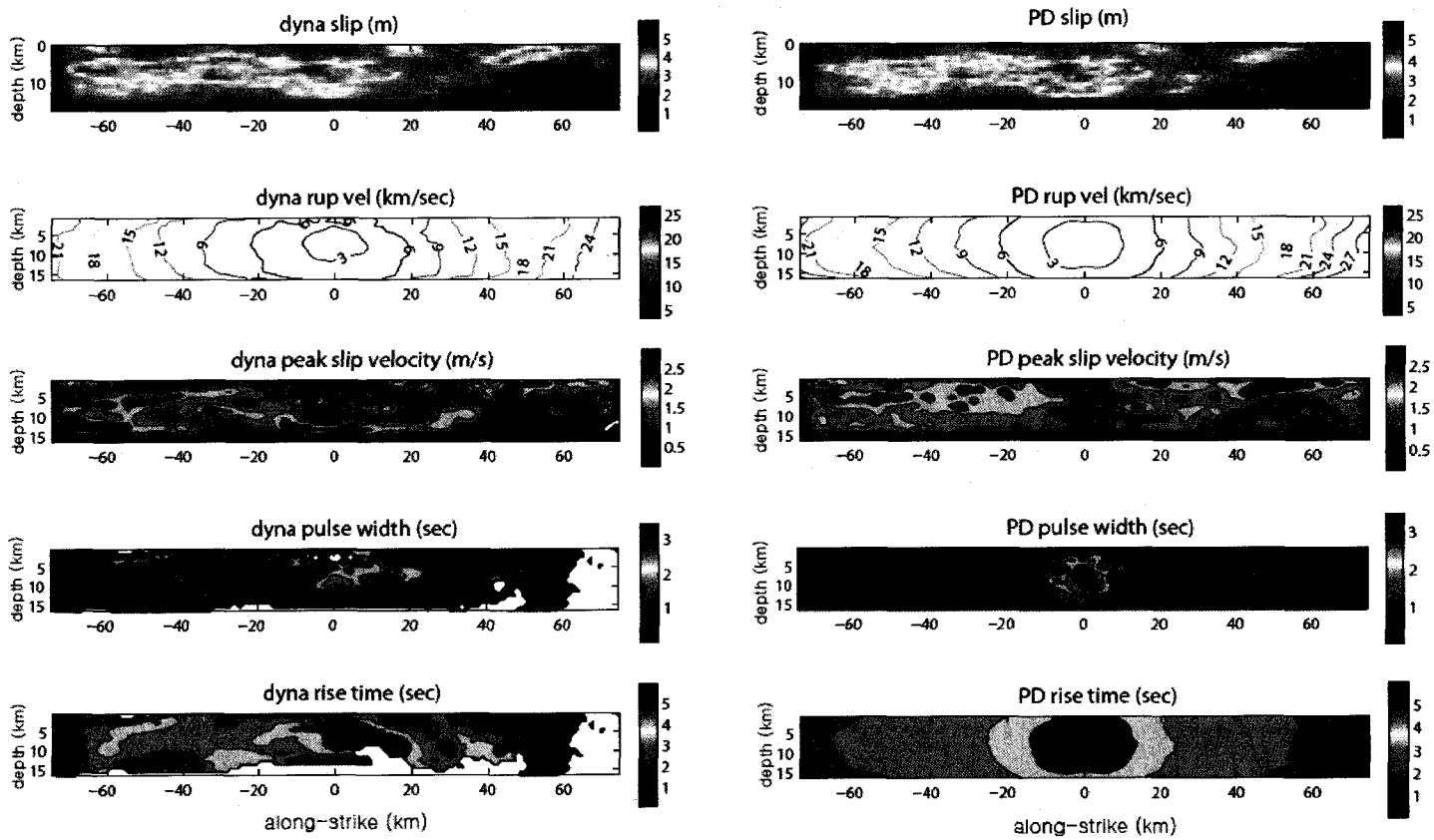

Figure 5.12. Comparison of the pseudo-dynamic modeling with the full dynamic approach (Model: dyna13)

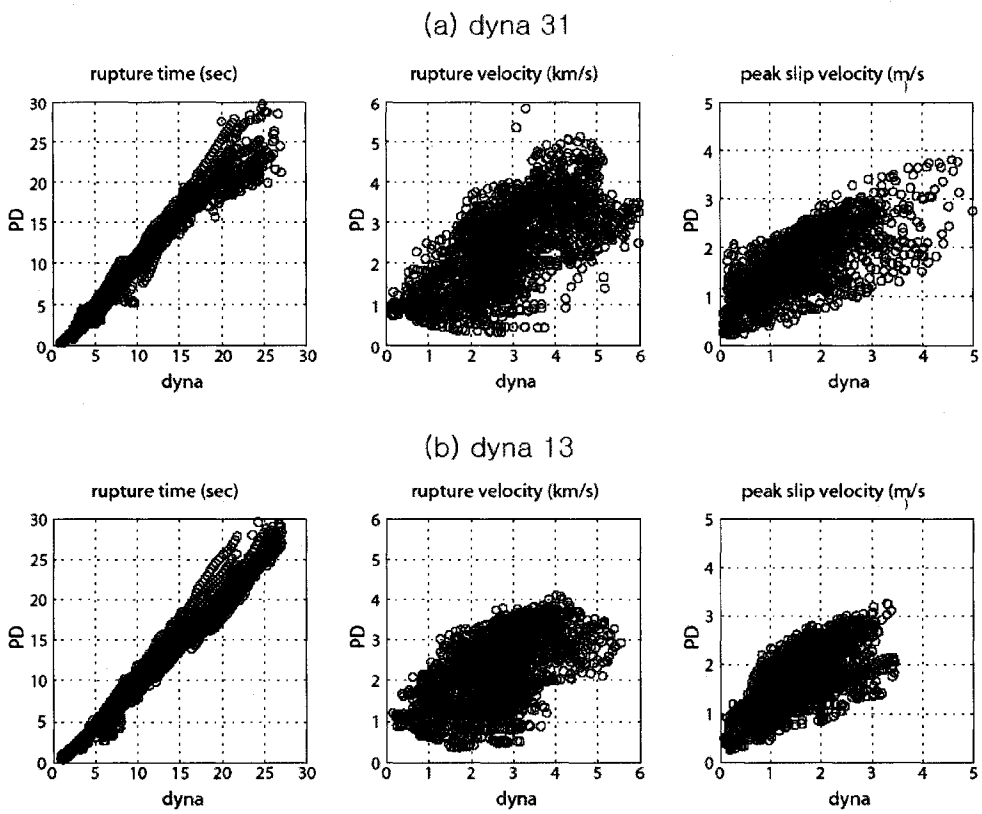

Figure 5.13. Scatter plots of the pseudo-dynamic modeling outputs with the full dynamic approach. Local rupture velocity in the middle of the plot is extracted from the rupture time distribution using equation (5.3) in both the pseudo-dynamic and full-dynamic modeling.

Reproduced with permission of the copyright owner. Further reproduction prohibited without permission.

Appendix A

Here we show that the de-nuisancing procedure of Yu and Segall (1996) reduces to the standard method, using the differences between repeated angles, when the pre and post earthquake networks are identical. That is, when all angles are repeated. Yu and Segall (1996) write the equations relating angle measurements $\mathbf{d\theta}$ to the coordinate corrections at the initial epoch $\mathbf{dx}_1$ and displacements $\mathbf{u}$ as

$$\begin{bmatrix} \mathbf{d\theta}_1 \\ \mathbf{d\theta}_2 \end{bmatrix} = \begin{bmatrix} \mathbf{A}_1 \\ \mathbf{A}_2 \end{bmatrix} \mathbf{dx}_1 + \begin{bmatrix} \mathbf{0} \\ \mathbf{A}_2 \end{bmatrix} \mathbf{u}, \tag{A1}$$

where the subscripts 1 and 2 refer to the initial and final surveys. The displacements are assumed to arise from fault slip $\mathbf{s}$ in an elastic medium so that $\mathbf{u} = \mathbf{Gs}$, and (A1) become

$$\begin{bmatrix} \mathbf{d\theta}_1 \\ \mathbf{d\theta}_2 \end{bmatrix} = \begin{bmatrix} \mathbf{A}_1 \\ \mathbf{A}_2 \end{bmatrix} \mathbf{dx}_1 + \begin{bmatrix} \mathbf{0} \\ \mathbf{A}_2\mathbf{G} \end{bmatrix} \mathbf{s}. \tag{A2}$$

If the network geometry is identical in both surveys then $\mathbf{A}_1 = \mathbf{A}_2 \equiv \mathbf{A}$ and subtracting the first set of equations from the second leads directly to

$$\mathbf{d\theta}_2 - \mathbf{d\theta}_1 = \mathbf{AGs}. \tag{A3}$$

In this case the changes in angles are directly related to the fault slip with no need to consider the corrections to the initial coordinates. For least squares estimation (A3) lead to normal equations

$$\mathbf{G}^{\mathrm{T}}\mathbf{A}^{\mathrm{T}}(\mathbf{d\theta}_2 - \mathbf{d\theta}_1) = \mathbf{G}^{\mathrm{T}}\mathbf{A}^{\mathrm{T}}\mathbf{AGs}. \tag{A4}$$

We now consider the de-nuisancing procedure. Equation (A2) can be written more compactly as

Reproduced with permission of the copyright owner. Further reproduction prohibited without permission.

$$\mathbf{d\theta} = \mathbf{\Psi dx} + \mathbf{\Omega s} \tag{A5}$$

Yu and Segall (1996) define a projection operator $\mathbf{Q}$ that annihilates the dependence on $\mathbf{dx}$

$$\mathbf{Q} \equiv \mathbf{I} - \mathbf{\Psi\Psi}^*, \tag{A6}$$

where $\mathbf{I}$ is an identity matrix and $\mathbf{\Psi}^*$ is the generalized inverse of $\mathbf{\Psi}$. Pre-multiplying (A5) by $\mathbf{Q}$ leads to

$$\mathbf{Qd\theta} = \mathbf{Q\Omega s}, \tag{A7}$$

since

$$\mathbf{Q\Psi} = (\mathbf{I} - \mathbf{\Psi\Psi}^*)\mathbf{\Psi} = \mathbf{0}. \tag{A8}$$

A least squares estimate of fault slip then follows from the normal equations

$$\mathbf{\Omega}^{\mathrm{T}}\mathbf{Qd\theta} = \mathbf{\Omega}^{\mathrm{T}}\mathbf{Q\Omega s}, \tag{A9}$$

since $\mathbf{Q}$ is both symmetric and idempotent.

If the network geometry is repeated then

$$\mathbf{\Psi} = \begin{bmatrix} \mathbf{A} \\ \mathbf{A} \end{bmatrix}. \tag{A10}$$

The matrix $\mathbf{A}$ has singular value decomposition (SVD) given by $\mathbf{A} = \mathbf{U}_{\mathbf{p}}\mathbf{S}_{\mathbf{p}}\mathbf{V}_{\mathbf{p}}^{\mathbf{T}}$, where p is the number of non-zero singular values. It follows then that $\mathbf{\Psi}$ has an SVD with the same singular vectors spanning the model space V and repeated data space singular vectors given by

Reproduced with permission of the copyright owner. Further reproduction prohibited without permission.

$$\begin{bmatrix} \frac{1}{\sqrt{2}}\mathbf{U_p} \\ \frac{1}{\sqrt{2}}\mathbf{U_p} \end{bmatrix}, \tag{A11}$$

where the factor of $1/\sqrt{2}$ arises due to normalization. Thus, in this case the projection operator $\mathbf{Q}$ is

$$\mathbf{Q} = \begin{bmatrix} \mathbf{I} - \frac{1}{2}\mathbf{H} & -\frac{1}{2}\mathbf{H} \\ -\frac{1}{2}\mathbf{H} & \mathbf{I} - \frac{1}{2}\mathbf{H} \end{bmatrix}, \tag{A12}$$

where $\mathbf{H} \equiv \mathbf{AA}^* = \mathbf{U_p U_p^T}$. Substituting (A12) into (A9) leads to

$$\begin{aligned} \mathbf{G^T A^T}[(\mathbf{I} - \frac{1}{2}\mathbf{H})\mathbf{d\theta_2} - \frac{1}{2}\mathbf{H}\mathbf{d\theta_1}) &= \mathbf{G^T A^T}(\mathbf{I} - \frac{1}{2}\mathbf{H})\mathbf{AGs} \\ \frac{1}{2}\mathbf{G^T A^T}(\mathbf{d\theta_2} - \mathbf{d\theta_1}) &= \frac{1}{2}\mathbf{G^T A^T AGs} \end{aligned} \tag{A13}$$

since $\mathbf{A^T H} = \mathbf{(HA)^T} = \mathbf{(AA^* A)^T} = \mathbf{A^T}$. Comparing (A13) to (A4) we see that both methods lead to the same result when all angles are repeated. The de-nuisancing procedure, however, allows all measurements to be used when the angles are not all repeated.

Reproduced with permission of the copyright owner. Further reproduction prohibited without permission.

Appendix B

Bibliography

Aagaard, B. T., and T. H. Heaton (2004). Near-source ground motions from simulations of sustained intersonic and supersonic fault ruptures, *Bull. Seism. Soc. Am.* **94**, 2,064-2,078.

Abercrombie, R.E., and J.R. Rice (2005). Can observations of earthquake scaling constrain slip-weakening?, *Geophys. J. Int.* **162**, 406-424.

Aki, K. (1972), Earthquake mechanism, *Tectonophysics*, **13**, 423-446.

Andrews, D.J. (1976a). Rupture propagation with finite stress in antiplane strain, *J. Geophys. Res.* **81**, 3,575-3,582.

Andrews, D.J. (1976b). Rupture velocity of plane strain shear cracks, *J. Geophys. Res.* **81**, 5,679-5,687.

Andrews, D.J. (1980). A stochastic fault model, I. Static case, *J. Geophys. Res.*, **85**, 3,867-3,877.

Andrews, D.J. (1999). Test of two methods for faulting in finite-difference calculations, *Bull. Seism. Soc. Am.* **89**, 931-937.

Andrews, D.J. (2004). Rupture models with dynamically determined breakdown displacement, *Bull. Seism. Soc. Am.* **94**, 769-775.

Beroza, G.C. (1991). Near-source modeling of the Loma Prieta earthquake: evidence for heterogeneous slip and implications for earthquake hazard, *Bull. Seism. Soc. Am.* **81**, 1,603-1,621.

Beroza, G.C., and T. Mikumo (1996). Short slip duration in dynamic rupture in the presence of heterogeneous fault properties, *J. Geophys. Res.* **101**, 22,449-22,460.

Reproduced with permission of the copyright owner. Further reproduction prohibited without permission.

Beroza, G.C., and P. Spudich (1988). Linearlized inversion for fault rupture behavior; application to the 1984 Morgan Hill, California, earthquake, *J. Geophys. Res.* **93**, 6,275-6,296.

Boatwright, J., and H. Bundock (2005). Modified Mercalli Intensity maps for the 1906 San Francisco earthquake plotted in shake-map format, *U. S. Geol. Surv.* Open-File Rept. 2,005-1,135.

Bolt, B. A. (1968). The focus of the 1906 California earthquake, *Bull. Seism. Soc. Am.* **58**, 457-471.

Boore, D.M., and W.B. Joyner (1997). Site amplifications for generic rock sites, *Bull. Seism. Soc. Am.* **87**, 327-341.

Bouchon, M., M. P. Bouin, H. Karabulut, M. N. Toksöz, M. Dietrich, and A. Rosakis (2001). How fast is rupture during an earthquake? New insights from the 1999 Turkey earthquakes, *Geophys. Res. Lett.* **28**, 2,723-2,726.

Bouchon, M., and M. Vallée (2003). Observation of long supershear rupture during the magnitude 8.1 Kunlunshan earthquake, *Science* **301**, 824-826.

Burridge, R. (1973). Admissible speeds for plane-strain self-similar shear cracks with friction but lacking cohesion, *Geophys. J. R. Astro. Soc.* **35**, 439-455.

Byerlee, J. (1978), Friction of Rock, *Pure Appl. Geophys.* **116**, 615-626.

Cochard, A., and R. Madariaga (1994). Dynamic faulting under rate-dependent friction, *Pure Appl. Geophys.* **142**, 419-445.

Cohee, B.P., and Beroza (1994). Slip distribution of the 1992 Landers earthquake and its implications for earthquake source mechanics, *Bull. Seism. Soc. Am.* **84**, 692-712.

Cotton, F., and M. Campillo (1995). Frequency domain inversion of strong motions; application to the 1992 Landers earthquake, *J. Geophys. Res.* **100**, 3,961-3,975.

Reproduced with permission of the copyright owner. Further reproduction prohibited without permission.

Das, S., and K. Aki (1977). A numerical study of two-dimensional spontaneous rupture propagation, Geophys. *J. R. Astr. Soc.* **50**, 643-668.

Day, S.M. (1982a). Three-dimensional finite difference simulation of fault dynamics: rectangular faults with fixed rupture velocity, *Bull. Seism. Soc. Am.* **72**, 705-727.

Day, S.M. (1982b). Three-dimensional simulation of spontaneous rupture: the effect of nonuniform prestress, *Bull. Seism. Soc. Am.* **72**, 1,881-1,902.

Day, S.M., L.A. Dalguer, N. Lapusta, and Y. Liu (2005). Comparison of finite difference and boundary integral solutions to three-dimensional spontaneous rupture, *J. Geophys. Res.* **110**, B12307, doi:10.1029/2005JB003813.

Day, S.M., G. Yu, and D.J. Wald (1998). Dynamic stress changes during earthquake rupture, *Bull. Seism. Soc. Am.* **88**, 512-522.

Dieterich, J.H. (1994). A constitutive law for rate of earthquake production and its application to earthquake clustering, *J. Geophys. Res.* **99**, 2,601-2,618.

Dunham, E. M., and R. J. Archuleta (2004). Evidence for a supershear transient during the 2002 Denali fault earthquake, *Bull. Seism. Soc. Am.* **94**, S256-S268.

Ellsworth, W.L., M. Celebi, J.R. Evans, E.G. Jensen, R. Kayen, M.C. Metz, D.J. Nyman, J.W. Roddick, P. Spudich, C.D. Stephens (2004). Near-field ground motion of the 2002 Denali fault, Alaska, earthquake recorded at Pump Station 10, *Earthquake Spectra* **20**, 597-615.

Freund, L.B. (1979). The mechanics of dynamic shear crack propagation, *J. Geophys. Res.* **84**, 2,199-2,209.

Freund, L.B. (1990). *Dynamic fracture mechanics*, Cambridge University Press, New York.

Fukuyama, E., and R. Madariaga (1995). Integral equation method for plane crack with arbitrary shape in 3D elastic medium, *Bull. Seism. Soc. Am.* **85**, 614-628.

Reproduced with permission of the copyright owner. Further reproduction prohibited without permission.

Fukuyama, E., and T. Mikumo (1993). Dynamic rupture analysis: Inversion for the source process of the 1990 Izu-Oshima, Japan, earthquake (M = 6.5), *J. Geophys. Res.* **98**, 6,529-6,542.

Guatteri, M., and P. Spudich (2000), What can strong motion data tell us about slip-weakening fault friction laws?, *Bull. Seismol. Soc. Am.* **90**, 98-116.

Guatteri, M., P. Spudich, and G. Beroza (2001). Inferring rate and state friction parameters from a rupture model of the 1995 Hyogo-ken Nanbu (Kobe) Japan earthquake, *J. Geophys. Res.* **106**, 26,511-26,521.

Guatteri, M., P.M. Mai, G.C. Beroza (2004). A pseudo-dynamic approximation to dynamic rupture models for strong ground motion, *Bull. Seism. Soc. Am.* **94**, 2,051-2,063.

Guatteri, M., P.M. Mai, G.C. Beroza, and J. Boatwright (2003). Strong-ground motion prediction from stochastic-dynamic source models, *Bull. Seismol. Soc. Am.* **93**, 301-313.

Hartzell, S.H., and M. Iida (1990). Source complexity of the 1987 Whittier Narrows, California earthquake from inversion of strong motion records, *J. Geophys. Res.* **95**, 12,475 – 12,485.

Heaton, T.H. (1990). Evidence for and implications of self-healing pulses of slip in earthquake rupture, *Phys. Earth Plane Interiors* **64**, 1-20.

Hernandez, B., F. Cotton, and M. Campillo (1999). Contribution of radar interferometry to a two-step inversion of the kinematic process of the 1992 Landers earthquake, *J. Geophys. Res.* **104**, 13,083-13,099.

Herrero, A., and P. Bernard (1994). A kinematic self-similar rupture process for earthquakes, *Bull. Seism. Soc. Am.* **84**, 1,216-1,228.

Ida, Y. (1972), Cohesive force across the tip of a longitudinal-shear crack and Griffith's specific surface energy, *J. Geophys. Res.* **77**, 3,796-3,805.

Reproduced with permission of the copyright owner. Further reproduction prohibited without permission.

Ide, S., and M. Takeo (1996). The dynamic rupture process of the 1993 Kushiro-oki earthquake, *J. Geophys. Res.* **101**, 5,661-5,675.

Ide, S., and M. Takeo (1997). Determination of constitutive relations of fault slip based on seismic wave analysis, *J. Geophys. Res.* **102**, 27,379-27,391.

Jachens, R., R. Simpson, R. Graymer, C. Wentworth, and T. Brocher (2006). Three-dimensional geologic map of northern and central California: A basic model for supporting earthquake simulations and other predictive modeling, *Seism. Res. Lett.* **77**, 270-271.

Kostrov, B.V. (1964). Self similar problems of propagation of shear cracks, *Appl. Math. Mech.* (PMM) **28**, 889-898.

Kostrov, B.V. (1966). Unsteady propagation of longitudinal shear cracks, *Appl. Math. Mech.* (PMM) **30**, 1,042-1,049.

Kostrov, B. and S. Das (1988). *Principles of earthquake source mechanics*, Cambridge University Press, New York.

Lavallée, D., P. Liu, and R.J. Archuleta (2006). Stochastic model of heterogeneity in earthquake slip spatial distributions, *Geophys. J. Int.* **165**, 622-640.

Lawson, A. C. (1908). The California earthquake of April 18, 1906, Report of the State Earthquake Investigation Commission, Vol. 1, A. C. Lawson, Chairman, Carnegie Inst. of Washington, Washington, D. C. (reprinted 1969).

Lomax, A. (2005). A reanalysis of the hypocentral location and related observations for the great 1906 California earthquake, *Bull. Seism. Soc. Am.* **95**, 861-877.

Madariaga, R. (1983). Earthquake source theory: a review, in the proceedings of the International School of Physics, titled "Earthquakes: observation, theory and interpretation", edited by H. Kanamori and E. Boschi, North-Holland publishing company, New York, pp. 1-44.

Reproduced with permission of the copyright owner. Further reproduction prohibited without permission.

Madariaga, R. (1976). Dynamics of an expanding circular fault, *Bull. Seism. Soc. Am.* **66**, 639-666.

Mai, P.M., and G.C. Beroza (2000). Source scaling properties from finite-fault-rupture models, *Bull. Seism. Soc. Am.* **90**, 604-615.

Mai, P.M., and G.C. Beroza (2002). A spatial random field model to characterize complexity in earthquake slip, *J. Geophys. Res.* **107**, 2308, doi:10.1029/2001JB000588.

Mai, P.M., P. Somerville, A. Pitarka, L. Dalguer, S. Song, G. Beroza, H. Miyake, and K. Irikura (2006). On Scaling of Fracture Energy and Stress Drop in Dynamic Rupture Models: Consequences for Near-Source Ground-Motions, AGU Chapman Monograph Series on Radiated Seismic Energy (edited by R. Abercrombie, A. McGarr, H. Kanamori, and G. Toro), 283-294.

Matthews, M. V., and P. Segall (1993). Statistical inversion of crustal deformation data and estimation of the depth distribution of slip in the 1906 earthquake, *J. Geophys. Res.* **98**, 12,153-12,163.

Metropolis, N., A. W. Rosenbluth, M. N. Rosenbluth, A. H. Teller, and E. Teller (1953). Equation of state calculations by fast computing machines, *J. Chem. Phys.* **21**, 1,087-1,092.

Mikumo, T., K.B. Olsen, E. Fukuyama, and Y. Yagi (2003). Stress-breakdown time and slip-weakening distance inferred from slip-velocity functions on earthquake faults, *Bull. Seism. Soc. Am.* **93**, 264-282.

Mikumo, T., and T. Miyatake (1995). Heterogeneous distribution of dynamic stress drop and relative fault strength recovered from the results of waveform inversion: the 1984 Morgan Hill, California, earthquake, *Bull. Seism. Soc. Am.* **85**, 178-193.

Reproduced with permission of the copyright owner. Further reproduction prohibited without permission.

Mosegaard, K, and A. Tarantola (2002). Probabilistic approach to inverse problems, in International Handbook of Earthquake & Engineering Seismology, Part A., edited by W. H. K. Lee et al., pp. 237-265, Academic Press, San Diego, California.

Nielsen, S., and J.M. Carlson (2000). Rupture pulse characterization: Self-healing, self-similar, expanding solutions in a continuum model of fault dynamics, *Bull. Seism. Soc. Am.* **90**, 1,480-1,497.

Okada, Y. (1992). Internal deformation due to shear and tensile faults in a half-space, *Bull. Seism. Soc. Am.* **82**, 1,018-1,040.

Okubo, P.G. (1989). Dynamic rupture modeling with laboratory-derived constitutive relations, *J. Geophys. Res.* **94**, 12,321-12,355.

Olsen, K., R. Madariaga, and R. Archuleta (1997), Three dimensional dynamic simulation of the 1992 Landers earthquake, *Science* **278**, 834-838.

Peyrat, S., and K.B. Olsen (2004). Nonlinear dynamic rupture inversion of the 2000 Western Tottori, Japan, earthquake, *Geophys. Res. Lett.* **31**, L05604, doi:10.1029/2003GL019058.

Peyrat, S., K.B. Olsen, and R. Madriaga (2001). Dynamic modeling of the 1992 Landers earthquake, *J. Geophys. Res.* **106**, 26,467-26,482.

Pitarka, A., S. Day, and L.A. Dalguer (2005). Investigation of shallow crustal weak zone effects on rupture dynamics of surface and subsurface faulting, 86(52), Fall Meet. Suppl., Abstract S43A-1050.

Prentice C. S., D. J. Merritts, E. C. Beutner, P. Bodin, A. Schill, and J. R. Muller (1999). Northern San Andreas fault near Shelter Cove, California, *Geol. Soc. Am. Bull.* **111**, 512-523.

Reproduced with permission of the copyright owner. Further reproduction prohibited without permission.

Reid, H. F. (1910). The mechanics of the earthquake, The California earthquake of April 18, 1906, Report of the State Earthquake Investigation Commission, Vol. 2, A. C. Lawson, Chairman, Carnegie Inst. of Washington, Washington, D. C. (reprinted 1969).

Rice, J.R., C.G. Sammis, and R. Parson (2005). Off-fault secondary failure induced by a dynamic slip pulse, *Bull. Seism. Soc. Am.* **95** 109-134.

Rosakis, A. J., O. Samudrala, and D. Coker (1999). Cracks faster than the shear wave speed, *Science* **284**, 1,337-1,340.

Scholz, C.H. (1982). Scaling relations for strong ground motion in large earthquakes, *Bull. Seism. Soc. Am.* **72**, 1,903-1,909.

Scholz, C.H. (1990). *The mechanics of earthquakes and faulting*, Cambridge University Press, New York.

Segall, P., and M.V. Matthews (1988). Displacement calculations from geodetic data and the testing of geophysical deformation models, *J. Geophys. Res.* **93**, 14,954-14,966.

Sekiguchi, H., K. Irikura, T. Iwata, Y. Kakehi, and M. Hoshiba (1996), Minute locating of faulting beneath Kobe and the waveform inversion of the source process during the 1995 Hyogo-ken Nanbu, Japan, earthquake using strong ground motion records, *J. Phys. Earth* **44**, 473-487.

Shaw, B.E., and C.H. Scholz (2001). Slip-length scaling in large earthquakes: observations and theory and implications for earthquake physics, *Geophys. Res. Lett.* **28**, 2,995-2,998.

Somerville, P.G. (2003). Magnitude scaling of the near fault rupture directivity pulse, *Phys. Earth Planet. Interiors* **137**, 201-212.

Somerville, P.G., K. Irikura, R. Graves, S. Sawada, D.J. Wald, N. Abrahamson, Y. Iwasaki, T. Kagawa, N. Smith, and A. Kowada (1999). Characterizing crustal earthquake slip models for the prediction of strong ground motion, *Seism. Res. Lett.* **70**, 59-80.

Reproduced with permission of the copyright owner. Further reproduction prohibited without permission.

Somerville, P.G., N.F. Smith, R.W. Graves, and N.A. Abrahamson (1997). Modification of empirical strong ground motion attenuation relations to include the amplitude and duration effects of rupture directivity, *Seism. Res. Lett.* **68**, 199-222.

Song, S., and G.C. Beroza (2004). A simple dynamic model for the 1995 Kobe, Japan earthquake, *Geophys. Res. Lett.* **31**, L18613, doi:10.1029/2004GL020557.

Song, S., P. Segall, and G.C. Beroza (2008). A unified source model of the 1906 San Francisco earthquake, accepted for the special issue on the 1906 San Francisco Earthquake.

Spudich, P., M. Guatteri, K. Otsuki, and J. Minagawa (1998), Use of fault striations and dislocation models to infer tectonic shear stress during the 1995 Hyogo-ken Nanbu(Kobe) earthquake, *Bull. Seism. Soc. Am.* **88**, 413-427.

Steidl, J.H., R.J. Archuleta, and S.H Hartzell (1991). Rupture history of the 1989 Loma Prieta, California, earthquake, *Bull. Seism. Soc. Am.* **81**, 1,573-1,602.

Stein, S., and E. A. Okal (2005). Speed and size of the Sumatra earthquake, *Nature* **434**, 581 – 582.

Thatcher, W., G. Marshall, and M. Lisowski (1997). Resolution of fault slip along the 470-km-long rupture of the great 1906 San Francisco earthquake and its implications, *J. Geophys. Res.* **102**, 5,353-5,367.

Tinti, E., E. Fukuyama, A. Piatanesi, and M. Cocco (2005). A kinematic source-time function compatible with earthquake dynamics, *Bull. Seism. Soc. Am.* **95**, 1,211-1,223.

Tinti, E., P. Spudich, and M. Cocco (2005). Earthquake fracture energy inferred from kinematic rupture models on extended faults, *J. Geophys. Res.* **110**, B12303, doi:10.1029/2005JB003644.

Wald, D. J. (1996), Slip history of the 1995 Kobe, Japan, earthquake determined from strong motion, teleseismic, and geodetic data, *J. Phys. Earth* **44**, 489-503.

Reproduced with permission of the copyright owner. Further reproduction prohibited without permission.

Wald, D.J., D.V. Helmberger, and T.H. Heaton (1991). Rupture model of the 1989 Loma Prieta earthquake from the inversion of strong-motion and broadband teleseismic data, *Bull. Seism. Soc. Am.* **81**, 1,540-1,572.

Wald, D.J., and T.H. Heaton (1994). Spatial and temporal distribution of slip for the 1992 Landers, California, earthquake, *Bull. Seism. Soc. Am.* **84**, 668-691.

Wald, D. J., H. Kanamori, D. V. Helmberger, and T. H. Heaton (1993). Source study of the 1906 San Francisco earthquake, *Bull. Seism. Soc. Am.* **83**, 981-1019.

Wells, D.J., and K.J. Coppersmith (1994). New empirical relationships among magnitude, rupture length, rupture width, rupture area, and surface displacement, *Bull. Seism. Soc. Am.* **84**, 974-1,002.

Xia, K., A. J. Rosakis, and H. Kanamori (2004). Laboratory earthquakes: the sub-Rayleigh-to-supershear transition, *Science* **303**, 1,859-1,861.

Yoshida, S., K. Koketsu, B. Shibazaki, T. Sagiya, and Y. Yoshida (1996), Joint inversion of near- and far-field waveforms and geodetic data for the rupture process of the 1995 Kobe earthquake, *J. Phys. Earth* **44**, 437-454.

Yu, E., and P. Segall (1996). Slip in the 1868 Hayward earthquake from the analysis of historical triangulation data, *J. Geophys. Res.* **101**, 16,101-16,118.

Zeng, Y., J.G. Anderson, and Y. Guang (1994). A composite source model for computing realistic synthetic strong ground motions, *Geophys. Res. Lett.* **21**, 725-728.

Reproduced with permission of the copyright owner. Further reproduction prohibited without permission.